JLab E12-14-012 (e,e′p) cross section measurements for Ar and Ti

Linjie Gu

Dissertation submitted to the Faculty of the

Virginia Polytechnic Institute and State University

in partial fulfillment of the requirements for the degree of

Doctor of Philosophy

in

Physics

Camillo Mariani, Chair

Mark Pitt

Shunsaku Horiuchi

Thomas O'Donnell

May 7, 2021

Blacksburg, Virginia

Keywords: neutrino oscillation experiment, electron scattering

Copyright 2021, Linjie Gu

JLab E12-14-012 (e,e′p) cross section measurements for Ar and Ti

Linjie Gu

(ABSTRACT)

In recent years, many high precision experiments were carried aiming to improve the accuracy on the measurements of the neutrino oscillation parameters. One of the main source of uncertainty for neutrino oscillation experiments is due to the lack of a comprehensive theoretical description of neutrino-nucleus interactions. The US Deep Underground Neutrino Oscillation Experiments (DUNE) will deploy a series of detectors using Liquid Argon Time Projection Chambers (LArTPCs). A fully consistent parameter-free theoretical neutrino-nucleus scattering model on argon does not exist. The first step towards constructing a nuclear model will be to determine the energy and momentum distribution of protons and neutrons inside the argon nucleus. The JLab E12-14-012 experiment performed at Jefferson Laboratory in Newport News, Virginia, ran in 2017 and will provide such measurements in Argon and Titanium using electron scattering (e,e′p). The data collected by the experiment covers a wide range of energy transfers and also includes several other targets like aluminum and carbon. This Ph.D. thesis will present details of the JLab E12-14-012 experiment, together with first data analysis results of the exclusive (e,e′p) data on Argon and Titanium.

JLab E12-14-012 (e,e′p) cross section measurements for Ar and Ti

Linjie Gu

(GENERAL AUDIENCE ABSTRACT)

One of the limitations of accelerator based neutrino oscillation experiments including the Deep Underground Neutrino Experiment (DUNE), is the lack of understanding on how neutrino interact in matter. As an indispensable part of the neutrino physics future, DUNE is an accelerator based experiment that will use Argon as the neutrino target. Argon is a complicated target and a well defined theoretical model for neutrino interaction on Argon is needed. Thus, the JLab E12-14-012 experiment was performed in Hall A at Jefferson Lab in Newport, News, VA to help develop a neutrino-nucleus model for Argon. Data was collected on five targets (Argon, titanium, carbon, dummy and optical) for five different kinematic set-ups. The primary goal of this experiment is to measure the spectral functions of Argon and Titanium through (e,e′p) reactions. This thesis will present an overview of the experimental setup and results from the data analysis.

Acknowledgments

First and foremost, I am deeply grateful to my advisor, Prof. Camillo Mariani, for his invaluable advice, continuous support, and patience during my Ph.D. study. His immense knowledge and plentiful experience have encouraged me in all the time of my academic research and daily life.

I would also like to thank all my committee members, Prof. Mark Pitt, Prof. Shunsaku Horiuchi and Prof. Thomas O'Donnell, for their insightful comments and suggestions on my research study. In each committee meeting, the valuable feedback they provided help keep me pointed in the right direction.

I would like to extend my sincere thanks to all the members of the argon collaboration, including Prof. Omar Benhar, Prof. Donal Day, postdoctoral researchers Vishvas Pandey, Artur Ankowski and Libo Jiang, and other graduate students Hongxia Dai, Matthew Murphy and Daniel Abrams. I have really enjoyed the opportunity to get to work closely with them over the years.

I would like to offer my special thanks to my friends at Blacksburg. They are Tianran Chen, Junkai Zeng, Linghua Zhu, Shengchao Li, Lin Ju, Jieru Xie, Yuhang Lai, Xinyue Wang and Donghan Hu. I will never forget all the wonderful times we shared together in this peaceful town.

Lastly, I thank my parents for their unconditional love and support. Without whom none of these will be possible.

Contents

List of Figures x

List of Tables xv

1 Introduction 1

1.1 Physics Motivation 1

1.2 Neutrino Oscillation 2

1.3 DUNE - The Deep Underground Neutrino Experiment 4

1.4 Neutrino-Nucleus Scattering 6

1.5 Electron Scattering 8

1.5.1 Inclusive Cross Section (e,e') 9

1.5.2 Exclusive cross section 10

1.6 Final State Interactions (FSI) 16

1.6.1 Impulse Approximation 17

1.6.2 Plane Wave Impulse Approximation (PWIA) 17

1.6.3 Distorted Wave Impulse Approximation (DWIA) 18

2 JLab E12-14-012 Experimental Setup 20

2.1 Overview 20

2.2 Beamline 21

2.2.1 Beam Current Measurements 21

2.2.2 Beam Position Measurements 22

2.2.3 Beam Energy Measurements 22

2.3 Target System 23

2.4 High Resolution Spectrometers (HRSs) 26

2.5 Detector Package 27

2.5.1 Vertical Drift Chambers 27

2.5.2 Scintillators 29

2.5.3 Gas Čerenkov detector 31

2.5.4 Lead Glass Calorimeter 32

2.6 Trigger System 33

2.7 Data Acquisition 34

3 JLab E12-14-012 Experiment - Data Analysis 36

3.1 Extracting the Differential Cross Section 36

3.2 Efficiency Corrections 38

3.2.1 Deadtime Correction 38

3.2.2 Trigger Efficiency 39

3.2.3 Particle Identification Efficiency 41

3.2.4 VDC Tracking Efficiency 42

3.2.5 Vertex Z Correction 44

3.2.6 Coincidence Time Correction 45

3.3 Background Study 48

3.3.1 Background From Target Wall 48

3.3.2 Accidental Background 49

3.4 List of Systematic Uncertainties 50

3.4.1 Systematic Uncertainty from Cuts 51

3.4.2 Systematic Uncertainty from the simulation 52

3.4.3 Systematic Uncertainty from Radiative Corrections and the input MC Cross Section Model 53

3.4.4 Systematic Uncertainty from Radiative corrections Dependence on Boiling Effect 53

3.4.5 Summary of the Systematic Uncertainties 55

4 Measurement of the cross sections for inclusive electron scattering in the E12-14-012 experiment at JLab 56

4.1 Introduction 57

4.2 Experimental Setup 60

4.3 Data Analysis 64

4.3.1 Yield-Ratio Method 64

4.3.2 Acceptance Method 64

4.4 Uncertainty Analysis 70

4.5 Experimental Results 73

4.6 Scaling and A-dependence 79

4.7 Summary and Conclusions 83

5 Measurement of the Ar(e,e′p) and Ti(e,e′p) cross sections in Jefferson Lab Hall A 85

5.1 Introduction 86

5.2 Experimental Setup 90

5.3 Data Analysis 94

5.3.1 The $(e, e'p)$ cross section 94

5.3.2 Data analysis details 98

5.3.3 Test spectral functions 100

5.4 Uncertainty Analysis 103

5.4.1 Final state interactions 107

5.5 Differential cross section comparison 112

5.6 Summary and Conclusions 116

5.7 Acknowledgments 117

6 Summary 118

Bibliography **120**

List of Figures

1.1 Schematic of the Deep Underground Neutrino Experiment [6]. 5

1.2 Example of the typical (e,e′) reaction energy spectrum 10

1.3 Feynman diagram of the Quasi-Elastic e-nucleus scattering 10

1.4 Schematic of the (e,e′p) reaction [12] 11

1.5 A diagram of the PWIA in the (e,e′p) reaction [12]. 17

1.6 DWIA in (e,e′p) reaction [12]. 18

2.1 A picture of Jefferson Experimental Hall A [18]. 21

2.2 Side view of the target system of JLab E12-14-012. 23

2.3 Technical 3D drawing of the argon target. 24

2.4 Picture of the several targets used during the JLab E12-14-012 experiment. The top aluminium cell is the argon gas cell. The nine carbon foils are visible, mounted just below the gas cell. 25

2.5 Schematic of the shell model structures of argon and titanium [22]. 25

2.6 Schematic layout of the spectrometer magnet configuration (QQDQ) [19]. . . 27

2.7 HRS detector stack. All the detectors for different experiment are shown in the diagram. Figure is from Ref. [19] 28

2.8 Schematic diagram of the Hall A HRS VDCs [19]. 29

2.9 A typical VDC track example. The continuous lines represent the path of least travel time distance between ionized electron and sense wires. The dot-dashed lines are the distance projection to reconstruct the trajectory [24]. . 30

2.10 A diagram showing the spherical mirrors and PMTs inside the Gas Čerenkov [26]. 32

2.11 Schematic layout of the calorimeters in both the HRS_L and the HRS_R [19]. 33

2.12 Layout of the trigger design for the E12-14-012 experiment [22]. 34

3.1 Trigger efficiency of T1 using two calculation methods for different runs in Kinematic 1. Red dots calculated from T1/T2 directly. Green dots represents the product of T3 and T4 efficiencies. 40

3.2 The distribution of the total ADC counts for all channels in gas Čerenkov detector. 41

3.3 Distribution of event's β values. The region indicated by the two red lines is the region of interest (corresponding to proton events). 43

3.4 The distribution of reconstructed event vertex along the z direction for the Al dummy targets. The unit of x axis is meters 45

3.5 The coincidence time distribution for Ar $(e, e'p)$ reaction. The unit of the x axis is seconds. 48

3.6 The coincidence time distribution for Ar $(e, e'p)$ reaction. The red box selects the background region to quantify the background ratio. The unit of x axis is seconds. 49

3.7 The vertex z distribution difference between left and right arm. Red curve is the Gaussian fit applied to the peak. 52

3.8 The distribution of the normalized yield versus different beam currents. . . . 54

4.1 (color online). Distribution along the beam direction of reconstructed events for the multi-foil carbon target. The shaded regions represent the data selected to identify the events coming from individual carbon foils. 67

4.2 (color online). Event yields from carbon foils at different positions along the beam direction, normalized to the yield for the central foil, for the uncorrected data and the Monte Carlo simulation. The dependence of the cross section on the scattering angle, correctly taken into account in the Monte Carlo simulation, introduces a linear trend in the data that needs to be corrected for. All uncertainties are purely statistical. 68

4.3 (color online). Event yields in the corrected data for the multi-foil carbon target surviving the z-position selection, normalized to the yield for the central foil. The outcomes of two correction procedures are compared. The error bars are symmetric and represent the total uncertainties, being the statistical and systematic uncertainties added in quadrature. 69

4.4 (color online). Double-differential cross section extracted for inclusive electron scattering off the Al-7075 target at beam energy 2.222 GeV and scattering angle 15.54°. The inner and outer uncertainty bands correspond to statistical and total uncertainties, respectively. 73

4.5 (color online). Comparison of the Al(e, e') cross sections extracted using the yield-ratio and acceptance methods. The inner (outer) bands for the yield-method show statistical (total) uncertainties. For the acceptance method only statistical uncertainties are shown. 74

4.6 (color online). Comparison of the cross sections per nucleon for aluminum, argon [37], titanium [36], and carbon [36] measured at beam energy 2.222 GeV and scattering angle 15.54°. The average nucleon number for every target is calculated according to the natural abundances of isotopes, see details in the text. The bands represent the total uncertainties. 76

4.7 (color online). Same as in Fig. 4.6 but for the cross sections normalized by the combination of the elementary cross sections according to Eq. (4.6). . . . 77

4.8 (color online) Comparison between the scaling function of aluminum obtained from the E12-14-012 data (this work), represented by diamonds, and those obtained from the data of Day *et al.* [49]. The data are labeled according to the value of Q^2 corresponding to quasi elastic kinematics. 80

4.9 (color online) Q^2-dependence of the scaling functions $F(y, Q^2)$ obtained from the cross section displayed in Fig. 4.4 and from the data reported in Ref. [49]. The meaning of the symbols is the same as in Fig. 4.8. 81

4.10 (color online) Scaling functions of second kind, obtained from the inclusive cross sections measured by the E12-14-012 experiment using carbon, aluminum, argon and titanium targets. 82

5.1 Missing momentum distributions of protons in argon and titanium assumed in this analysis. 101

5.2 Missing energy distribution of protons in (a) argon and (b) titanium assumed in this analysis. 104

5.3 Six-fold differential cross section as a function of missing energy for argon ((a) panel) and titanium ((b) panel). The background estimate (line connecting the experimental data points) is multiplied by 10 for purpose of presentation. The MC predictions, based on the mean-field SF, include a correction for the nuclear transparency, while other FSI effects are not accounted for. 105

5.4 Same as Fig. 5.3 but for the cross section as a function of missing momentum. The inner (outer) uncertainty bands correspond to statistical (total) uncertainties. 106

5.5 Reduced cross section as a function of missing momentum for the $1p_{1/2}$ proton knockout from argon. We compare the PWIA and DWIA results obtained for the parallel kinematics considered in this analysis. 108

5.6 Differential cross section for elastic proton scattering on ^{40}Ar at 0.8 GeV as a function of scattering angle. Results for the DEM, EDAD1, and EDAD3 optical potentials, which turn out to almost completely overlap, are compared with the experimental data [110]. 111

5.7 Six-fold differential cross section for argon as a function of missing momentum integrated over different ranges of missing energy. The background estimate is multiplied by 10 for presentation. The MC predictions, based on the mean-field SF, include the full FSI corrections. 114

5.8 Same as Fig. 5.7 but for titanium. 115

List of Tables

2.1 Main characteristics of the Hall A HRSs [19]. 26

2.2 Data taking summary [22] 35

2.3 Kinematic settings for (e,e′p) measurements, the central kinematic variables include beam energy (E_e), central momenta ($E_{e'}$, P_p), central angles (θ_e, θ_p), momentum transfer ($|\vec{q}|$) and central missing momentum (p_m) [22]. 35

3.1 Trigger system designed for E12-14-012 experiment. 40

3.2 Accidental Background to signal ratio in each kinematic and target. 50

4.1 Composition of the Al-7075 alloy. For each element, we provide the number of protons Z and the average number of neutrons N calculated according to the isotopic abundances [38]. 62

4.2 Contributions to systematic uncertainties in the yield-ratio method for aluminum and argon. 71

5.1 Kinematics settings used to collect the data analyzed here. 90

5.2 Trigger lists detailing how the signals from different detector components are combined. LEFT and RIGHT identify the electron and proton arm, respectively. 92

5.3 Summary of the efficiency analysis for the argon and titanium targets. . . . 94

5.4 Parametrization of the missing energy distributions of ${}^{40}_{18}$Ar and ${}^{48}_{22}$Ti assumed in this analysis. The central peak position E_α, its width σ_α, and the lower (upper) bound on the considered energy range, E^α_{low} (E^α_{high}) are shown for each level α. All values are given in units of MeV. 99

5.5 Contributions to systematical uncertainties for argon and titanium average over all the E_m and p_m bins. 103

5.6 Shifts between the reduced DWIA and PWIA cross sections, and the DWIA to PWIA cross-section ratios, obtained for proton knockout from various argon orbital using different optical potentials: DEM [108], EDAD3 [109], and EDAD1 [109]. All results are calculated for $p_m > 0$. 109

Chapter 1

Introduction

This Ph.D. thesis will present the data analysis from the JLab E12-14-012 experiment performed in Hall A at the Thomas Jefferson National Accelerator Facility (JLAB) in Newport News, Virginia. The data taking was performed in the Spring of 2017 using four different targets (Argon, Titanium, Carbon and Aluminum). The main purpose of the JLab E12-14-012 experiment is to measure the spectral functions of Argon and Titanium through (e,e′) and (e,e′p) reactions.

In the first chapter, we will briefly review the motivations for the JLab E12-14-012 experiment as well as an overview of electron and neutrino scattering on nuclei.

1.1 Physics Motivation

In recent years, neutrino physics has developed fast and high precision measurements have been performed by complex and big detectors. Several experiments already proved that neutrinos have non-vanishing masses, through measuring neutrino oscillations, which is against the massless particle assumption in the Standard Model. Nowadays, after reporting high quality measurements of the θ_{13} mixing angle, future experiments like the deep underground neutrino experiment (DUNE) will focus on the search for CP violation in the leptonic sector, which is one of the top priority of the US particle physics community. However, these searches require high accuracy measurement of the neutrino-oscillation parameters and pre-

cision knowledge of neutrino interactions with complex nuclei in preparation for the current and future multi-kilotons neutrino detectors. One of these experiments, in particular, is going to use the Liquid Argon Time Projection Chambers (LArTPCs) as the neutrino detector. A fully consistent parameter-free theoretical neutrino-nucleus model on Argon is therefore needed. Argon is a complex nucleus that is non-isospin symmetric. Lepton-nucleus scattering was modeled in the '80s and then the models were tested using electron scattering experiments. There is no available data on the argon nuclei. Therefore, electron-argon scattering data is needed to help build a fully consistent neutrino-nucleus interaction model.

The JLab E12-14-012 experiment was proposed to measure inclusive and exclusive electron scattering on Argon and Titanium. This experiment will provide the experimental inputs to help generate the theoretical model presented in Ref. [1, 2] for argon. In addition, measuring spectral function of argon nucleus would give us the initial momentum and energy distributions of nucleons bound in the argon nucleus, which could be directly used in the reconstruction of neutrino energies. Therefore, it is important to obtain nuclear structure information through measuring the (e,e′p) cross section of argon.

1.2 Neutrino Oscillation

In the Standard Model of Particle Physics, neutrinos are treated as neutrally-charged and massless elementary particles [3, 4]. They came in three different flavors, ν_e, ν_μ, and ν_τ, which refers to three types of charged leptons, electron, muon, and tau. Neutrino experiments observed that neutrinos oscillate between flavors, which indicates that neutrinos have a finite though non-zero mass. In the following we show a simple two flavor neutrino oscillation model, where the $|\alpha\rangle$ and the $|\beta\rangle$ are the two flavor eigenstates, and the $|1\rangle$ and the $|2\rangle$ are the two mass eigenstates, which could be also viewed as the mixture of flavor eigenstates.

$$\begin{pmatrix} |\nu_\alpha\rangle \\ |\nu_\beta\rangle \end{pmatrix} = \begin{pmatrix} \cos\theta & \sin\theta \\ -\sin\theta & \cos\theta \end{pmatrix} \begin{pmatrix} |\nu_1\rangle \\ |\nu_2\rangle \end{pmatrix} = U \begin{pmatrix} |\nu_1\rangle \\ |\nu_2\rangle \end{pmatrix}, \tag{1.1}$$

where U is the mixing matrix and θ is the mixing angle.

Considering quantum mechanics laws, the oscillation probability $P(\nu_\alpha \to \nu_\beta)$ could be written as

$$P(\nu_\alpha \to \nu_\beta) = \sin^2(2\theta)\sin^2\left(\Delta m^2 \frac{L}{4E}\right). \tag{1.2}$$

where $\Delta m^2 = |m_1^2 - m_2^2|$, L is the oscillation distance in meters. E is the neutrino energy, and typically on the order of MeV.

Scientists put lots of effort studying the neutrino oscillation and more and more Long Baseline Neutrino Experiment (LBNE) like DUNE are being prepared. People already know that CP is violated for quarks, if scientists could further prove CP is also violated among neutrinos through comparing neutrino oscillations with anti-neutrino oscillations, it will cause a big "earthquake" in physics society.

1.3 DUNE - The Deep Underground Neutrino Experiment

The DUNE [5] neutrino experiment is one of the most exciting next generation Long Baseline Neutrino Experiment (LBNE) to expect. More than 1,200 collaborators from over 30 countries participate in this experiment. The DUNE experiment will use detectors based on the Liquid Argon Time-Projection Chambers (LArTPCs) technology. Apart from precision goal of oscillation parameter measurements, like the third mixing angle θ_{13}, DUNE's goal is to measure the value of the delta CP violation in the leptonic sector.

The Long-Baseline Neutrino Facility (LBNF) will provide the neutrino beam line for the DUNE experiment, with neutrino energy ranging between 1 up to 8 GeV. DUNE will have a far and near detectors. The near detector will be located at Fermilab, and will provide measurements of the neutrino flux and cross sections on a variety of targets. The far detector will be installed 1,300 km away from Fermilab in the Sanford Laboratory at a depth of 4,500 m.w.e. A schematic of the DUNE experiment is shown in Fig. 1.1. The far detector will be used to provide high-precision neutrino flavor identification information and search for CP violation [5, 6].

The CP violation phase δ_{CP} will be estimated by the "appearance" searches, which is the searching for the appearance of ν_e or ν_τ in a pure ν_μ beam. In other word, an observation of an asymmetry between the oscillation probabilities $P(\nu_\mu \to \nu_e)$ and $P(\bar{\nu}_\mu \to \bar{\nu}_e)$ will prove the existence of the CP violation.

The event rates at near and far detectors could be written as,

$$N^{\alpha}_{\mathrm{ND}}(\boldsymbol{p}_{\mathrm{reco}}) = \sum_i \phi_\alpha(E_{\mathrm{true}}) \times \sigma^i_\alpha(\boldsymbol{p}_{\mathrm{true}}) \times \epsilon_\alpha(\boldsymbol{p}_{\mathrm{true}}) \times R_i(\boldsymbol{p}_{\mathrm{true}}; \boldsymbol{p}_{\mathrm{reco}}) \tag{1.3}$$

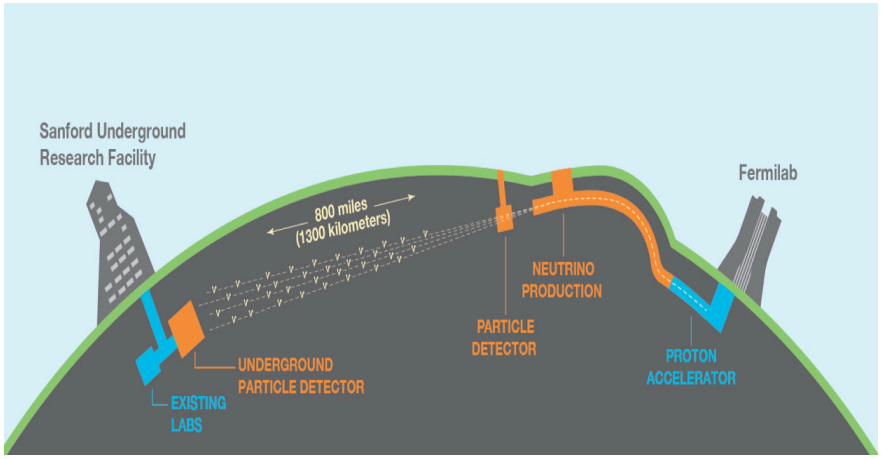

Figure 1.1: Schematic of the Deep Underground Neutrino Experiment [6].

$$N_{\mathrm{FD}}^{\alpha\to\beta}(\boldsymbol{p}_{\mathrm{reco}}) = \sum_i \phi_\alpha(E_{\mathrm{true}}) \times P_{\alpha\beta}(E_{\mathrm{true}}) \times \sigma_\beta^i(\boldsymbol{p}_{\mathrm{true}}) \times \epsilon_\beta(\boldsymbol{p}_{\mathrm{true}}) \times R_i(\boldsymbol{p}_{\mathrm{true}};\boldsymbol{p}_{\mathrm{reco}}). \quad (1.4)$$

where $N_{\mathrm{ND}}^{\alpha}(\boldsymbol{p}_{\mathrm{reco}})(N_{\mathrm{FD}}^{\alpha}(\boldsymbol{p}_{\mathrm{reco}}))$ is the event rate at near (far) detector, which varies according to whatever value the reconstructed variable $\boldsymbol{p}_{\mathrm{reco}} \equiv (E_{\mathrm{reco}}, \vec{p}_{\mathrm{reco}})$ takes on. ϕ_α is the flux of α neutrino at the near detector, $P_{\alpha\beta}(E_{\mathrm{true}})$ is the oscillation probability. σ_α^i represents the neutrino cross section for flavor α at interaction i. ϵ_α (ϵ_β) is the detector efficiency for a neutrino of flavor α (β) interaction. $R_i(\boldsymbol{p}_{\mathrm{true}};\boldsymbol{p}_{\mathrm{reco}})$ is the reconstruction probability of an event due to nuclear or detector effects.

The ratio of Eq. (1.4) and Eq. (1.3) refers to the oscillation probability $P(\nu_\alpha \to \nu_\beta)$. Through comparison with Eq. (1.2), the oscillation parameters θ and Δm^2 can be extracted. The distance L is a easily measurable variable. However, considering neutrinos has no electrical charge and a very small mass, the neutrino energy E can not be measured directly. We have to reconstruct the neutrino energy using charged current quasielastic (CCQE) method [7].

$$E_\nu = \frac{m_p^2 - m_\ell^2 - E_n^2 + 2E_\ell E_n - 2\mathbf{k}_n \cdot \mathbf{p}_n + |\mathbf{p}_n^2|}{2(E_n - E_\ell + |\mathbf{k}_\ell|\cos\theta_\ell - |\mathbf{p}_n|\cos\theta_n)}, \quad (1.5)$$

where $|\mathbf{k}_\ell|$ and $|\theta_\ell|$ are measurable. θ_n is the angle between the outgoing lepton and the

neutrino beam direction. While $\mathbf{p}_n$ and E_n are the unknown momentum and energy of the neutron interactions. Measuring spectral functions of target nucleus will provide the energy and momentum distribution of protons and neutrons bound inside, which will allow more accurate reconstruction of the neutrino energies. For the DUNE experiment, if one can measure the spectral function of Argon nucleus and further develop a theoretical model of neutrino-nucleus interactions and nuclear effects, this will be a significant step ahead in improving the measurement accuracy of the oscillation parameters, more importantly the CP violation phase in leptonic sector.

1.4 Neutrino-Nucleus Scattering

In neutrino-nucleus interaction,

$$\nu_\ell(k) + A(p) \to \ell^-(k') + X(p') \tag{1.6}$$

After neutrino ν_ℓ interacts with nucleus A, one should expect an outgoing lepton ℓ and a hadronic state X. The four-dimensional momenta is

$$k = (E_\nu, \mathbf{k}), k' = (E_\ell, \mathbf{k}'), p = (E_p, \mathbf{p}), p' = (E_{p'}, \mathbf{p}'). \tag{1.7}$$

The two-fold differential cross section of this process could be written as [2, 8, 9, 10],

$$\frac{d^2\sigma}{d\Omega_\ell dE_\ell} = \frac{G_F^2\, V_{ud}^2}{16\,\pi^2}\,\frac{|\mathbf{k}_\ell|}{|\mathbf{k}_\nu|}\,L_{\lambda\mu}\,W^{\lambda\mu}\ , \tag{1.8}$$

where G_F is the Fermi constant. $|V_{ud}|$ is the coupling of the quarks u and d in the Cabibbo-Kobayashi-Maskawa (CKM) matrix V. $L_{\lambda\mu}$ is the leptonic tensor, with m_ℓ^2 term neglected, $L_{\lambda\mu}$ could be written as

$$L_{\lambda\mu} = 8(k_\ell^\lambda k_\nu^\mu + k_\mu^\lambda k_\ell^\nu - g^{\lambda\mu} k_\ell \cdot k_\nu - i\epsilon^{\lambda\mu\alpha\beta} k_{\ell\beta} k_{\nu\alpha}), \tag{1.9}$$

where $\epsilon_{\lambda\nu\alpha\beta}$ is the fully antisymmetric Levi-Civita tensor.

The hadronic tensor is defined as $W^{\lambda\mu}$, which could be written in terms of five structure functions followed.

$$\begin{aligned} W^{\lambda\mu} = -g^{\lambda\mu} W_1 + \frac{p^\lambda p^\mu}{m_N^2} W_2 - i\epsilon^{\lambda\mu\varrho\sigma} \frac{p_\varrho q_\sigma}{m_N^2} W_3 \\ + \frac{q^\lambda q^\mu}{m_N^2} W_4 + \frac{p^\lambda q^\mu + q^\lambda p^\mu}{m_N^2} W_5 \ . \end{aligned} \tag{1.10}$$

where p refers to the momentum of neutron, and q is the momentum transfer.

From Eq. (1.9) and Eq. (1.10), one can get

$$L^{\lambda\mu} W_{\lambda\mu} = 16 \sum_i W_i \left(\frac{A_i}{m_N^2} \right), \tag{1.11}$$

the kinematical factor A_i's are,

$$
\begin{aligned}
A_1 &= m_N^2(k \cdot k'), \\
A_2 &= (k \cdot p)(k' \cdot p) - \frac{A_1}{2}, \\
A_3 &= (k \cdot p)(k' \cdot q) - (k \cdot q)(k' \cdot p), \\
A_4 &= (k \cdot q)(k' \cdot q) - \frac{q^2}{2}\frac{A_1}{m_N^2}, \\
A_5 &= (k \cdot p)(k' \cdot q) + (k' \cdot p)(k \cdot q) - (q \cdot p)\frac{A_1}{m_N^2},
\end{aligned}
\tag{1.12}
$$

More different structure functions expressions for the quasi-elastic scattering and resonance production could be found in Ref. [8].

1.5 Electron Scattering

Electron scattering is one of the most widely used tools to study the nucleus structure. Due to the fact that electron has no internal structure and could be treated as a point particle, electron beam is a clean probe of the target nucleus. The scattering process between electron and nucleus could be described as the exchange of single virtual photon. Considering the restriction $Q^2 = q^2 - \omega^2 > 0$, and photon carries energy ω and 3-momentum $\mathbf{q}$, we can plot the spatial distributions of the nuclear charge and current densities by varying $\mathbf{q}$ with ω fixed. Furthermore, electron scattering method could provide us more details about the target nuclear structure, through the cross section measurement at various kinematics.

The primary purpose of E12-14-012 experiment is to measure the spectral functions of Argon and Titanium through (e,e′p) reactions. Five kinematics with different final electron energies and scattering angles were setup. We collected data on both inclusive (e,e′) and exclusive (e,e′p) reactions. More details about inclusive and exclusive processes will be described in

the following.

1.5.1 Inclusive Cross Section (e,e')

Inclusive electron scattering is a useful tool to study short range nuclear reactions. In the experiments based on inclusive (e,e′) reaction, after electron beam hit the target, the outgoing electrons will be detected by the spectrometer set at a particular momentum and angle. No specific reaction channel is chosen during this kind of experiments and all processes that related to production of the scattering electron are measured. Thus, this kind of experiments is called inclusive. Figure (1.2) shows the inclusive (e,e′) cross section as a function of ω, for a fixed value of $Q^2 = q^2 - \omega^2$ [11].

The first peak in Fig. (1.2) is the elastic peak. It is located at $\omega = \frac{Q^2}{2M_A}$ (where M_A is the mass of the nucleus). This peak represents the elastic electron scattering from the nucleus as a whole. When ω gets higher, a few sharp peaks followed by the elastic peak mean the target nucleus is excited to discrete states. The broad bump after the discrete part of the spectrum correspond to excitation of collective modes and it is called the giant resonance region. Next is the quasielastic peak near $\omega = \frac{Q^2}{2M_N}$ (where M_N nucleon mass). This peak corresponds to the elastic scattering off a free single nucleon. At higher energy transfer, we can find a few bumps like Δ and N^* resonances which indicates the nucleon excitation region. When the energy goes even higher, we have the electron scattering off quarks, which results in the breakup of the nucleon. This is the so-called deep inelastic scattering region.

For the inclusive (e,e′) process, like Fig. 1.3 shows,

$$e(k_i) + A(p) \rightarrow e'(k_f) + X(p') \ , \tag{1.13}$$

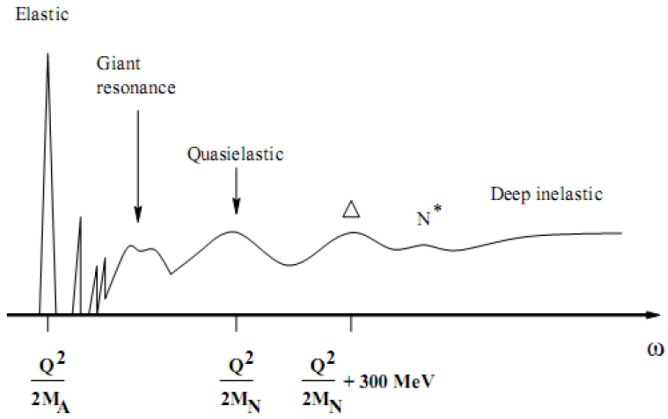

Figure 1.2: Example of the typical (e,e′) reaction energy spectrum

.

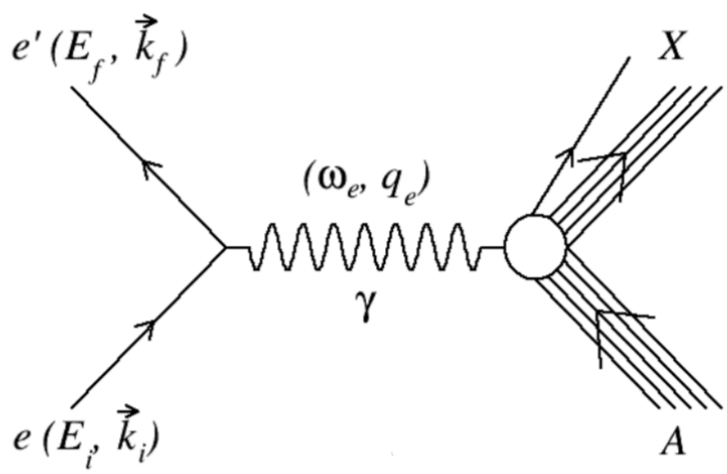

Figure 1.3: Feynman diagram of the Quasi-Elastic e-nucleus scattering

.

1.5.2 Exclusive cross section

Since inclusive cross section includes data from many exclusive channels, it is hard to evaluate the individual contributions of the different channels in the data. On the other hand, exclusive cross section provides a better way to study single-nucleon properties. Data taking of the exclusive (e,e′p) reaction comes from the use of two different spectrometers. One spectrometer detects the out-going electron, and the other one detects and analyzes the

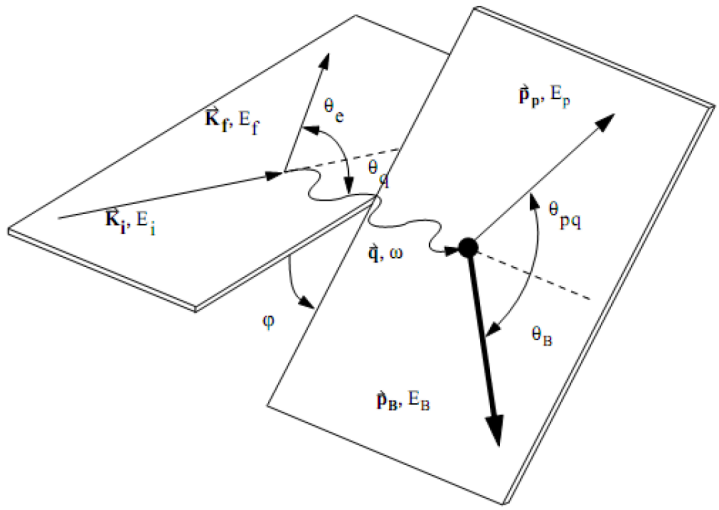

Figure 1.4: Schematic of the (e,e′p) reaction [12]

.

knocked-out nucleon. These two measurements are carried simultaneously.

Figure 1.4 illustrates the exclusive (e,e′p) reaction. Left side is the electron-scattering plane. The incident and outgoing electron momenta are fixed. θ_e is the electron-scattering angle. The other side is nuclear-scattering plane, with momentum transfer $\vec{q}$ and the knocked-out proton momentum $\vec{p_p}$. The angle between momentum transfer $\vec{q}$ and proton momentum is defined as θ_{pq}. The out-of-plane angle ϕ is the angle between electron and nuclear scattering planes.

If $\phi = 0°$ or $\phi = 180°$, the electron scattering and nuclear-scattering measurements will be in the same plane. Parallel kinematics indicates a particular kinematic space where the momentum of the knocked-out nucleon is parallel to the $\vec{q}$. All the five kinematic setups in the JLab E12-14-012 experiment are parallel.

The quantities measured in the exclusive (e,e′p) scattering are the initial 4-momenta of the beam electron $k_i = (E_i, \mathbf{k}_i)$, the final 4-momenta of the electron $k_f = (E_f, \mathbf{k}_f)$, and the 4-momenta of the scattered proton $p_p = (E_p, \mathbf{p}_p)$. $\mathbf{k}_i$, $\mathbf{k}_f$ and $\mathbf{p}_p$ can be measured from

the experiment. In normal case, electron mass is neglected so we could get $E_i \approx |\mathbf{k}_i|$ and $E_f \approx |\mathbf{k}_f|$. The total energy of the detected proton $E_p = \sqrt{M_p^2 + \mathbf{p}_p^2}$, where M_p is the rest mass of proton. The 4-momentum transfer could be given from the energy-momentum conservation

$$q = k_i - k_f = (\omega, \mathbf{q}) \tag{1.14}$$

The missing energy is given by

$$E_{miss} \equiv \omega - T_p - T_B \tag{1.15}$$

Where T_p and T_B are the kinetic energies of the ejected proton and the recoil nucleus, respectively. We also have

$$T_p = \sqrt{\vec{p_p}^{\,2} + m_p^2} - m_p \tag{1.16}$$

$$T_B = \sqrt{\vec{p_B}^{\,2} + M_B^2} - M_B. \tag{1.17}$$

With the momentum and energy conservation law,

$$\vec{p}_{miss} = \vec{p}_p - \vec{q} = -\vec{p}_B. \tag{1.18}$$

$$E_i + M_A = E_f + E_P + E_B \tag{1.19}$$

$$\omega = E_p + E_B - M_A = (m_p + T_p) + (M_B + T_B) - M_A \tag{1.20}$$

By plugging the equations above into Eq. (1.15), results in

$$E_{miss} = m_p - M_A + M_B, \tag{1.21}$$

We can rewrite the residual mass in terms of energy and momentum,

$$E_B = \omega + M_A + E_p, \tag{1.22}$$

$$\begin{aligned} M_B &= \sqrt{E_B^2 - \vec{p}_B^2} \\ &= \sqrt{E_B^2 - \vec{p}_{miss}^2} \\ &= \sqrt{(\omega + M_A - E_p)^2 - \vec{p}_{miss}^2} \end{aligned} \tag{1.23}$$

Therefore, the missing energy is,

$$E_{miss} = m_p - M_A + \sqrt{(\omega + M_A - E_p)^2 - \vec{p}_{miss}^2}. \tag{1.24}$$

This expression shows that the missing energy calculation does not depend on the knowledge of the residual system.

The invariant cross section is defined as in Ref. [11]

$$d\sigma = \frac{1}{(2\pi)^3}\frac{E_f}{E_i}\frac{\alpha^2}{Q^4}\eta_{\mu\nu}W_{\mu\nu}dE_f d\Omega_e d^3\mathbf{p}_p, \tag{1.25}$$

where $d\Omega_e$ is the solid angle for electron momentum in the laboratory, $\eta_{\mu\nu}$ and $W_{\mu\nu}$ are the electron and nuclear response tensors. Using

$$d^3\mathbf{p}_p = E_p p_p dE_p d\Omega_p \tag{1.26}$$

where $d\Omega_p$ is solid angle of the electron momentum in the laboratory reference frame. Six-fold differential cross section could be written as

$$\frac{d^6\sigma}{dE_f d\Omega_e dE_p d\Omega_p} = \frac{E_p p_p}{(2\pi)^3}\frac{E_f}{E_i}\frac{\alpha^2}{Q^4}\eta_{\mu\nu}W_{\mu\nu}. \tag{1.27}$$

The mass of the ultra-relativistic electron could be neglected, thus, the electron response tensor could be defined as

$$\begin{aligned}\eta_{\mu\nu} &= 2(k_{i\mu}k_{f\nu} + k_{f\mu}k_{i\nu} - k_i k_f g_{\mu\nu}) \\ &= K_\mu K_\nu - q_\mu q_\nu - Q^2 g_{\mu\nu}\end{aligned} \tag{1.28}$$

where $K_\mu = k_{i\mu} + k_{f\mu}$, and $q_\mu = k_{i\mu} - k_{f\mu}$.

The nuclear response tensor matrix is the products of the nuclear current matrix elements, while averaging over initial states and summed over final states

$$W_{\mu\nu} = \langle J_\mu J_\mu^\dagger \rangle. \tag{1.29}$$

Applying the current conservation and the continuity equation, one can get

$$q_\mu W^{\mu\nu} = W^{\mu\nu} q_\nu = 0, \tag{1.30}$$

$$J_z = \frac{\omega}{\vec{q}}\rho. \tag{1.31}$$

After some math derivation, the contraction of electron and nuclear response tensors could be reduced to

$$\eta_{\mu\nu} W_{\mu\nu} = 4E_i E_f \cos^2\frac{\theta_e}{2}[V_L R_L + V_T R_T + V_{LT} R_{LT} cos\phi + V_{TT} R_{TT} \cos 2\phi]. \tag{1.32}$$

The kinematic factors could be written as

$$\begin{aligned} V_L &= \frac{Q^4}{\vec{q}^4} \\ V_T &= \frac{Q^2}{2\vec{q}^2} + \tan^2(\frac{\theta_e}{2}) \\ V_{LT} &= \frac{Q^2}{\vec{q}^2} + \left[\frac{Q^2}{\vec{q}^2} + \tan^2(\frac{\theta_e}{2})\right]^{\frac{1}{2}} \\ V_{TT} &= \frac{Q^2}{2\vec{q}^2}, \end{aligned} \tag{1.33}$$

In terms of the nuclear current tensor, the response functions are

$$
\begin{aligned}
R_L &= \langle W_{00} \rangle = \langle \rho\rho^\dagger \rangle \\
R_T &= \langle W_{xx} + W_{yy} \rangle = \langle J_\parallel J_\parallel^\dagger + J_\perp J_\perp^\dagger \rangle \\
R_{LT} \cos\phi &= -\langle W_{0x} + W_{x0} \rangle = -\langle \rho J_\parallel^\dagger + J_\parallel \rho^\dagger \rangle \\
R_{TT} \cos 2\phi &= \langle W_{xx} - W_{yy} \rangle = \langle J_\parallel J_\parallel^\dagger - J_\perp J_\perp^\dagger \rangle,
\end{aligned}
\tag{1.34}
$$

where ρ is the charge component of the nuclear current. $J_\parallel$ is the transverse component of the nuclear current in the scattering plane. $J_\perp$ is the transverse parameter orthogonal to the scattering plane. Both $J_\parallel$ and $J_\perp$ are orthogonal to $\vec{q}$. R_L is the longitudinal response function from the charge and the longitudinal component of the current. R_T is the transverse response function arises from the sum of the two transverse components of the nuclear current. R_{TL} is the transverse-longitudinal interference response function related to the transverse current and the longitudinal component of the nuclear current in the scattering plane. R_{TT} is the transverse-transverse interference response function of the two transverse components of the nuclear current. Generally speaking, R_L, R_T, R_{TL} and R_{TT} are functions of kinematic variables. All of these information could be calculated in the (e,e′p) reaction.

1.6 Final State Interactions (FSI)

The knocked-out nucleon could interact with nucleons before exiting the nucleus. This is clearly included in data but in the case of the E12-14-012 experiment is not part of the Monte Carlo simulation. For low energy (e,e′p) process, FSI could be described in terms of the interactions of the knocked-out nucleon with a complex optical potential.

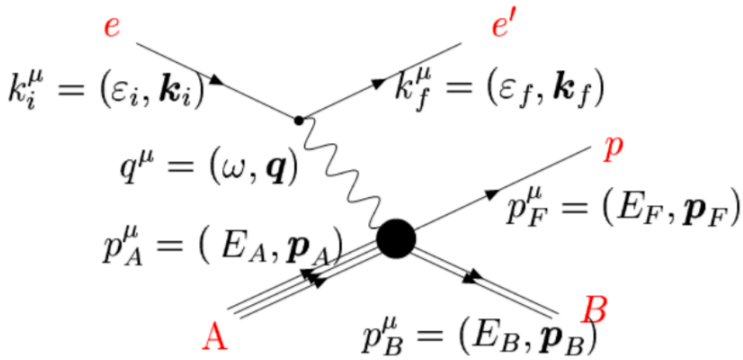

Figure 1.5: A diagram of the PWIA in the (e,e′p) reaction [12].

1.6.1 Impulse Approximation

Because of the inadequacy of the Born approximation in the nuclear force case [13], it is hard to study nuclear collision system involving more than two nucleons. To simplify, usually this kind of problem is decomposed into a superposition of simple two-body collision [14]. Impulse approximation is another expression sharing the same thought. It assumes that the exchanged virtual photon only interacts with the detected nucleon.

1.6.2 Plane Wave Impulse Approximation (PWIA)

Based on the impulse approximation, if the knocked-out proton is further assumed no interaction with the residual nucleus, this nucleon could be described using plane wave impulse approximation (PWIA), as Fig. 1.5 shows.

In non-relativistic PWIA, we can factorized the six-folder cross section as in Ref. [15]

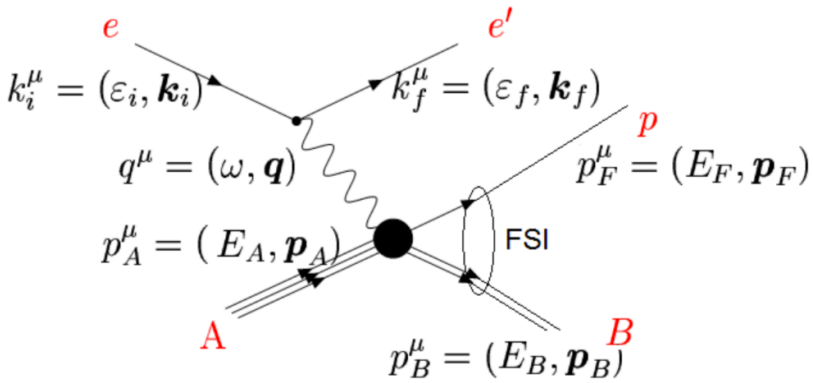

Figure 1.6: DWIA in (e,e′p) reaction [12].

$$\begin{aligned}\frac{d^6\sigma}{dE_f d\Omega_e dE_p d\Omega_p} &= R{\cdot}K{\cdot}\sigma_{ep}{\cdot}S(E_{miss}, \vec{p}_{miss}) \\ &= \frac{E_p p_p}{(2\pi)^3}{\cdot}\sigma_{ep}{\cdot}S(E_{miss}, |\vec{p}_{miss}|)\end{aligned} \tag{1.35}$$

where R is the recoil factor, $K \equiv E_p p_p$. σ_{ep} is the off-shell cross section [16] and S is the spectral function, represents the probability to find a proton with initial momentum $|\vec{p}_{miss}|$ and binding energy E_{miss} inside the initial nucleus.

1.6.3 Distorted Wave Impulse Approximation (DWIA)

In the Distorted Wave Impulse Approximation (DWIA), final state interactions between the knocked-out proton and the residual nucleus is taken into account. The DWIA process is shown in Fig. 1.6.

Considering the fact that FSI effect also depends on the momentum of the knocked-out nucleons, (e,e′p) could be rewritten using the distorted spectral function,

$$\begin{aligned}\frac{d^5\sigma}{dE_f d\Omega_e dE_p d\Omega_p} &= \frac{E_p p_p}{(2\pi)^3}\sigma_{ep} S^D(E_{miss}, \vec{p}_{miss}, |\vec{p}_p|) \\ &= R{\cdot}K{\cdot}\sigma_{ep}{\cdot}S^D(E_{miss}, \vec{p}_{miss}, |\vec{p}_p|)\end{aligned} \tag{1.36}$$

Note that the distorted spectral function S^D not only depends on E_{miss} and $\vec{p}_{miss}$, but also upon the proton momentum $|\vec{p}_p|$.

In the JLab E12-14-012 experiment, FSI effect need to be considered. Our data contains naturally FSI, but the Monte Carlo simulation does not include FSI corrections other than for the nuclear transparency. It is necessary to add the FSI corrections to the Monte Carlo simulation results. More details will be discussed in later section and in the included published papers.

Chapter 2

JLab E12-14-012 Experimental Setup

2.1 Overview

The JLab E12-14-012 [17] experiment has been proposed to obtain the Argon spectral function, through the analysis of the nuclear (e,e′p) cross section. It ran in Spring 2017 and was performed in Hall A of the Thomas Jefferson National Accelerator Facility.

Several targets were used in the E12-14-012 experiment. Argon target is a gas cell, major part of the data was taken using this target. Two Aluminum blocks were used as dummy target to study the experiment background. More details about the target setup will be described later.

In Hall A, a pair of identical 4 GeV/c spectrometers are installed.

In our experiment, we used both spectrometers to detect scattered electrons and knocked-out protons, respectively.

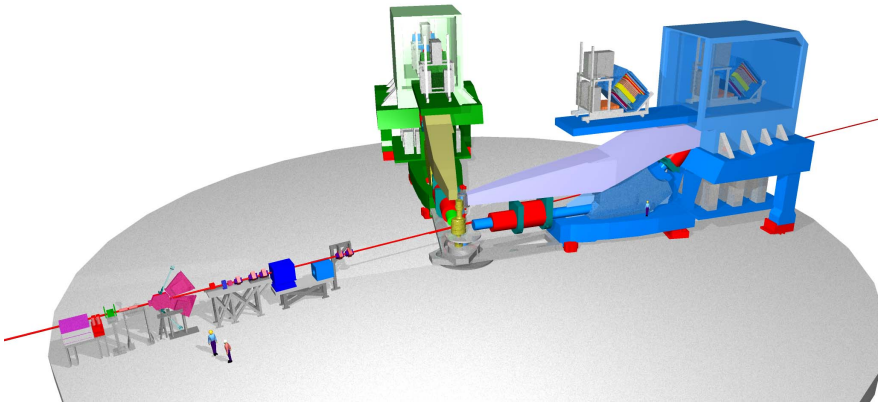

Figure 2.1: A picture of Jefferson Experimental Hall A [18].

2.2 Beamline

2.2.1 Beam Current Measurements

The beam current monitor (BCM) consists of an Unser monitor, two RF cavities, bunch of electronic systems and a data-acquisition (DAQ) system [19]. A box consists of the cavities and the Unser monitor is placed 25 m upside of the target. All the rest part of the BCM is located in the control room.

The Unser monitor provides an absolute reference to the beam current. It cannot be treated as continuously beam current monitor due to the large output signal drift happening in a shot period (usually several minutes).

The RF cavity located at two sides of the Unser monitor are cylindrical waveguides made of stainless steel [19]. Their output voltages are proportional to the beam current. The output signal of the RF cavity is split into a sampled and an integrated part.

The sampled part is sent to an AC voltmeter to provide average beam current for each second. For the integrated data part, it is converted through an RMS-to-DC converter. The output signal will be used to represent the total beam charge.

2.2.2 Beam Position Measurements

The position and direction of the beam is determined by two Beam Position Monitors (BPMs) located upstream of the target. BPM is made of four open-ended antennas. The relative position can be found within 100 μm for current above 1 μA [19, 20]. By calibrating the BPMs to wire scanners, the absolute position of the beam could be determined.

The position information from the BPMs could be recorded into the EPICS database in average value or into the CODA data stream event-by event.

2.2.3 Beam Energy Measurements

The beam energy is measured in two different ways.

The Arc method [19], which is based on the fact that the electron motion can be affected by magnetic field. It determines the missing momentum of the beam by measuring the magnetic field magnitude and the net bend angle.

$$p = k\frac{\int \vec{B} \cdot \vec{dl}}{\theta}, \tag{2.1}$$

where p is in GeV/c, $k = 0.299792\text{GeV} \cdot \text{rad} \cdot \text{T}^{-1} \cdot \text{m}^{-1}/c$. $\int \vec{B} \cdot \vec{dl}$ is the integral of the eight dipoles in $\text{T} \cdot \text{m}$ and θ is the net bend angle in rads.

In the e-P measurement, we could determine the beam energy by measuring the incoming

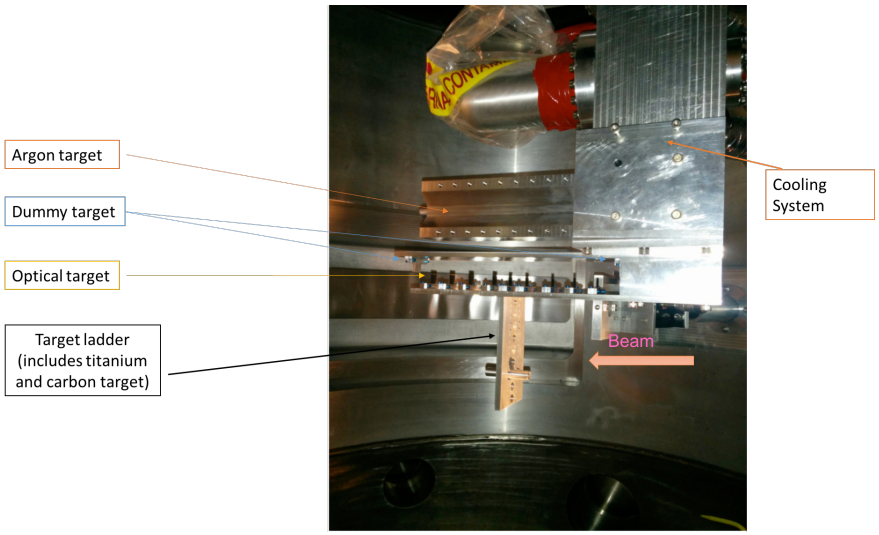

Figure 2.2: Side view of the target system of JLab E12-14-012.

electron and outgoing proton angles in the H(e,e′p) elastic reaction [19].

2.3 Target System

In the JLab E12-14-012 experiment, five targets were included in the data taking for different purposes. As shown in Fig. 2.2, the right side aluminium box is the cooling system to make sure our target system will not be overheated by the high energy beam. Electron beam comes from right to left. From top to bottom, we have argon, dummy, optical targets and the target ladder which has titanium and carbon targets on it. The whole target system could move freely up and down to adjust the beam position.

The argon target is designed to measure the coincidence (e,e′p) cross section on argon. It is a closed gas cell with 25 cm long. Figure 2.3 shows the design structure of the argon target. Figure 2.4 is a photo of the argon target. The whole body is made of Aluminum. The fill temperature of the cell is 291 K, the fill pressure of the cell is 500 psi. The density of the argon gas without beam on target is 58.2 kg/m^3. The length and density are chosen to be

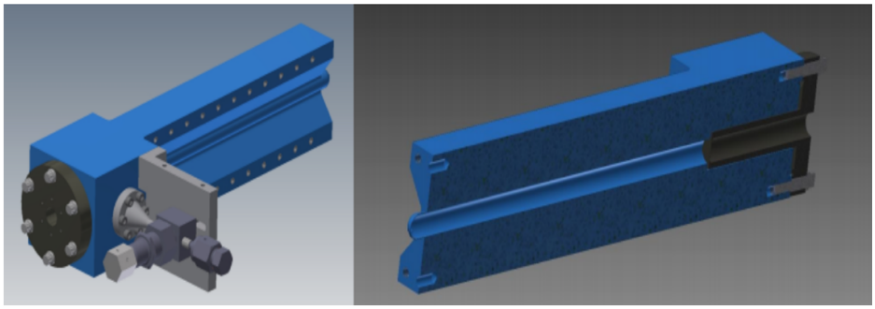

Figure 2.3: Technical 3D drawing of the argon target.

about 0.3 radiation length to avoid major re-interactions of the secondary electrons in the target gas medium. The gas density in the target will change when the beam turned on due to the heat deposited by the beam in the target gas. We call this the "boiling effect". The beam passing through the target center will heat the gas around it. This causes the uneven distribution of the temperature inside the gas cell and it will create fluid motion in the gas cell. The density of the gas is lower around the center compared to the edge space. We performed some detail studies of this effect and they are described in Ref. [21].

The dummy targets are aluminum foils mounted on separate frames just below the main gas target. They are placed at the same position as the argon target exit and entrance windows separately. Electrons will interact in the entry and exit window of the gas target, and we can use this target to determine the background from the aluminum blocks,

The optics target includes a series of nine carbon foils placed evenly along the Z direction, as Fig 2.4 shown. It is used to check the target alignment, the optical alignment and the acceptances of the spectrometers.

The titanium target is a solid target located at Z=0 on the target ladder. It is a 1.5 mm thick natural titanium foil. We can use this target to measure the coincidence (e,e′p) on titanium. We are interested in the neutron spectral function of argon, but measuring the (e,e′n) process is very difficult. The proton shell structure of titanium is very similar to the

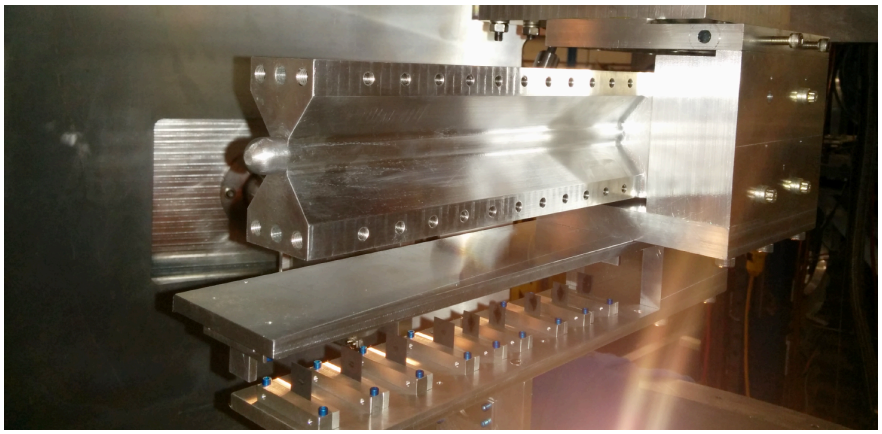

Figure 2.4: Picture of the several targets used during the JLab E12-14-012 experiment. The top aluminium cell is the argon gas cell. The nine carbon foils are visible, mounted just below the gas cell.

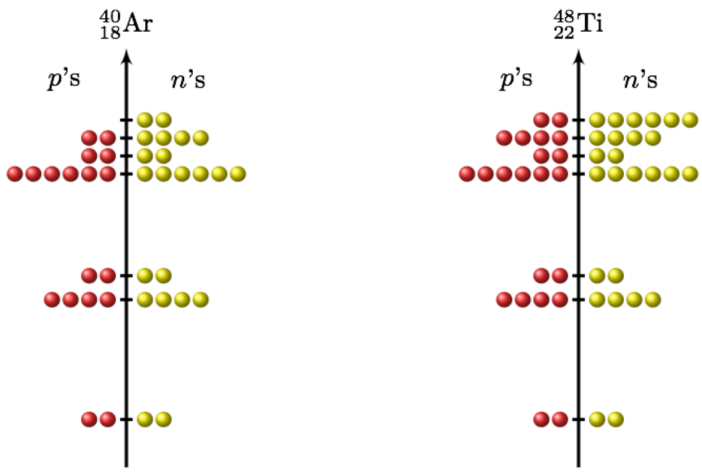

Figure 2.5: Schematic of the shell model structures of argon and titanium [22].

neutron shell structure of argon (see Fig. 2.5). Measuring cross section on titanium will help us study the proton and neutron interactions with neutrinos of argon in neutrino oscillation experiments.

The carbon target is a solid target similar to the titanium target. Its thickness is 0.167 g/cm^2. There is a lot of previous electron scattering data in C. Measuring the carbon cross section helps us validate our data analysis by comparing with previous carbon results.

The thickness of the argon, titanium, carbon and dummy targets are matched to have the same radiation length.

2.4 High Resolution Spectrometers (HRSs)

A pair of spectrometers is the major equipment in Jefferson Lab Hall A. The left arm HRS is used to detect outgoing electrons while the right arm HRS is used to detect the knock-out protons. These two spectrometers are quasi-identical with momentum resolution up to 2×10^{-4} and high position and angular resolution. The full list of the spectrometer characteristics are listed in Tab. 2.1 [19].

Table 2.1: Main characteristics of the Hall A HRSs [19].

Configuration	QQD$_n$Q Vertical bend
Bending angle	45°
Optical length	23.4 m
Momentum range	0.3 - 4.0 GeV/c
Momentum acceptance	-4.5% < δp/p <+4.5%
Momentum resolution	2×10^{-4}
Angular acceptance (Horizontal)	±30 mrad
Angular acceptance (Vertical)	±60 mrad
Angular resolution (Horizontal)	0.5 mrad
Angular resolution (Vertical)	1.0 mrad
Solid angle at δp/p = 0, $y_0 = 0$	6 msr
Transverse length acceptance	±5 cm
Transverse position resolution	1 mm

Each HRS follows the vertically bending design. Its magnet configuration is QQDQ, which consists of three quadrupoles and a dipole. Figure 2.6 shows the layout of this configuration. The first two quadrupoles in front of the dipole help meet the angular acceptance standard and maximize the resolving power by generating a parallel beam. The following dipole bend the beam 45 degree and help simplify the magnet configuration design. The third quadrupoles after the dipole increases horizontal position and angular resolution.

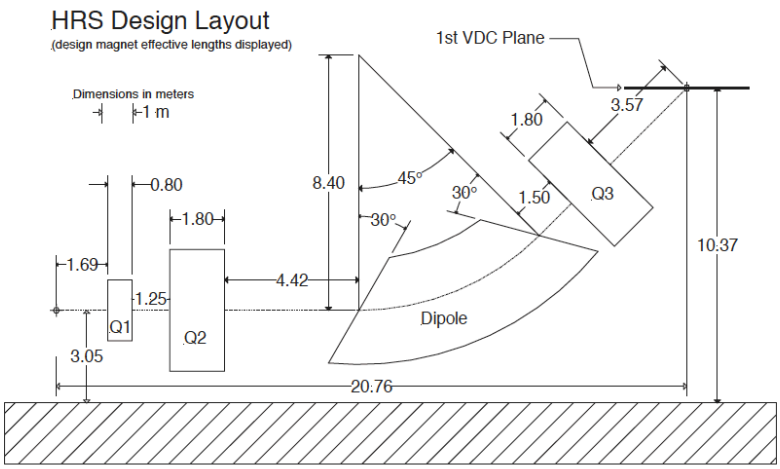

Figure 2.6: Schematic layout of the spectrometer magnet configuration (QQDQ) [19].

2.5 Detector Package

The detector packages for left and right arm HRSs are a bit different as shown in Fig. 2.7. Both spectrometers have trigger setting to activate the data acquisition (DAQ) system, identical vertical drift chambers for tracking information, two scintillator planes which provides the timing information. The only difference between the two HRS is the particle identification detector. Left arm uses a gas Cherenkov and calorimeter to detect outgoing electrons and the right arm use a pre-shower and shower to distinguish between pions and protons.

2.5.1 Vertical Drift Chambers

The vertical Drift Chambers (VDCs) are used to provide tracking information of the outgoing particles [24]. Each spectrometer has a pair of VDCs. The lower VDC is placed at most closest position related to the focal plane. The upper VDC is located parallel above the lower one. The distance between VDC planes is 0.335 m (shown in side view part of Fig. 2.8).

Each VDC has two wire planes, these planes are in a standard UV configuration. The U

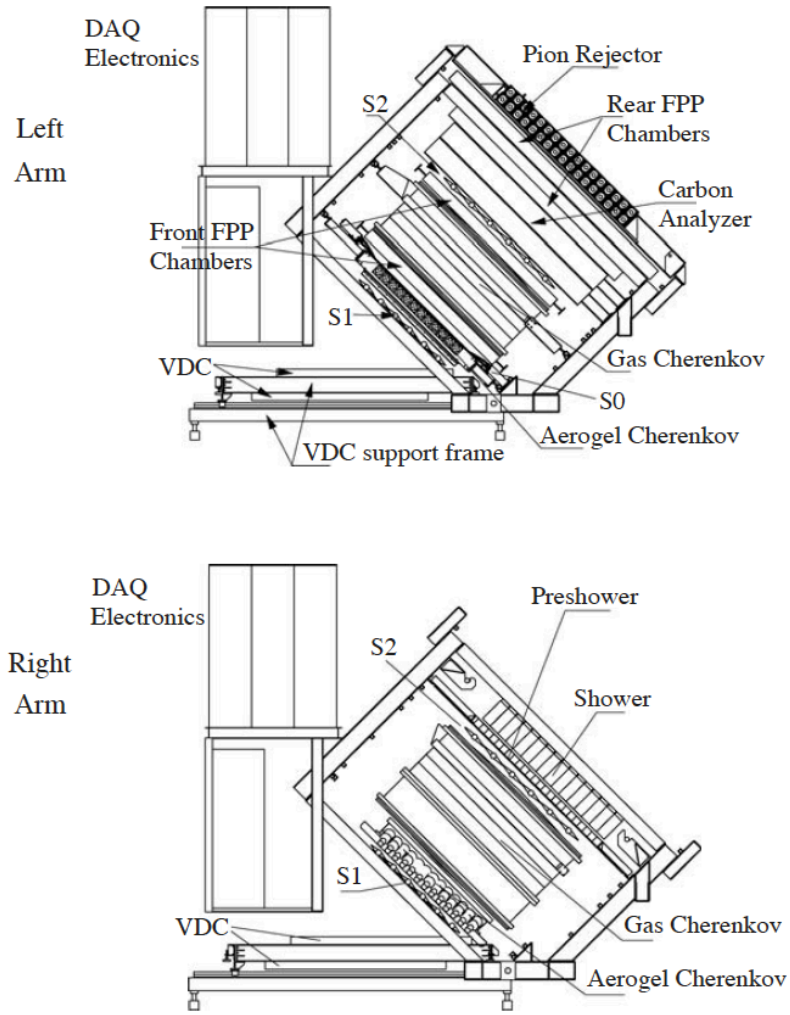

Figure 2.7: HRS detector stack. All the detectors for different experiment are shown in the diagram. Figure is from Ref. [19]

and V wires are orthogonal to each other, inclined at 45(degree) from the normal particle trajectory (shown in top view part of Fig. 2.8). Each plane has 368 wires and they are spaced 4.24 mm apart.

Two Mylar planes are placed above and below each wire plane, an -4.0 kV electric field of the VDCs is generated by these Mylar planes. The standard gas mixture used inside chambers are 62% argon and 38% ethane [19].

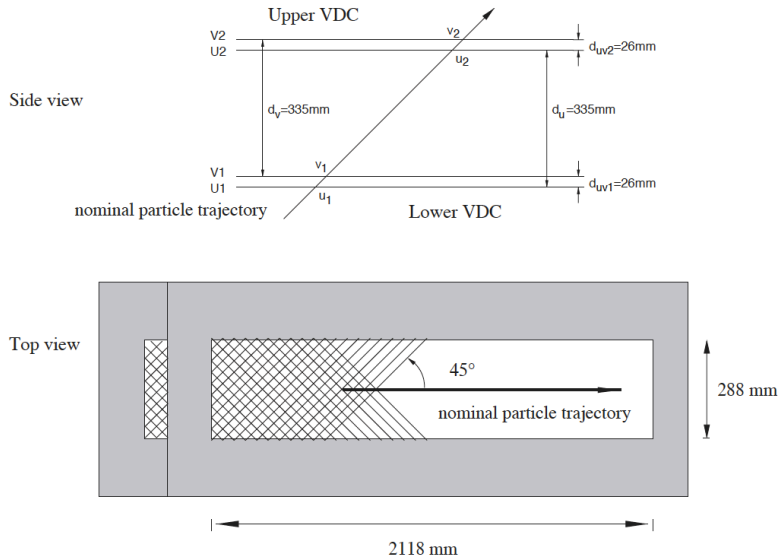

Figure 2.8: Schematic diagram of the Hall A HRS VDCs [19].

Particle trajectories can be reconstructed using VDCs' data. When a particle pass through the VDC, electrons would be ionized and accelerated by inside electric field and moving towards the closest sense wires (Like Fig. 2.9 shows). The drift time information is measured by TDCs and converted to the distance between the wire plane and the trajectory. In general, the system will generate about 5 read-out signal for each particle passing through the wire plane. These TDC signals can be used to find the exact position the particle hit the plane. Then, four hitting locations in four wire planes reconstruct the particle trajectory. The position resolution in the focal plane is 100 μm and the angular resolution is about 0.5 mrad.

2.5.2 Scintillators

After the VDCs, two scintillator planes S0 and S2m are used to provide time-of-flight information. When a particle passes through the plane, atoms in the scintillator get exited, and then returned to normal state quickly by generating a bunch of photons, which could be received by the PMTs at two sides. The process provides the whole system a trigger signal

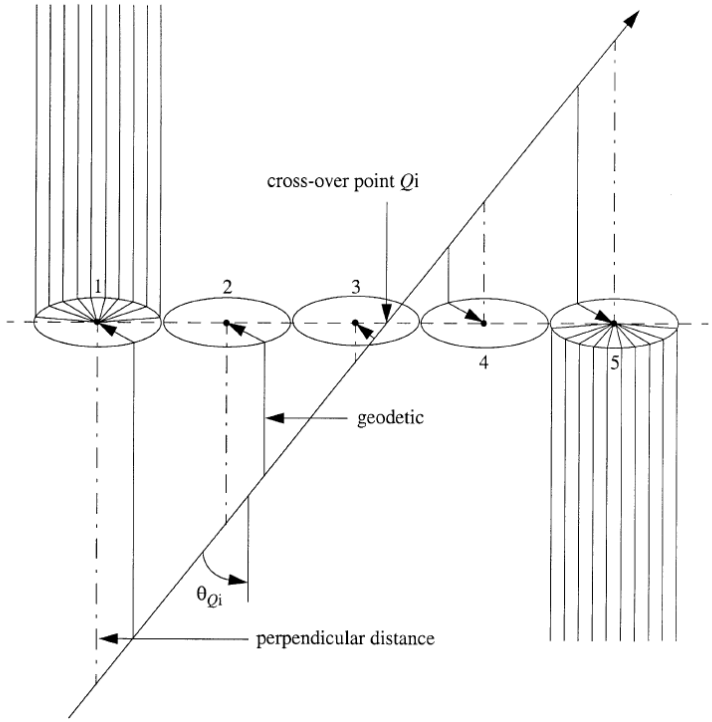

Figure 2.9: A typical VDC track example. The continuous lines represent the path of least travel time distance between ionized electron and sense wires. The dot-dashed lines are the distance projection to reconstruct the trajectory [24].

with time information included.

These two scintillators are placed parallel to each other and separated by 1.6 m. Scintillators have fast reaction to the happening signal with very high resolution (30 ns), thus, they are generally used to form the trigger system. The trigger settings for our experiment will be discussed in Sec. 2.6.

Each scintillator paddle is viewed by two photomultiplier tubes (PMTs). S0 only has one plastic paddle, and S2m has 16 overlapping paddles.

2.5.3 Gas Čerenkov detector

While a high energy charged particle moving in a medium with the speed faster than that of light, it can radiate Čerenkov light [25]. The momentum threshold to emit Čerenkov light depends on the mass of the particle and the medium property:

$$p_{threshold} = \frac{mc}{\sqrt{n^2 - 1}}, \tag{2.2}$$

The momentum threshold for electrons and pions to emit Čerenkov light is 0.017 GeV/c and 4.8 GeV/c separately. The angle between the track of the charged particle and the direction of Čerenkov light is given by:

$$\cos\theta = \frac{1}{\beta n}, \tag{2.3}$$

where n is the index of reflection of the medium. $\beta = v/c$ is the ratio of the charged particle's velocity in the medium over the speed of light.

A gas Čerenkov detector is mounted between S0 and S2m on each spectrometer. The detector box is filled with atmospheric pressure CO2. It has ten well arranged spherical mirrors to collect the Čerenkov light and focus it into the corresponding PMTs (See Fig. 2.10.

In our experiment, the gas Čerenkov works well to distinguish between electrons and pions, considering the momentum coverage of the HRS is from 0.3 to 4 GeV/c, only electrons could emit Čerenkov light. Though pions still have very low possibility to produce signals by interacting with the gas, this process is negligible compared with the background signal.

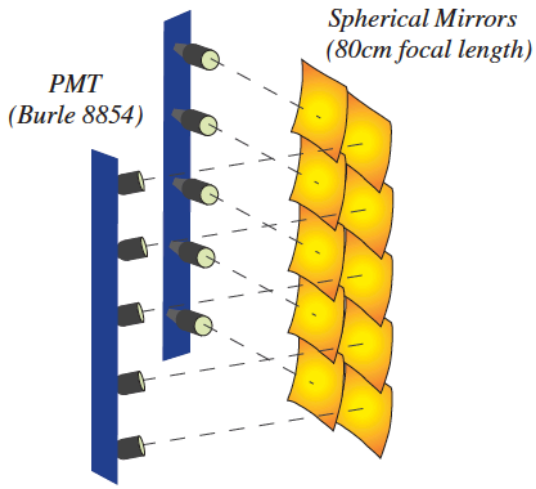

Figure 2.10: A diagram showing the spherical mirrors and PMTs inside the Gas Čerenkov [26].

2.5.4 Lead Glass Calorimeter

The calorimeter mounted behind S2m in each HRS provides the energy measurement for each charged particle passing through it. Each calorimeter is composed of two layers of lead glass blocks and associated PMTs.

Both spectrometers have two layers of calorimeters. The structure of the calorimeters are shown in Fig. 2.11 . The two layers in HRS_L are similar, each layers consists of 34 lead glass blocks, with 15 cm × 15 cm × 30 cm in 3-D dimensions. The front layer in HRS_R has 48 lead glass blocks. All the blocks in both layers in HRS_L and the first layer in HRS_R are perpendicular to the particle tracks. The second layer of HRS_R is composed of 80 lead glass blocks and oriented parallel to the particle tracks.

When passing through the dense material in calorimeter, a high energy electron will transfer its energy into photons through Bremsstrahlung radiation. The emitted photons repeatedly generate more Bremsstrahlung radiation through electron-positron pair production. A shower of photons could be developed along the particle traveling path, and detected by the

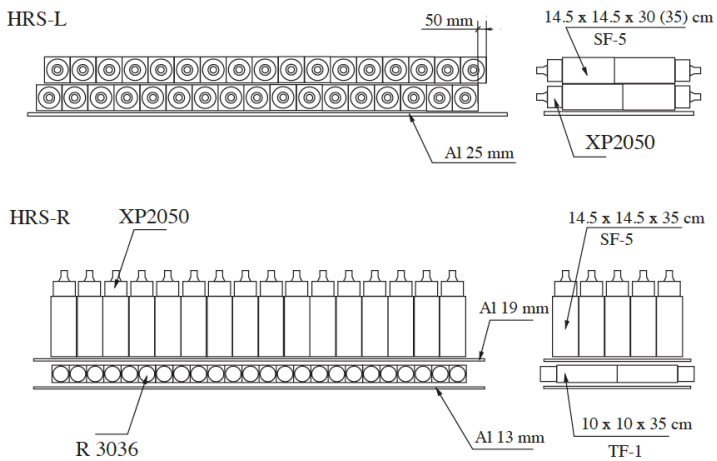

Figure 2.11: Schematic layout of the calorimeters in both the HRS_L and the HRS_R [19].

PMTs. At the GeV energy scale, only electrons could deposit its energy inside calorimeter, which provides another substantial particle identification method in addition to the gas Cerenkov detector.

2.6 Trigger System

In the JLab E12-14-012 experiment, the scattered electrons are measured by left arm HRS and the knock-out protons are detected by the right arm HRS. Three detector planes (S0, S2m and GC) and calorimeter are included in the trigger system design. We set up 6 triggers totally, the trigger system is shown in Fig. 2.12. All the triggers are logical AND and OR of S0, S2m, GC and calorimeter.

T3 is designed as the left arm triggers. The coincidence of logic signals from S0, S2m and GC (or Calorimeter) created T3 trigger in left arm HRS. T4 is the right arm trigger, which is the coincidence of logic signals from S0 and S2m. T1 is the coincidence signal of T3 and T4, which is the production trigger in the experiment.

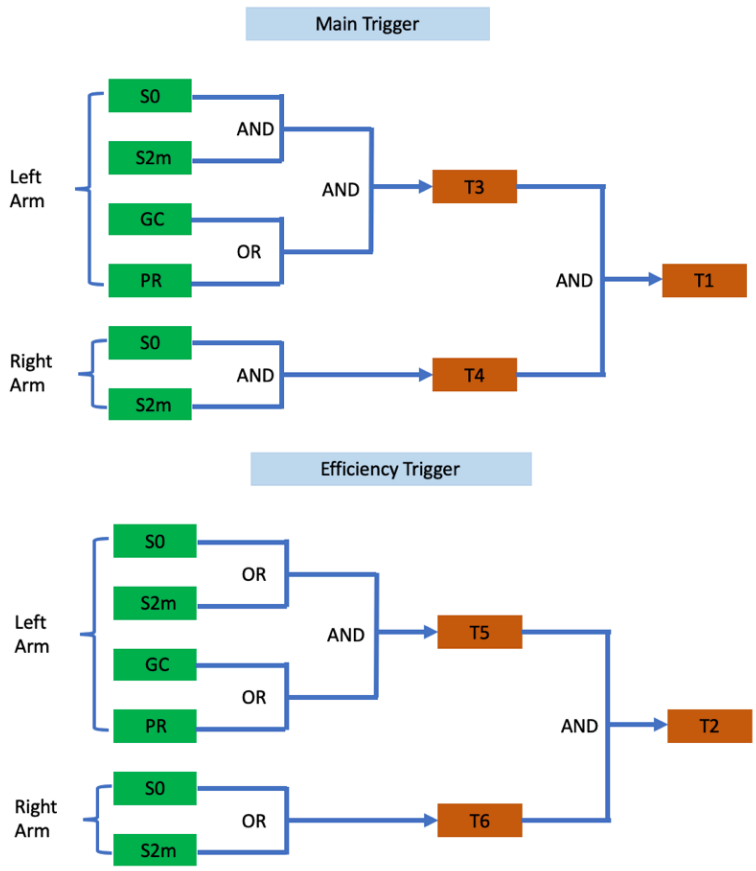

Figure 2.12: Layout of the trigger design for the E12-14-012 experiment [22].

In order to measure the trigger efficiencies of these main triggers, T2, T5 and T6 are designed. For example, T2 is formed by the logical OR of T5 and T6, it is the efficiency trigger of T1.

2.7 Data Acquisition

In the JLab E12-14-012 experiment, we have five kinematic setups for (e,e′p) reactions for argon, titanium, aluminum, carbon and optical targets. We also have one kinematic settings for (e,e′) reactions for all five targets used. The energy of the beam used is 2.222 GeV. The missing momentum ranges from dozens to 300 MeV for all five kinematics.

Table 2.2 shows a summary of the data taking and Tables 2.3 contains detailed settings for different kinematics.

Table 2.2: Data taking summary [22]

Kin1			Kin3		
Target Type	Hours	Events(k)	Target Type	Hours	Events(k)
Ar	29.6	43,955	Ar	13.5	73,176
Ti	12.5	12,755	Ti	8.6	28,423
Dummy	0.75	955	Dummy	0.6	2,948
Kin2			**Kin4**		
Target Type	Hours	Events(k)	Target Type	Hours	Events(k)
hline Ar	32.1	62,981	Ar	30.9	158,682
Ti	18.7	21,486	Ti	23.8	113,130
Dummy	4.3	5,075	Dummy	7.1	38,591
Optics	1.15	1,245	Optics	0.9	4,883
C	2.0	2,318	C	3.6	21,922
Kin5			**Inclusive**		
Target Type	Hours	Events(k)	Target Type	Minutes	Events(k)
Ar	12.6	45,338	Ar	57	2,928
Ti	1.5	61	Ti	50	2,993
Dummy	5.9	16,286	Dummy	56	3,235
Optics	2.9	160	C	115	3,957

Table 2.3: Kinematic settings for (e,e′p) measurements, the central kinematic variables include beam energy (E_e), central momenta ($E_{e'}$, P_p), central angles (θ_e, θ_p), momentum transfer ($|\vec{q}|$) and central missing momentum (p_m) [22].

(e,e′p)	$E_e(MeV)$	$E_{e'}$(MeV)	$\theta_e(°)$	$P_p(MeV/c)$	$\theta_p(°)$	$\|\vec{q}\|$(MeV/c)	p_m(MeV/c)
kin 1	2,222	1,777	21.5	915	-50.0	857.5	57.7
kin 3	2,222	1,799	17.5	915	-47.0	740.9	174.1
kin 4	2,222	1,799	15.5	915	-44.5	658.5	229.7
kin 5	2,222	1,716	15.5	1,030	-39.0	730.3	299.7
kin 2	2,222	1,716	20.0	1,030	-44.0	846.1	183.9

Chapter 3

JLab E12-14-012 Experiment - Data Analysis

3.1 Extracting the Differential Cross Section

The raw data taken was processed using a common JLab C++ analysis macro for each of the experiment's kinematic. The data was then stored into special format file (rootfile), which contain event-by-event information on tracking, PID, angles, beam quantities and timing information.

The differential cross section could be extracted using two different methods: correction and ratio. The methods depends from the Monte Carlo simulation of the experiment in different ways, so using both would help decoupling the analysis from the Monte Carlo simulation. For the correction method, the measurement of the cross section for the (e,e′p) reaction needs to find luminosity L and overall efficiencies and corrections first. The luminosity is measured as the product of the total incident electrons and the target nuclei number per unit area

$$L = \left(\frac{Q}{e}\right) \cdot \left(t \cdot \frac{N_{AV}}{A}\right) \tag{3.1}$$

where Q is the total beam charge, e is the electron charge. N_{AV} represents Avogadro's number, A is the atomic weight and t is the target thickness in g/cm^2.

For (e,e′p) reaction, the cross section is six-fold differential estimated over a finite angular and momentum acceptances for electron and proton. The data was measured in the five-dimensional space $(E_{miss}, p_{miss}, q, \omega, \phi)$, through dividing the number of events by an effective luminosity L_{eff} and the phase space volume of the bin V_B, one can find the six-fold differential cross section for each bin.

$$\left\langle \frac{d^6\sigma}{d\omega d\Omega_e dT_p d\Omega_p} \right\rangle_B = \frac{N_B}{L_{eff} \cdot V_B} \tag{3.2}$$

$\langle\rangle_B$ refers to the averaged value in the phase space volume of the bin B. The theoretical cross section could be obtained with the central values of the bin. The effective luminosity L_{eff} contains all the efficiencies and corrections mentioned in the next section. The phase space volume V_B of each bin B could be written as

$$V_B = \int_B d\omega d\Omega_e dT_p d\Omega_p \tag{3.3}$$

This volume was estimated from the MC simulation.

The ratio method uses the same efficiency and correction factors. But the goal of this method is to obtain the Monte Carlo yield after simulating MC data using a specific cross section model. Data features like radiative corrections and spectrometer acceptance were applied to the Monte Carlo yield. If all the experimental features were included, we should expect an agreement of the yields from the MC and the experiment data.

In our data analysis, we used the data to MC ratio method, though the acceptance method (or ratio method) is less dependent from the MC input model, is more computational in-

tensive due to the fact that acceptances need to be computed for each of the data samples. Computing systematic uncertainties for the acceptance method is also much more complicated, due to the correlation between the data sample. We found in general very good agreement between the two methods. More details on the two methods and a more detailed description of the comparisons could be found in Ref. [27].

3.2 Efficiency Corrections

3.2.1 Deadtime Correction

We only consider the DAQ dead-time (CDT) in our analysis, which includes also the electronic and detector dead-times.

The dead-time correction is computed using the probability that a trigger would be accepted. From the electronic scalers we can count how many triggers were created, and we can also count how many triggers were accepted from the data written on the DAQ stream. To accurately compute the dead-time, it is more convenient to calculate live-time (LT), being the latter and former related by

$$LT = (1 - DT) \tag{3.4}$$

The live-time is the ratio between the number of triggers accepted by the DAQ and the sum of triggers sent to the DAQ. For example, for Trigger T1, the live-time is

$$LT = \frac{N_{T_1} \cdot ps_1}{N_1} \tag{3.5}$$

where N_{T_1} is the number of Trigger T1 recorded by DAQ, ps_1 is the pre-scaler of this trigger. N_1 is the total number of trigger T1 sent to DAQ.

The average live-time for the five different kinematics in our experiment is ∼95%, kinematic 1 having the highest live-time of 99%.

The uncertainty on our live-time calculation is less than 0.5%.

3.2.2 Trigger Efficiency

Our experiment trigger system uses three sub-detectors for each of the HRS: scintillators, pion rejector and gas Čerenkov. A detailed description of those detectors is presented in Chapter 2.5. The trigger efficiency considered for both spectrometers represent the probability that the out-going electron and knocked-out proton comes from the same primary electron interaction. The trigger is generated by the scintillator planes (coincidence signal between S0 and S2), the calculated trigger inefficiency results from the inefficiency of the scintillators and other detectors related to the generated triggers.

Table 5.2 shows detailed list of six triggers used in our experiment. S_0 and S_2 are two scintillator planes used. GC and PR are gas Čerenkov and pion rejector, respectively. PS_e represents pre-shower and shower detector. LEFT and RIGHT refer to electron and proton arm, separately.

The trigger efficiency is estimated by measuring the ratio of the events passing trigger T1 to the events surviving trigger T2. In other words, trigger efficiency is measuring the fraction of the good events passing through both scintillator planes instead of just one of them. Coincidence between electron and proton events must be considered. If the electron and proton coincidence events were perfectly paired, trigger efficiency of T1 also equals the product of T3 and T4 efficiencies. Though in real experiment, we can see the difference

Table 3.1: Trigger system designed for E12-14-012 experiment.

T1	(S_0&&S_2) AND (GC||PR) [LEFT]
	AND (S0&&S2) [RIGHT]
T2	(S_0||S_2) AND (GC||PR) [LEFT]
	AND (S_0||S_2) AND NOT(PS) [RIGHT]
T3	(S_0&&S_2) AND (GC||PR) [LEFT]
T4	(S_0&&S_2) [RIGHT]
T5	(S_0||S_2) AND (GC||PR) [LEFT]
T6	(S_0||S_2) AND NOT(PS) [RIGHT]

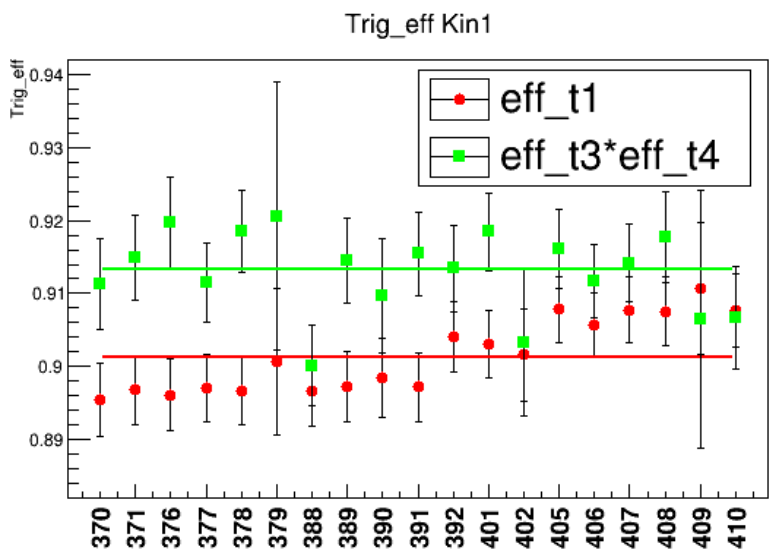

Figure 3.1: Trigger efficiency of T1 using two calculation methods for different runs in Kinematic 1. Red dots calculated from T1/T2 directly. Green dots represents the product of T3 and T4 efficiencies.

between these two calculations methods as shown in Fig 3.1.

In general, the measured efficiency varies between different kinematics. That's due to the several modifications of trigger settings during the data taking. Kinematic 1 had lowest trigger efficiency about 92%, while the trigger efficiency was about 98% for kinematic 5.

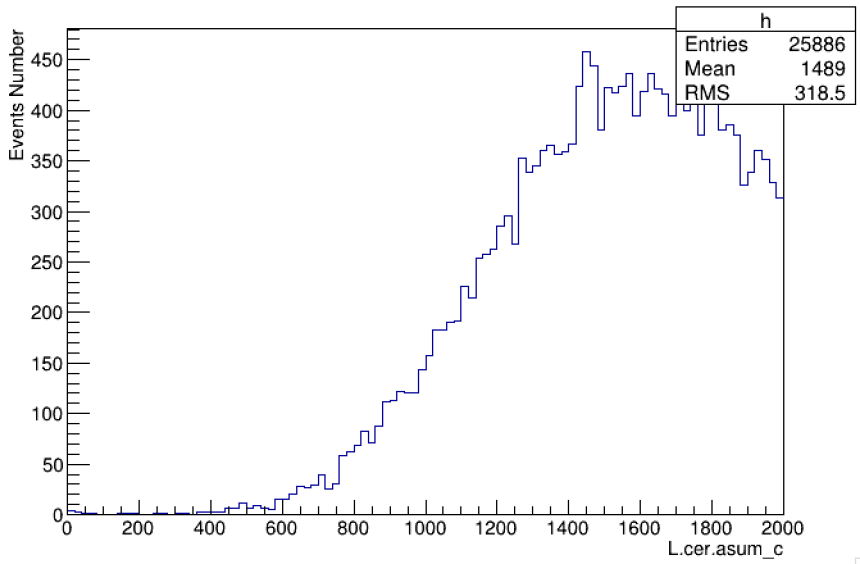

Figure 3.2: The distribution of the total ADC counts for all channels in gas Čerenkov detector.

3.2.3 Particle Identification Efficiency

In order to make sure to get clean electron and proton events, particle identification (PID) cuts should be applied. Since we used two spectrometers, PID cuts and efficiencies were considered for both arms.

For the left electron arm, gas Čerenkov and calorimeter were used for the electron selection.

The gas Čerenkov detector is described in Sec. 2.5.3. Figure 3.2 shows the distribution of the sum of the gas Čerenkov ADC counts for all channels. Electrons could be separated from π^- by requiring that the sum of the ADC counts (proportional to energy deposited) ($L.cer.asum_c$) is greater than 400 ADC counts.

The efficiency of the gas Čerenkov is computed isolating a very pure sample of electron events using other detectors in the HRS and then looking at ratio of events with $L.cer.asum_c > 400$ with respect to the total events in the controlled sample. The gas Čerenkov efficiency is defined as

$$\varepsilon_{GC} = \frac{N_{good}}{N_{tot}} \tag{3.6}$$

where N_{good} is the number of good events after we apply the ADC cuts on gas Čerenkov. N_{tot} is the total events before the cut. Gas Čerenkov efficiency was found varying from 97.5% for the lowest scattered electron beam energy runs to 99.9% for the highest E' runs.

Similarly, the calorimeter cut was applied to ensure only pure electrons left. The calorimeter cut efficiency was near 100% for all runs.

Apart from pure electron selection, to obtain a clean proton sample, we have also applied a selection cut using the proton arm spectrometer, in particular we selected events with a certain β value. Figure 3.3 shows the distribution of the β value for events in the right HRS. Events with a $\beta = 0.7$ corresponds to proton interacting in the spectrometer. Counting the good events number inside a region centered around β=0.7 and taking the ratio with respect to the the total events gives us the efficiency of the β cut. The efficiency of the β cut is $\sim$95% with a fluctuation of about 2% between the different kinematics.

3.2.4 VDC Tracking Efficiency

The VDC tracking efficiency is evaluated using two samples: the events with non-zero reconstructed tracks and the one with just one-track. We measure the probability that a charged particle is observed by the VDCs and accurately reconstructed.

We calculated the non-zero tracking reconstruction efficiency as follows:

- Without using any information from the VDCs, the data-set of electron (proton) events were defined as initial data input. Several cuts are applied to define this sample:

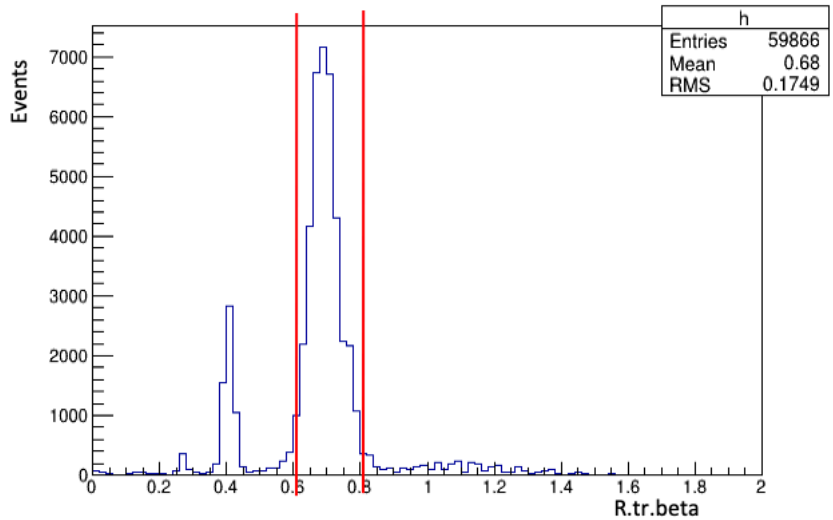

Figure 3.3: Distribution of event's β values. The region indicated by the two red lines is the region of interest (corresponding to proton events).

1. require a T1 trigger type;
2. apply the PID cuts using the gas Čerenkov and calorimeter in order to select a pure electron(proton) samples in the HRSs.

- The events number after these cuts defines the total number of event (N_{tot}), the non-zero tracking efficiency for the left(right) arm are defined as

$$\varepsilon_{Non-zero-tracking} = \frac{N_{good}}{N_{tot}} \tag{3.7}$$

where N_{good} is the number of events after adding non-zero cut on VDC ($L.tr.n > 0$ or $R.tr.n > 0$).

To find the one-track tracking sample efficiency, the procedures to find the N_{tot} is similar to non-zero tracking calculation, but we also considered the left(right) arm acceptance cuts. The acceptance cuts are the convolution of the θ, the ϕ, and the dp/p cuts to remove the events which are reconstructed outside the spectrometer acceptance volume. When

calculating N_{good}, single trajectory cut on VDC ($L.tr.n == 1$ or $R.tr.n == 1$) was used on the remaining events.

The total tracking efficiency for left (right) arm is the product of non-zero tracking and one-track tracking efficiencies. This efficiency is around 99%.

3.2.5 Vertex Z Correction

The argon target is 0.25 m long along the beam direction (defined as z in our coordinate reference system). The target volume is centered at z=0 and spans from z=-0.125 m to z=0.125 m. Since the Argon target is made of Aluminum, it is necessary to pay attention to the electron interactions that happen in the Aluminum and not in the Argon. We will consider those as background events from the end caps and the target cell's wall. Events that came from the beam entry and exit windows will need to be estimated and then subtracted from our data sample. We need to define a smaller volume of the target, and require that the reconstructed event vertex to be in such range. To define such volume we look at events from the dummy Aluminum target, the dummy target has the thickness much greater than the Aluminum gas cell but they are positioned at the same z as the gas cell entry and exit windows. Figure 3.4 shows the vertex z distribution of the dummy (Aluminium) target. We selected a region between -0.1 m to 0.1 m to best avoiding the background region. We then looked at events collected with an empty cell to further estimate the background due to the entry and exit window. The z cut is wide enough to make sure that we have plenty of data to do our analysis. The efficiency of vertex z was not measured separately. It is included in the tracking efficiency calculation and it is folded in the acceptance cuts.

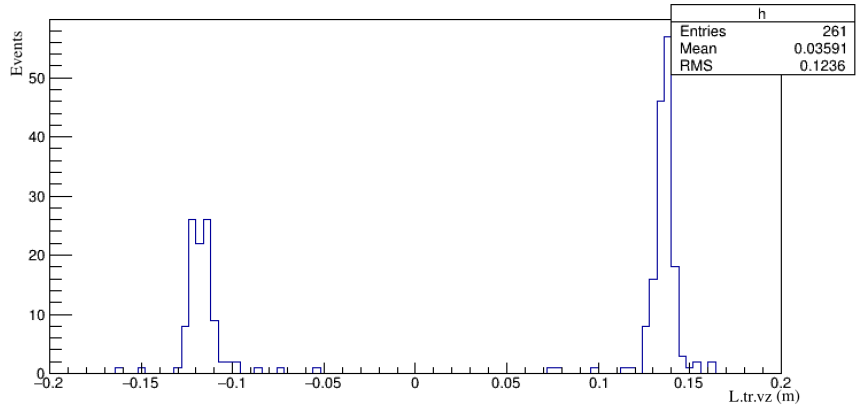

Figure 3.4: The distribution of reconstructed event vertex along the z direction for the Al dummy targets. The unit of x axis is meters

3.2.6 Coincidence Time Correction

The coincidence time is defined as the time difference between out-going electron passing through first scintillator plane S0 on the left spectrometer arm and knocked-out proton passing though S0 on the right arm. Considering the relativistic electrons and narrow range proton momentum, the coincidence time distribution should be expected as a sharp, well-defined peak. This distribution could be used to distinguish between true and accidental events.

True events are centered around the coincidence time distribution peak. They represents the out-going electron and knocked-out proton were coming from the same electron interacting event in the target.

Accidental event is another background source for our experiment. These events came from two uncorrelated events of each arm or also from (e,e$'\pi$) events. In general, these events are distributed uniformly in time and they will appear as a flat contribution in the coincidence time distribution. The number of accidentals depends on the target thickness and kinematical conditions. For kinematic 5 for example, its background is 70% of the selected sample,

considering kinematic 5 missing momentum is close to 300 MeV/c, the probability of pion production in final state is very high.

In order to get a high statistic sample for the background, we selected a broad region in the time coincidence distribution far away from the coincidence time window and we then determine the background events in the selected time coincidence window.

The time coincidence window is defined as a region at $\pm\,\sigma$ around the peak in the coincidence time event distribution. The peak corresponds to events in coincidence between the two spectrometers, see Fig. 3.5.

The coincidence time peak is not a delta peak but a distribution with finite width due to the following factors:

- Time fluctuation in the scintillators. The trigger time is determined by the timing the photomultiplier tubes (PMTs) receiving the signal on S0 plane. Thus, this time varies based on the location of the particle in the S0 plane. In general, this variation could be reduced by taking the average value of the two time-to-digit converters (TDCs).

- Fluctuation of proton's flight time due to different proton velocity. Because the knocked-out proton velocity could fluctuate, the time window will be broadened. This effect can be corrected through particle momentum reconstruction from the VDC information

$$\beta = \frac{p}{E} = \frac{p}{\sqrt{p^2 + m^2c^4}} \tag{3.8}$$

  where m is the mass of the particle in the experiment frame.

- Variation of electron's and proton's time of flight due to path differences. Ideally, if

the particle travels along the beam direction, the time of flight of the particle is

$$t_0 = \frac{l_0}{v_0} \tag{3.9}$$

where l_0 is the path length along the beam direction and v_0 is the nominal velocity of the particles. In general, particle travel path may vary a bit and the actual time of flight of a particle is

$$t = \frac{l}{v} = \frac{l_0 + \Delta l}{\beta \cdot c} \tag{3.10}$$

where v is the actual velocity of the particle calculated. Δl is the calculated path difference. The difference between the actual and ideal time of flight is

$$t - t_0 = l_0 \cdot \left(\frac{1}{v} - \frac{1}{v_0}\right) + \frac{\Delta l}{v} \tag{3.11}$$

Figure 3.5 shows the distribution of time difference between scattered electron passing through S0 and knocked-out proton passing through S0. The red peak curve is the coincidence time cut applied after the Gaussian fit. The range of the cut is $\pm\sigma$ around the peak center. The coincidence time efficiency is around 50% for all runs.

The accidental background is the flat distribution at the bottom of the peak. To select it we pick up a region distant from the time coincidence peak, and integrate the number of events in this region. We then re-scale the background events using the ratio between the width of the time coincidence peak and the width of the region used to select the background sample. Based on above we can have a very good background estimation with a very low statistical error for each of our kinematics.

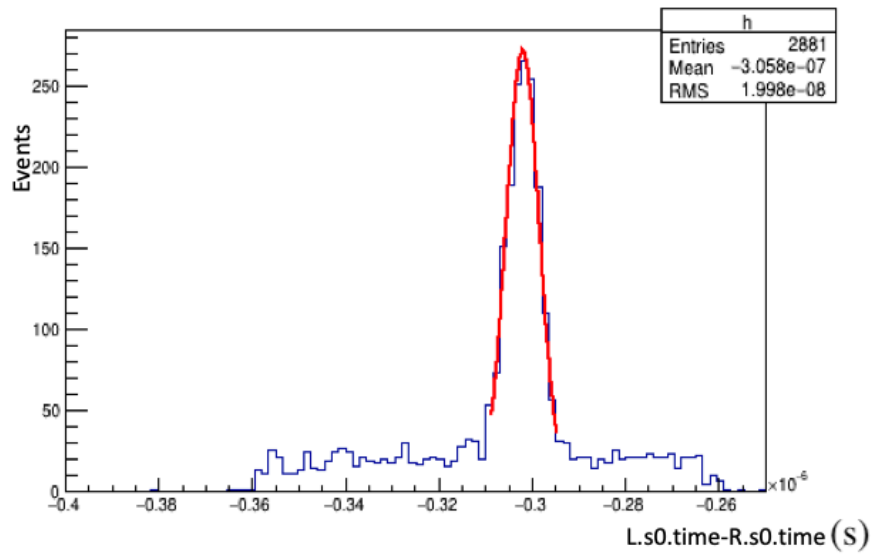

Figure 3.5: The coincidence time distribution for Ar $(e, e'p)$ reaction. The unit of the x axis is seconds.

3.3 Background Study

The experimental data combines both signal and background. It is necessary to perform background studies and remove as much as background events as possible. For JLab E12-14-012 experiment, background mainly comes from two ways: Target Wall and Accidental. Section. 3.3.1 and Section. 3.3.2 will explain how we quantify those backgrounds and how we have them subtracted from our data.

3.3.1 Background From Target Wall

Argon target cell is made of aluminium. Electrons in the beam could scatter not only with Argon nucleus, but also with Aluminium nucleus from the entry and exit windows. We set up the dummy target which is introduced in Section. 2.3. In general, dummy target is two aluminium blocks sitting at the same position as the entry and exit window of Argon

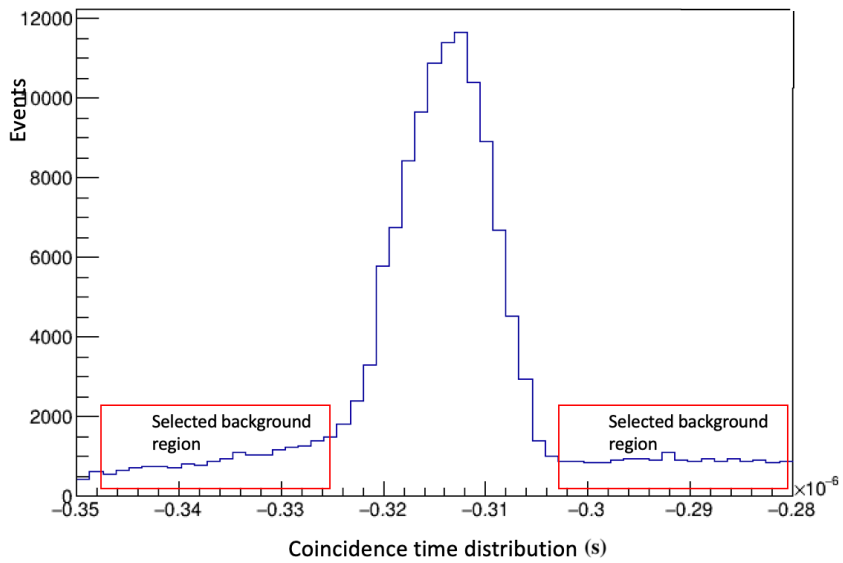

Figure 3.6: The coincidence time distribution for Ar $(e, e'p)$ reaction. The red box selects the background region to quantify the background ratio. The unit of x axis is seconds.

cell. Figure 3.4 shows an example for vertex z distribution of dummy target. Z cut range is defined as ±0.1 m. Events that falls inside the z cut, in the case of the dummy target sample, are bad events N_{bad}, the ratio N_{bad}/N_{total} measures the background rate coming from the target's windows. We will then need to correct that from the thickness of the dummy Aluminium target and the actual thickness of the gas target cell. This ratio is very very small (far below 1%).

3.3.2 Accidental Background

With higher missing momentum, the probability that (e,e′π) happens is higher. This is the accidental background source for our experiment. Figure 3.6 shows the coincidence time distribution for (e,e′p) reaction. The procedures to calculate the accidental background ratio is followed.

1. Identify the background region. Red boxes at two sides of the coincidence peak select the flat accidental background region. Count the total events number inside two regions as $N_{outside}$. The width of background selection range is $L_{outside}$.

2. Apply the Gaussian fit to the coincidence time peak. Measure the mean and standard deviation of the peak as T_{center} and σ, respectively.

3. Scale the sides background rate to the peak region. The scaled background events inside $\pm\sigma$ coincidence time peak region N_{inside} is

$$N_{inside} = \frac{2\sigma N_{outside}}{L_{outside}} \tag{3.12}$$

Table 3.2 lists accidental background ratio in five kinematics. Kinematic 1 has lowest background because of low missing momentum. While for kinematic 5, data is dominated by (e,e$'\pi$) reaction.

Table 3.2: Accidental Background to signal ratio in each kinematic and target.

	Ar	Ti
kin 1	3%	2%
kin 2	7%	8%
kin 3	13%	11%
kin 4	20%	20%
kin 5	70%	NA

3.4 List of Systematic Uncertainties

Systematic uncertainties come both from data itself and the Monte Carlo model used. We considered uncertainties for each of the 40 bins in missing momentum distributions. The missing momentum distributions are computed by integrating events in different ranges of missing energies.

3.4.1 Systematic Uncertainty from Cuts

The procedure used to compute systematic uncertainties from acceptance and selection cuts is followed.

1. Count the events number for data and Monte Carlo (MC). Number of events is measured for each bin after applying all the cuts as N_{data} and N_{MC}.

2. Compute the data to MC event ratio. The ratio r is

$$r = \frac{N_{data}}{N_{MC}} \tag{3.13}$$

3. Vary the cut using the experimental resolution, repeat step 1 and 2 to compute the new ratio r'. Here are the variations for different cuts.

   - Acceptance cuts were all varied by ± 0.0002 rad. This corresponds to the spectrometer angular resolution.
   - The z cut was varied by ± 0.008 m corresponding to the width of the peak in Fig. 3.7.
   - Particle identification cuts were varied by $\pm 5\%$.
   - Coincidence time cut was varied by $\pm 3^{-10}$ s, corresponding to the scintillator resolution.

4. The difference of the two ratios were considered as the systematic uncertainty from this cut for each bin in missing momentum.

$$sys_{error} = \frac{|r - r'|}{r} \tag{3.14}$$

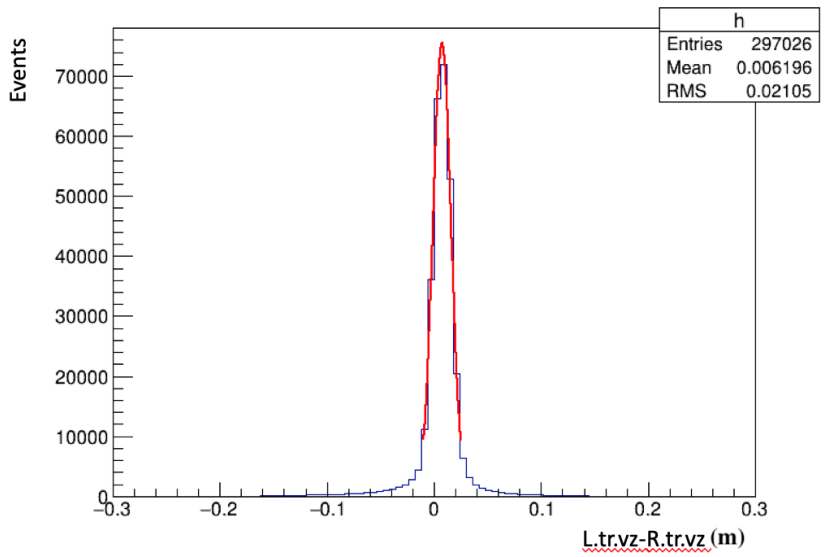

Figure 3.7: The vertex z distribution difference between left and right arm. Red curve is the Gaussian fit applied to the peak.

3.4.2 Systematic Uncertainty from the simulation

The MC model was used to simulate the whole experiment. The systematic uncertainties from the beam and spectrometer offsets were measured.

1. For the MC model, we count the events number of each bin in missing momentum distribution.

2. Re-generate the MC model after varying the offset or COSY matrix. COSY is the optical transport simulation package. It simulates the particle transport through the dipole and quadrupole magnet of the HRSs. We measure the number of events within all the cuts for each different MC settings.

   - The resolution of the beam position is ±0.004 m in the x direction and ±0.005 m in the y direction. Thus, beam offsets were varied using those settings.

   - The variation of the spectrometer x offset is ±0.0005 m, which is the same as of

the spectrometer y offset.

- The code COSY was used to generate the optical matrix for simulation. Measuring the systematic uncertainty from COSY would help estimate the optical matrix uncertainty due to the magnetic field settings of three quadrupoles (Q1, Q2 and Q3). The individual settings were varied by 1%, respectively.

3. The percentage difference of the events number between old and new MC model was considered as the systematic uncertainty from it.

3.4.3 Systematic Uncertainty from Radiative Corrections and the input MC Cross Section Model

Radiative processes includes a variety of effects like vertex corrections, vacuum polarization and external bremsstrahlung process. These effects should be correctly taken into account when generating events in the MC and can affect both the normalization and shape of the event distributions. To understand the effect on the shape of the event distributions, we re-scaled the MC input cross section by $\sqrt{(Q^2)}/2$, and then we recalculated the radiative corrections. We added a flat 1% systematic uncertainty due to the uncertainties in the theoretical models used to compute such corrections.

3.4.4 Systematic Uncertainty from Radiative corrections Dependence on Boiling Effect

When the high energy beam passing through the Argon target, Argon gas inside is heated and as a result the gas density changed inside the gas cell. The density change is proportional to the energy deposited by the beam on the target. We have computed the density variations

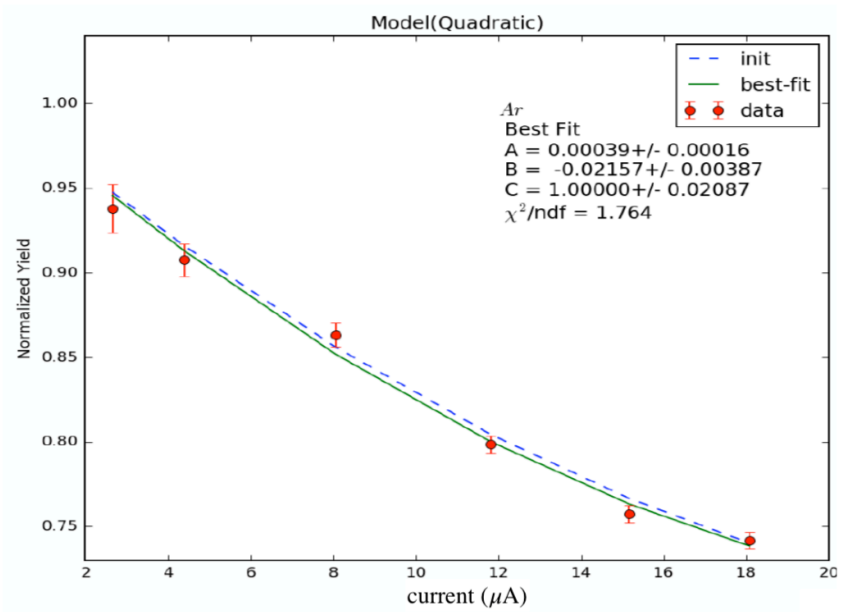

Figure 3.8: The distribution of the normalized yield versus different beam currents.

for different beam currents using:

$$Yield = \frac{PS \cdot N}{\epsilon \cdot LT \cdot charge} \tag{3.15}$$

where PS is the pre-scale factor, N is the total events counted. ϵ is the total efficiency correction applied. LT refers to live-time and $charge$ is the total electron charge measured.

The percentage change in yield represents density change in the gas cell. The yield normalization is done with respect to the lowest current. Figure 3.8 shows a fit with a quadratic function (green curve) and with the $I = 0$ point fixed to 1.

The average beam current of our 5 kinematics is 17 μA, with a $\pm 4\%$ variation. The corresponding boiling effect is 25%, with a 0.35% variation. After generating a cross section model with 25% boiling effect, the radiation correction was calculated at boiling effect at 24.65% and 25.35%. The variations were added to the overall systematic uncertainties.

3.4.5 Summary of the Systematic Uncertainties

An estimate of the systematic uncertainties for kinematic 1 is listed in Chapter. 5. The total uncertainty is around 5% for E12-14-012 experiment. The uncertainty is dominated by Acceptance cuts, MC and cross section model. The systematic uncertainties for the other four kinematics are still under working, but we should expect them to be finished before summer.

Chapter 4

Measurement of the cross sections for inclusive electron scattering in the E12-14-012 experiment at Jefferson Lab

The work described in this chapter was contributed by: Matt Murphy, Hongxia Dai, Linjie Gu, et al, (The Jefferson Lab Hall A Collaboration). It has been published on Physical Review C as:

Matt Murphy, Hongxia Dai, Linjie Gu, et al, (The Jefferson Lab Hall A Collaboration), "Measurement of the cross sections for inclusive electron scattering in the E12-14-012 experiment at Jefferson Lab" [27].

Reproduced with permission from the American Physical Society. Copyright (2019) by the American Physical Society.

I contributed part of the data analysis work in this paper under Prof. C. Mariani's supervision. I have been responsible for the detector efficiency calculations.

4.1 Introduction

Electron scattering experiments have been shown to be the best tool for precise investigations of the structure of atomic nuclei [28]. The electromagnetic interaction of electrons with the target is weak compared with the strength of interactions that bind nucleons together, and can be treated as an exchange of a single photon. Allowing the nuclear response to be probed at energy transfers varied independently from momentum transfers, electron beams can be used to investigate physics corresponding to various excitation energies with different spacial resolutions, exposing to different interaction mechanisms.

The existing body of electron-scattering data clearly shows that many important features of nuclear structure can be described assuming that nucleons forming the nucleus behave as independent particles bound in a mean field [29], but this picture is not complete without accounting for correlations between nucleons [30].

While analysis of electron scattering from nuclei is interesting in its own right, accurate description of nuclear effects in interactions of a few-GeV probes is now coming into sharp focus due to its relevance for neutrino physics. As neutrino oscillation parameters are extracted from collected event spectra, and neutrino energies have to be reconstructed from the observed kinematics of the products of their interactions with nuclear targets, nuclear effects play fundamental role in neutrino-oscillation analysis [31].

In neutrino experiments, nuclear models implemented in Monte Carlo (MC) simulations are employed to predict event rate in a near detector, perform its extrapolation to a far detector, estimate the energy carried by undetected particles, and obtain background estimates. While description of nuclear effects is already one of the largest sources of systematic uncertainties in ongoing oscillation studies [32], its importance will increase further in the next generation of oscillation experiments. In particular, to achieve their sensitivity goals, the

Deep Underground Neutrino Experiment (DUNE) and Hyper-Kamiokande have to reduce uncertainties coming from nuclear cross sections to a few-percent level [33, 34].

As weak interactions of neutrinos probe nucleus in a very similar way as electromagnetic interactions of electrons, precise electron scattering data give unique opportunity to validate nuclear models employed in neutrino physics. A theory model unable to reproduce electron measurements cannot be expected to provide accurate predictions for neutrino cross sections.

At the kinematics where the impulse approximation is valid—the process of scattering off a nuclear target can be described as involving predominantly a single nucleon, with $(A-1)$ nucleons acting as a spectator system—nuclear effects can be separated from the description of the elementary cross sections, differing between neutrinos and electrons, and the knowledge gained in electron scattering directly translates to neutrino interactions. In particular, measurements of the $(e, e'p)$ cross sections—in which knocked out protons are detected in coincidence with electrons—can be used to extract the information on the momentum and energy distributions (the spectral function) of protons in the nucleus, and on final-state interactions (FSI) of the struck protons propagating through the (excited) residual nucleus, which are intrinsic properties of the target and do not depend on the interaction mechanism.

In the simplest case of a symmetric nuclear target, with the proton number Z equal to the neutron number N, nuclear effects are expected to be largely the same in neutrino and electron interactions, up to small Coulomb corrections. For an asymmetric nucleus, one needs to additionally analyze electron scattering on its mirror nucleus, with Z and N swapped, to obtain a good approximation of information on the neutron structure, impossible to collect directly. In the case of DUNE, in addition to argon $(Z = 18, N = 22)$—employed as the target material—it is necessary to collect electron scattering data also for titanium $(Z = 22)$. While the exclusive $(e, e'p)$ cross sections give direct insight into the nuclear structure, they do not provide a complete picture of all interaction dynamics.

When the energy transferred by the interacting electron to the nucleon increases, the interaction mechanism changes from quasielastic (QE) scattering, in which the struck nucleon is removed from the nucleus, to nucleon resonance production, dominated by the excitation of the Δ resonance, and finally to deep-inelastic scattering on individual quarks forming nucleons. The inclusive (e, e') measurements, which yield the spectra of electrons scattered at fixed angle, provide information on all interaction mechanisms, regardless of the composition of hadrons in the final state. As a consequence, a great deal can be learned from the inclusive (e, e') cross sections, particularly in the context of DUNE, in which $\sim$2/3 of events are expected to involve pions [33].

The features of the peaks observed in the inclusive spectrum—their width, position, shape, and height—provide information on the momentum and energy distributions of the nucleons in the nuclear ground state, as well as on the final-state interactions (FSI) between the struck-nucleons and the spectator system. The width of the QE peak, which in the nonrelativistic regime depends on both the momentum carried by the struck nucleon and the momentum transfer, $\mathbf{q}$, in the relativistic regime becomes largely independent of $\mathbf{q}$, and can be simply parametrized in terms of a Fermi momentum, k_F [35]. However, a kinematic-dependent broadening ascribed to FSI is also observed. The position of the QE peak is determined by the combined effects of nuclear binding and FSI, while its pronounced asymmetry is a consequence of multi-nucleon knockout processes, induced by short-range correlations between nucleons in the initial state and by two-body interaction mechanisms, such as those involving meson-exchange currents. The height of the QE peak depends on the number of nucleons probed by the interaction and the momentum and energy distributions of nucleons in the ground state.

The identification of nuclear effects shaping the peak corresponding to QE scattering largely applies to other interaction mechanisms as well. However, their contributions give rise to

broader structures in the cross section, as they involve production of hadrons of finite lifetimes.

To provide a reliable foundation for the oscillation analysis of precise long-baseline neutrino experiment, a nuclear model employed in Monte Carlo simulations must be able to reproduce the features of the cross sections for electron scattering corresponding to the kinematics and target of relevance. In the context of DUNE, beam energies between 2 and 4 GeV play the most important role, and argon is the target material.

Previously [36, 37], we have reported the inclusive cross sections for electron scattering off argon, titanium, and carbon, extracted for beam energy 2.222 GeV and scattering angle 15.54°. Here we present a new result for aluminum, and a complete scaling analysis of all the targets that we have analyzed. We also discuss in more details the procedures used to measure the inclusive cross sections, together with their uncertainty estimates. In Sec. 5.2 we describe the setup of the performed experiment. The methods of extracting the cross sections are presented in Sec. 4.3. The estimates of their uncertainties are covered in Sec. 5.4. In Sec. 4.5 we report and discuss the measured aluminum cross section, while Sec. 4.6 is devoted to the scaling analysis of our data. Finally, in Sec. 5.6 we summarize our findings and draw the conclusions.

4.2 Experimental Setup

Performed at Jefferson Lab, E12-14-012 took both exclusive electron scattering data $(e, e'p)$ in which the proton knocked out from the nuclear target is detected in coincidence with the scattered electron, and inclusive (e, e') data in which all final states contribute, for different targets: C, Ti, Ar and Al. The experiment E12-14-012 used an electron beam of energy 2.222 GeV provided by the Continuous Electron Beam Accelerator Facility (CEBAF),

and took data in Spring 2017. The average beam current was 10 μA. Scattered electrons were measured using a high resolution spectrometer (HRS), equipped with two vertical drift chambers (VDCs) providing tracking information [24], two scintillator planes for timing measurements and triggering, double-layered lead-glass calorimeter, and a gas Čerenkov counter used for particle identification [19]. The HRS was positioned with a central scattering angle of $\theta = 15.54°$. The data analysis for inclusive electron scattering is relatively simple, as it implies modest data acquisition (DAQ) rates and very small pion backgrounds. The beam current and position, the latter being critical for the electron-vertex reconstruction and momentum calculation, were monitored by resonant radio-frequency cavities (beam current monitors, or BCMs [19]) and cavities with four antennae (beam position monitors, or BPMs [19]), respectively. The beam size was measured using harp scanners, which moved a thin wire through the beam. The beam was spread over a 2×2 mm^2 area to avoid overheating the target.

The experiment employed a set of solid targets—aluminum, carbon (single foil and a multi-foil composed of 9 foils), and titanium—as well as a closed cell of gaseous argon [23]. The aluminum target consisted of two identical foils of the 7075 alloy, the thickness of which was 0.889 ± 0.002 g/cm^2. Details of the elementary composition of the Al-7075 alloy used in the E12-14-012 experiment are given in Table 4.1. The aluminum foils were positioned to match the entrance and exit windows of the argon target, separated by a distance of 25 cm. Their thickness was fixed to be the same as the radiation length of the argon target. The analysis presented here uses the data from one of the foils only, located upstream of the spectrometers at $z = -12.5$ cm. The data were taken in nine separate runs, modifying at each step the momentum of the spectrometer in order to cover the final electron energy E' from 1.285 to 2.135 GeV.

The VDCs' tracking information allowed the determination of the momentum and recon-

Table 4.1: Composition of the Al-7075 alloy. For each element, we provide the number of protons Z and the average number of neutrons N calculated according to the isotopic abundances [38].

	weight (%)	Z	N
Al	89.72	13	14.00
Zn	5.8	30	35.45
Mg	2.4	12	12.32
Cu	1.5	29	34.62
Fe	0.19	26	29.91
Cr	0.19	24	28.06
Si	0.07	14	14.11
Mn	0.03	25	30.00
Ti	0.03	22	25.92
V	0.01	23	28.00
Zr	0.01	40	51.32
other	0.05		
average		14.26 ± 0.01	15.58 ± 0.01

struction of the direction (in-plane and out-of-plane angles) of the scattered electron, and reconstructing the interaction vertex at the target. The transformation between focal plane and target quantities was computed using an optical matrix, the accuracy of which was verified using the multi-foil target data. Possible variations of the magnetic field in the HRS magnets that could affect the optics are included in the analysis as systematic uncertainties.

We set up two types of hardware triggers:

$$T_3 = (S_0 \&\& S_2) \&\& (LC || GC),$$

$$T_5 = (S_0 || S_2) \&\& (LC || GC).$$

The T_3 (T_5) trigger type requires that the signal from the scintillator plane S_0 AND S_2 (S_0 OR S_2) is detected in coincidence with the signal from the lead calorimeter (LC) OR the gas Čerenkov counter (GC).

Electrons were selected in the HRS requiring, in addition, one reconstructed track. Further, they had to deposit 30% of their energy in the lead calorimeter ($E_{\rm cal}/p > 0.3$). To select events in the central acceptance region of the spectrometer, the electron's track was required to be within ± 4 mrad of the in-plane angle and ± 6 mrad of the out-of-plane angle with respect to the center ray of the spectrometer and have a dp/p of ± 0.04. The spectrometers were calibrated using sieve slit measurements and the position of the spectrometers and angles were surveyed before the start of the data taking. The survey precision for the angle and position measurements is respectively 0.01 mrad and 0.01 mm.

The efficiencies of the elements in the detector stack were studied by comparing rates in various combinations of secondary triggers. The scintillator efficiency, ($S_0 \& \& S_2$), was studied using the ratio of the events rates selected using T_3 and T_5 trigger types, requiring one reconstructed track, and applying the acceptance and calorimeter cuts. It was found to be 99%. The efficiency of the calorimeters was close to 100% for all runs, the efficiency of the Čerenkov detector was found to range from 99.9% for the highest E' runs down to 97.5% for the lowest E' run. The Čerenkov efficiency was evaluated by selecting a pure sample of electrons in the calorimeter and varying the Čerenkov cut by $\pm 10\%$. The live-time of the electronics, computed using the rates from scalers, which were independent of triggered events, was above 98% for all runs. The acceptance cuts efficiencies ($\sim$98%) and the dp cut efficiency ($\sim$99%) were computed using the MC simulation [39]. The overall efficiency (between 88 and 95% across all the kinematical regions) includes cuts on the calorimeters, both the lead and the Čerenkov counter, track reconstruction efficiency, livetime and acceptance.

4.3 Data Analysis

4.3.1 Yield-Ratio Method

The yield-ratio method of determining the cross section involves both the experimental data and simulated MC data. In this method, the yield Y is calculated for both sets of data as

$$Y^i = (N_S^i \times PS)/(LT \times \epsilon), \tag{4.1}$$

where i refers to the ith bin of the E' distribution, N_S^i is the total number of scattered electrons, PS is a pre-scale factor in the DAQ, ϵ is the total efficiency of the detector, and LT is the livetime of the electronics. The ratio of the yields for the actual and MC data is taken as a means of eliminating any impact of the acceptance on each bin, and then the measured cross section is determined by multiplying this ratio by the cross section calculated within the Monte Carlo model:

$$\frac{d^2\sigma_{\text{data}}}{d\Omega dE'} = \frac{d^2\sigma_{\text{MC}}}{d\Omega dE'} \times \frac{Y_{\text{data}}}{Y_{\text{MC}}}. \tag{4.2}$$

4.3.2 Acceptance Method

The cross section was also extracted via another method, the acceptance method, and both the yield ratio and acceptance methods were examined for agreement. In the case of the argon target, for which an accurate model of the nuclear response is not yet available, it is important to validate the MC simulation and results obtained using the yield ratio method using an alternative method less dependent on the input MC cross section model. The acceptance method will be described in the following of this section.

For each $(\Delta E, \Delta\Omega)$ bin, the number of detected electrons can be determined using

$$N_S^i = L \times \frac{d^2\sigma}{d\Omega dE'} \times \Delta E' \Delta\Omega \times \epsilon \times A^i(E', \theta, \phi) \tag{4.3}$$

where L is the integrated luminosity (number of beam electrons $\times$ number of targets / area), ϵ is the total detection efficiency, and θ and ϕ represent the in-plane and out-of-plane angles, respectively. The acceptance $A^i(E', \theta, \phi)$ is the probability that a particle passes through the spectrometer into the ith bin.

The electron yield corrected for the overall efficiency (product of individual efficiencies as described above) can be cast as

$$\begin{aligned} Y^i &= \frac{N_S^i}{\epsilon} \\ &= L \times \frac{d^2\sigma_{\text{data}}}{d\Omega dE'} \times \Delta E' \Delta\Omega \times A^i(E', \theta, \phi), \end{aligned} \tag{4.4}$$

and the cross section can be measured using

$$\frac{d^2\sigma_{\text{data}}}{d\Omega dE'} = \frac{Y^i}{\Delta E' \Delta\Omega \times A^i(E', \theta, \phi) \times L}. \tag{4.5}$$

The single-arm Monte Carlo simulation was used to generate events uniformly distributed in (θ, ϕ, E'). For a specific phase-space slice in $(\Delta\theta, \Delta\phi, \Delta E')$, we computed the ratio between the total number of events that reach the spectrometer and the number of generated events. The ratio of these two numbers represents the probability that a particle successfully passes through the magnets and the aperture to arrive at the detector package.

For an extended target, an acceptance matrix $A^i(E', \theta, \phi)$ was generated at various points along the target length. Each different target slice was associated with a different $A^i(E', \theta, \phi)$.

The number and size of the slices were optimized based on the statistics of the data. In

principle, an infinite number of matrices could be used in order to make events perfectly weighted, but this method would be inefficient and subject to large statistical fluctuations, if the number of events in each region was limited.

In this analysis, we used a single matrix for events along the entire target length to correct the data, and evaluated the residual variation along the beam direction z. For these studies we took advantage of the optical target data, collected in Spring 2017.

The optical target was a series of nine carbon foils, placed along the beam direction at $z = 0$ cm, ± 2 cm, ± 5 cm, ± 7.5 cm, ± 10 cm, respectively. The z distribution of the events reconstructed from the optical target is shown in Fig. 4.1, with the shaded regions representing the z-position cuts employed to identify the events coming from individual carbon foils. Because it would be difficult to select pure events from each foil, due to its finite thickness, we used the Monte Carlo simulation and the carbon cross-section model to generate single-foil carbon data for different z positions of the target.

Using the single-foil carbon data, we generated 9 acceptance matrices corresponding to the mean z position of each foil composing the multi-foil carbon target. We applied a weight of $1/A(E', \theta, \phi)$ to every event, and made a comparison between the events originating from individual foils. The obtained distribution of MC event yields from different foils, normalized to the one from the foil at $z = 0$ cm, is shown in Fig. 4.2. The results for the 9 regions, represented by the red dots lying inside the green shaded band, are in excellent agreement, with variations between them remaining below 0.5%.

When the same procedure is applied to the reconstructed data events, the obtained event yields—represented by the blue lozenges in Fig. 4.2—exhibit a dependence on the target z position. This behavior is expected due to the variation of the cross section as a function of the electron scattering angle, as foils at different positions have different acceptances,

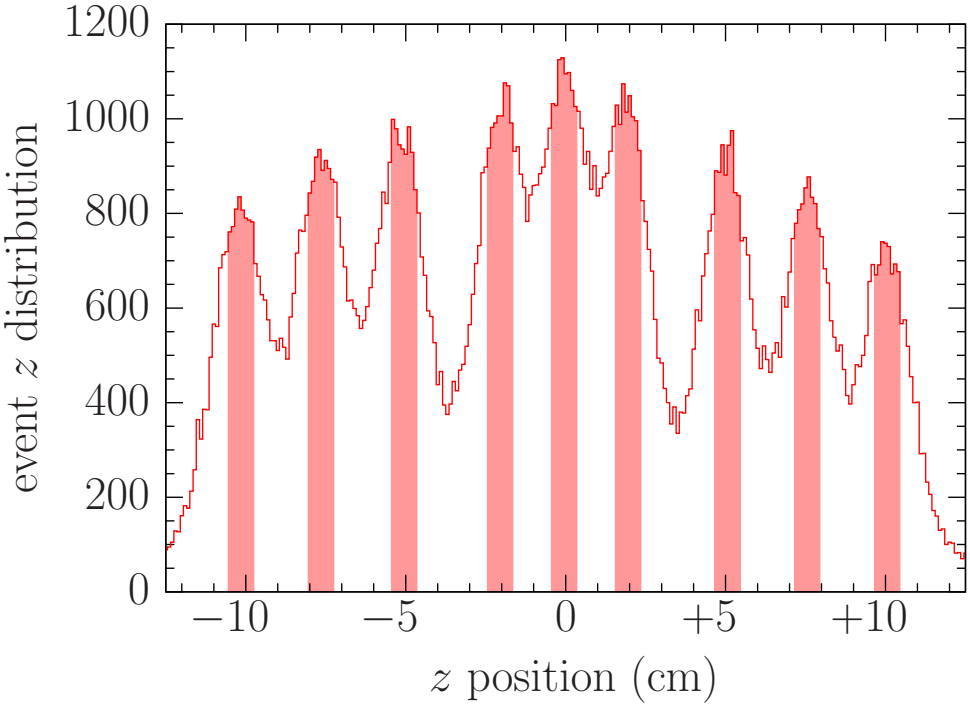

Figure 4.1: (color online). Distribution along the beam direction of reconstructed events for the multi-foil carbon target. The shaded regions represent the data selected to identify the events coming from individual carbon foils.

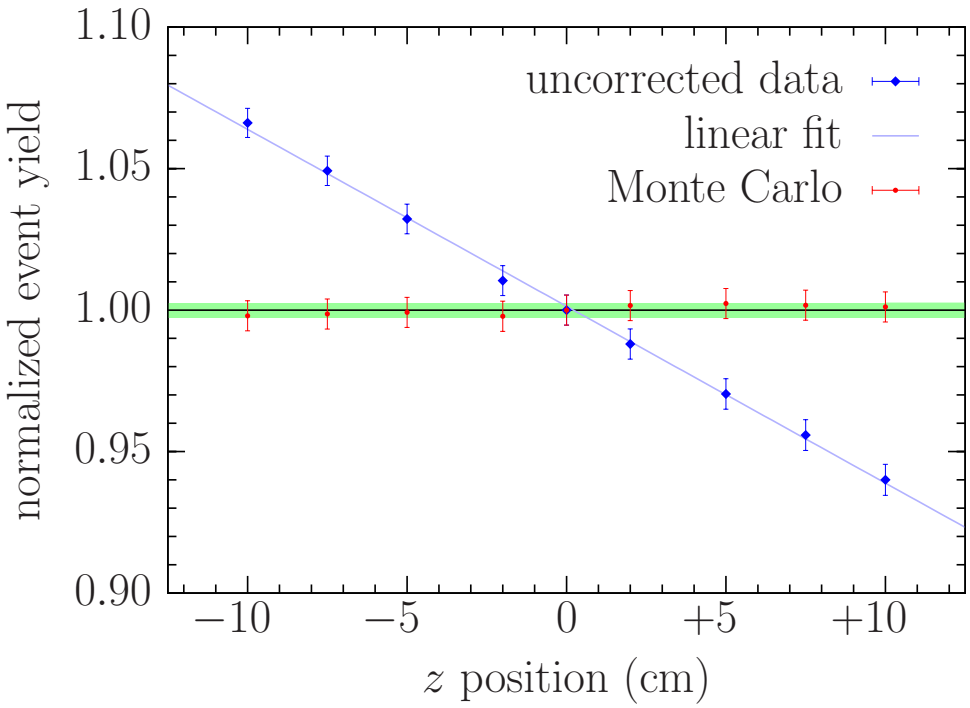

Figure 4.2: (color online). Event yields from carbon foils at different positions along the beam direction, normalized to the yield for the central foil, for the uncorrected data and the Monte Carlo simulation. The dependence of the cross section on the scattering angle, correctly taken into account in the Monte Carlo simulation, introduces a linear trend in the data that needs to be corrected for. All uncertainties are purely statistical.

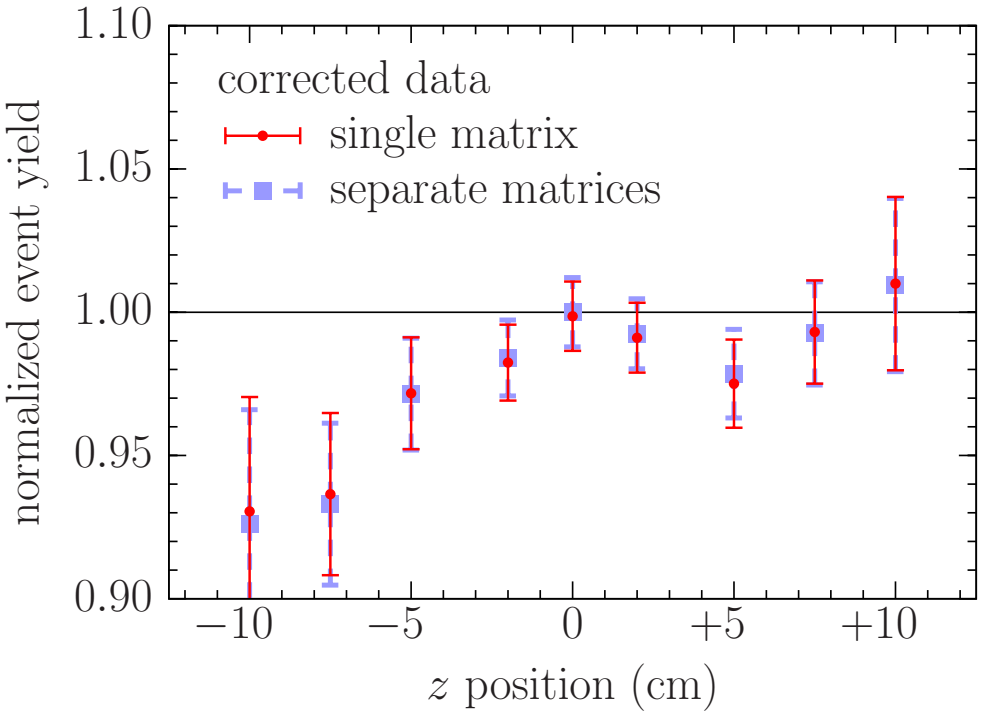

Figure 4.3: (color online). Event yields in the corrected data for the multi-foil carbon target surviving the z-position selection, normalized to the yield for the central foil. The outcomes of two correction procedures are compared. The error bars are symmetric and represent the total uncertainties, being the statistical and systematic uncertainties added in quadrature.

depending on the mean value of the scattering angle. The observed z dependence of the event yields is in a good agreement with a linear function ($\chi^2/\text{NDF} = 0.35$) and a correction is applied to the data. Note that this behavior is absent in the MC event yields (the red dots in Fig. 4.2), because the MC simulation takes into account differences in the acceptance for individual foils. In the data analysis, we relied on the reconstructed target z position to identify events coming from each of the 9 carbon foils, applying the selections represented by the shaded regions in Fig. 4.1. The selected events were then corrected using the acceptance matrix computed at $z = 0$ cm. In order to determine the sensitivity to this approximation, we repeated the same study using 9 different matrices (one for each carbon foil) and found a negligible variation, as shown in Fig 4.3. The obtained event yields are subject to the systematic uncertainties due to the z-position selection applied to identify events coming from individual foils.

As a final remark, we note that to acquire the inclusive data, we varied the momentum settings of the left-arm spectrometer in the MC to determine its effect on the acceptance matrix, and found that it is negligible.

4.4 Uncertainty Analysis

The total systematic uncertainty in this analysis was estimated by adding in quadrature the contributions listed in Table 5.5. Each of the uncertainties was considered completely uncorrelated. We determined the cuts ensuring that there are no dependencies on kinematical variables and, therefore, all the uncertainties affects only the normalization of the extracted cross sections. The kinematical cuts used in the analysis were varied by $\pm 10\%$ or by the resolution of the variable under consideration.

As the obtained results depend on the Monte Carlo calculation, it is important to estimate

Table 4.2: Contributions to systematic uncertainties in the yield-ratio method for aluminum and argon.

	Al	Ar
a. Beam energy	0.1%	0.1%
b. Beam charge	0.3%	0.3%
c. Beam x offset	$< 1.0\%$	$< 0.8\%$
d. Beam y offset	$< 1.0\%$	$< 0.9\%$
e. HRS x offset	$< 0.8\%$	$< 1.0\%$
f. HRS y offset	$< 0.6\%$	$< 0.8\%$
g. Optics (q1, q2, q3)	$< 1.8\%$	$< 1.0\%$
h. Target thickness	0.2%	0.7%
i. Acceptance cut $(\theta, \phi, dp/p)$	$< 1.0\%$	$< 2.4\%$
(i) dp acceptance cut	$< 0.32\%$	-
(ii) θ acceptance cut	$< 0.32\%$	-
(iii) ϕ acceptance cut	$< 0.79\%$	-
(iv) z acceptance cut	$< 0.45\%$	-
j. Calorimeter cut	$< 0.02\%$	$< 0.02\%$
k. Čerenkov cut	$< 0.12\%$	$< 0.07\%$
l. Cross section model	$< 0.2\%$	$< 1.3\%$
m. Radiative and Coulomb corr.	1.0%–1.3%	1.0%–1.3%
Total systematic uncertainty	1.7%–2.7%	1.8%–3.0%

uncertainties resulting from its inputs. To determine the uncertainties related to the target position, we performed the simulation with the inputs for the beam's and spectrometer's x and y offsets varied within uncertainties, and we recomputed the optical transport matrix varying the three quadrupole magnetic fields, one at the time. Each of these runs was compared to the reference run, and the corresponding differences were summed in quadrature to give the total systematic uncertainty due to the Monte Carlo. That summed uncertainty value varied from 1.1 to 2.2%, based on the momentum setting for each of the run, and was the largest single source of systematic error.

The systematic uncertainty due to the cuts on the calorimeter and Čerenkov detector was calculated in a similar way, by varying the cut by a small amount and calculating the

difference with respect to the nominal cut. Given the already high efficiency of these cuts, this resulted in a very small contribution to the uncertainty. The uncertainty due to the acceptance cuts on the angles and on dp/p was calculated in the same way. We included a fixed uncertainty relative to the beam charge and beam energy as in previous work on C and Ti [36].

The measured cross section is also corrected for the effects from internal and external radiative processes. Internal radiative process are vacuum polarization, vertex corrections, and internal bremsstrahlung. External radiative processes refer to electrons losing energy while passing through material in the target. We applied the radiative correction following the recipe of Dasu [40], using the approach of Mo and Tsai [41], which is subject to theoretical uncertainties and depends on the cross-section model. We consider a fixed 1% uncertainty due to the theoretical model for the radiative corrections over the full kinematical range. To account for the cross-section model dependence—the same for both the yield-ratio and acceptance methods—we added an additional uncertainty (fully uncorrelated), estimated by computing the difference in the final double differential cross section when the cross section model is rescaled by $\sqrt{(Q^2)}/2$, Q^2 being the four-momentum transfer squared. Coulomb corrections were included in the local effective momentum approximation, following Ref. [42]. A 10% uncertainty associated with the Coulomb potential was included as systematic uncertainty.

Near the quasielastic peak, there is a non-negligible contribution of the elastic cross section to the inclusive cross section, through the radiative processes. To estimate the corresponding uncertainty, we increased the tail of the elastic contribution by 20%, recalculated the radiative correction, and used its difference with respect to the reference correction as an estimate of the corresponding systematic uncertainty. Finally, we included a target thickness uncertainty.

4.5 Experimental Results

The cross section for inclusive scattering of electrons on the Al-7075 target, extracted using the yield-ratio method and normalized per nucleus, is shown in Fig. 4.4. Its total uncertainties—represented by the outer bands—are obtained by adding in quadrature statistical and systematic uncertainties. As in the case of the previously reported results [36, 37], the aluminum measurement is very precise and limited by the systematic uncertainties.

As a cross check, we also extracted the Al cross section using the acceptance method. Figure 4.5 shows that the results obtained using the two methods are in good agreement. Note that in the acceptance method we did not estimate systematic uncertainties, the error bars

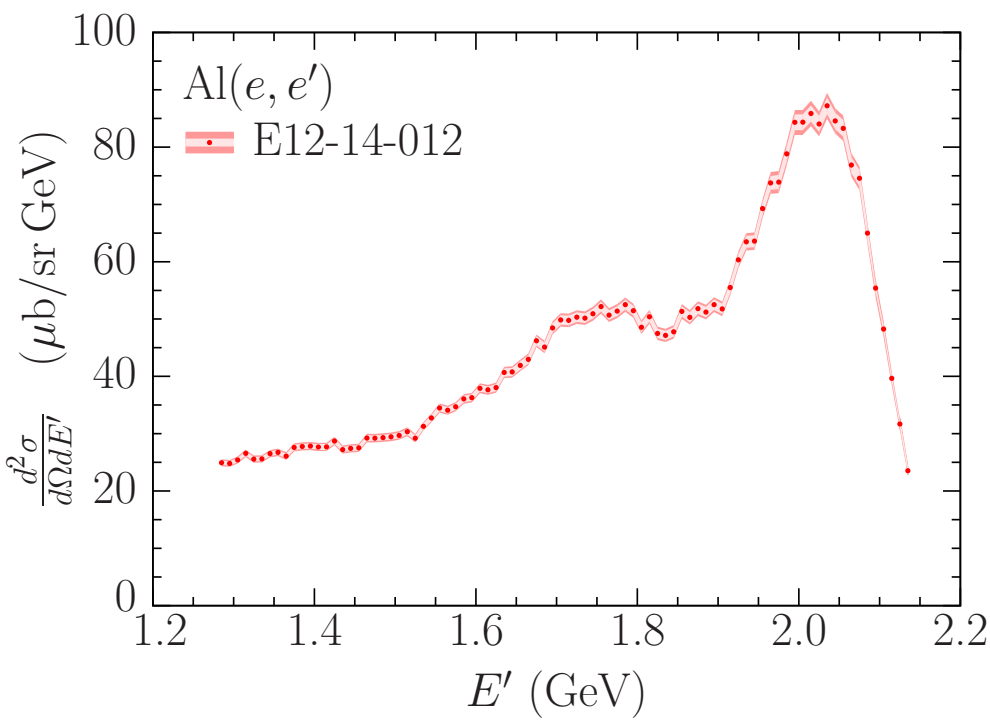

Figure 4.4: (color online). Double-differential cross section extracted for inclusive electron scattering off the Al-7075 target at beam energy 2.222 GeV and scattering angle 15.54°. The inner and outer uncertainty bands correspond to statistical and total uncertainties, respectively.

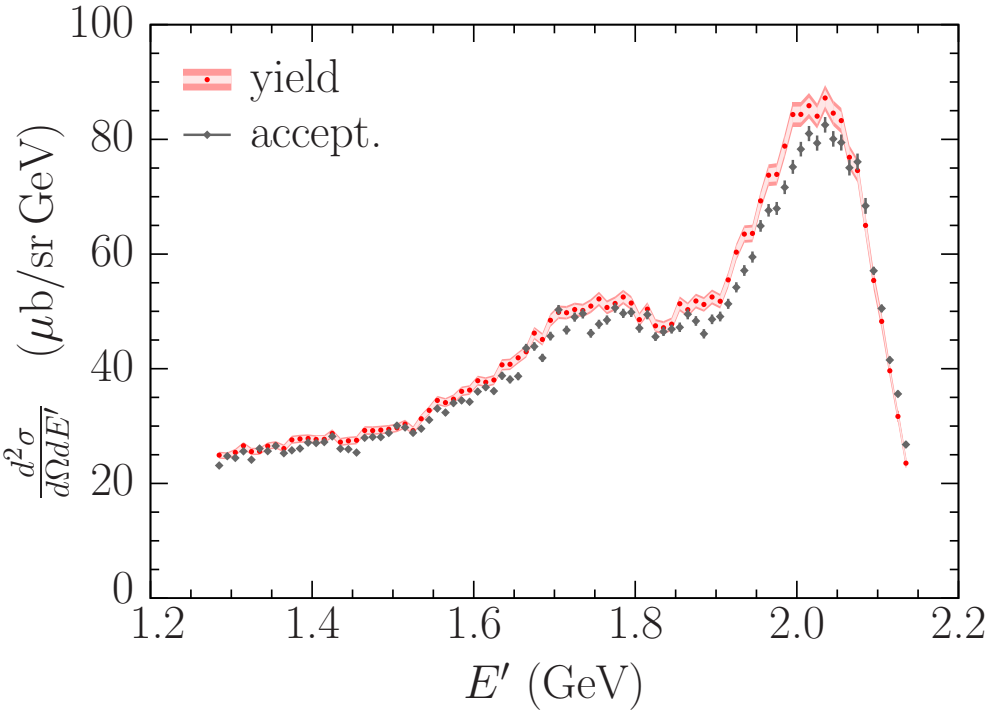

Figure 4.5: (color online). Comparison of the Al(e, e') cross sections extracted using the yield-ratio and acceptance methods. The inner (outer) bands for the yield-method show statistical (total) uncertainties. For the acceptance method only statistical uncertainties are shown.

represent the statistical uncertainties only.

The agreement between the yield-ratio and acceptance results was observed for the carbon, aluminum, titanium, and argon targets and provides validation for the approximation employed in the acceptance method, namely using a single acceptance matrix computed at $z = 0$ cm, as explained in Sec. 4.3.2. The consistency between the yield and acceptance methods for all analyzed targets also indicates that the yield-ratio result exhibits only weak dependence on the input cross section used in the Monte Carlo simulation to correct the data for efficiency and acceptance. This issue is particularly important in the case of the titanium and argon targets, where the cross-section simulations cannot be validated against existing data. Note that the radiative corrections applied in both methods are the same and do depend on the input cross section. The related uncertainties are discussed in Sec. 5.4.

To illustrate how nuclear effects affect different interaction channels, in Fig. 4.6 we compare the per-nucleon cross sections for aluminum, argon, titanium, and carbon. While for every target we account for the abundances of naturally occurring isotopes [38], this effect is relevant only for the Al target. It is a consequence of the non-negligible contributions of elements heavier than $^{27}_{13}$Al to the Al-7075 alloy, detailed in Table 4.1. At the considered kinematics, corresponding to the beam energy 2.222 GeV and scattering angle 15.54°, the cross sections per nucleon for targets ranging from carbon ($A = 12.01$) to titanium ($A = 47.92$) turn out to be in very good agreement in the region where different pion production mechanisms dominate. While this finding is by no means obvious—due to asymmetry of the proton and neutron numbers for aluminum, argon, and titanium—it is consistent with the results of Refs. [43, 44] at energies ∼0.54–1.50 GeV and scattering angles ∼37°.

The influence of nuclear effects on QE interactions can be better illustrated in terms of the cross sections normalized to the elementary contributions of neutrons and protons that

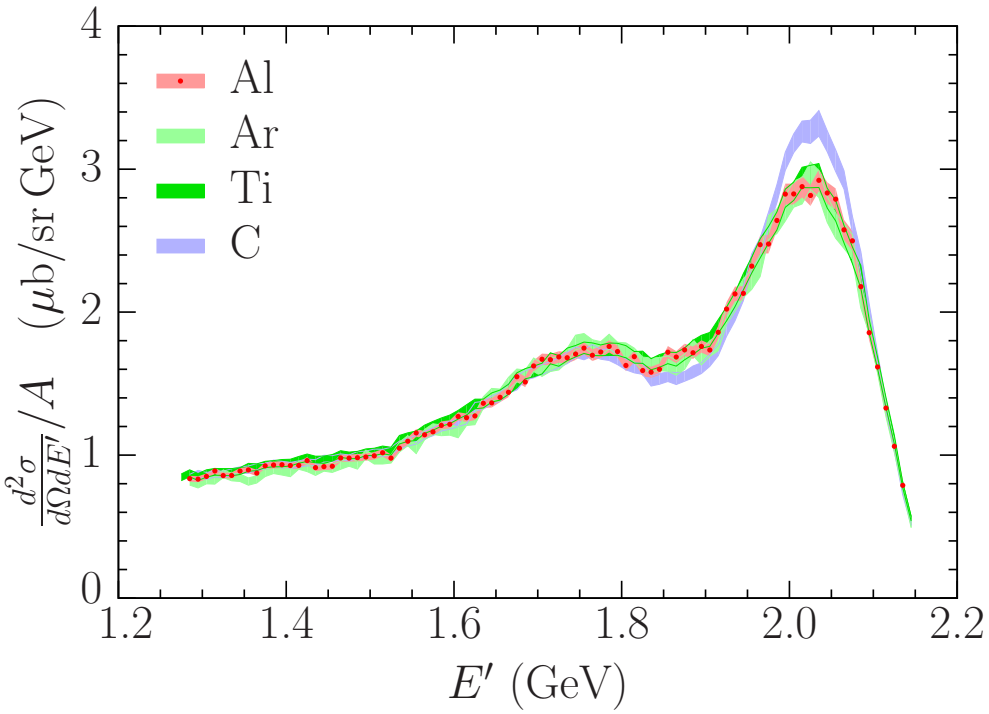

Figure 4.6: (color online). Comparison of the cross sections per nucleon for aluminum, argon [37], titanium [36], and carbon [36] measured at beam energy 2.222 GeV and scattering angle 15.54°. The average nucleon number for every target is calculated according to the natural abundances of isotopes, see details in the text. The bands represent the total uncertainties.

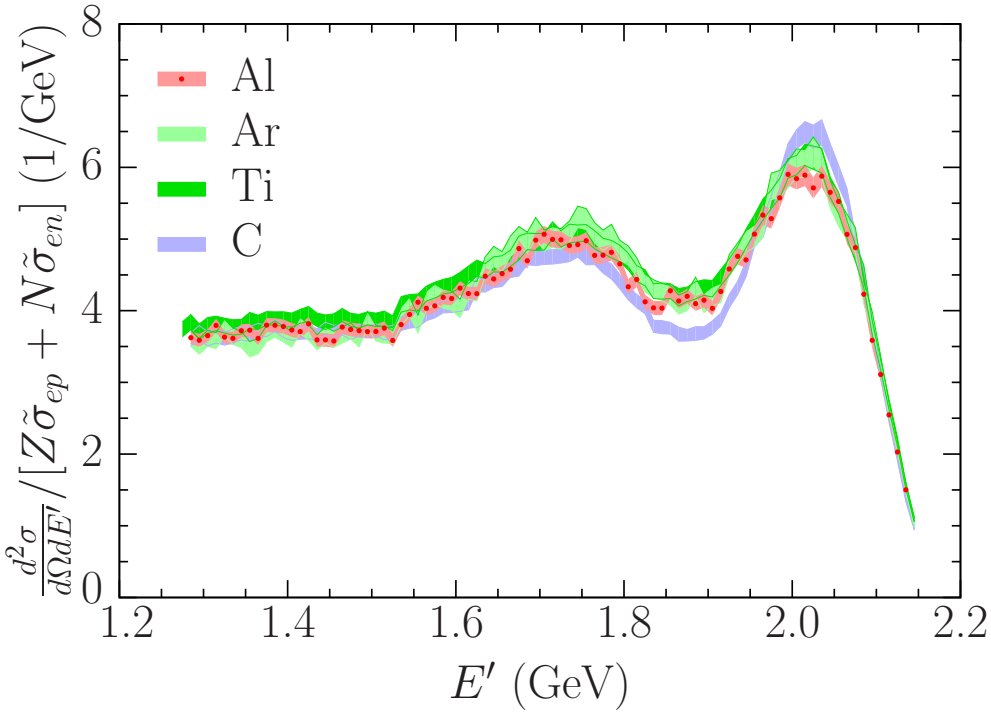

Figure 4.7: (color online). Same as in Fig. 4.6 but for the cross sections normalized by the combination of the elementary cross sections according to Eq. (4.6).

compose the nucleus, that is the quantity

$$\frac{d^2\sigma}{d\Omega dE'}/[Z\tilde{\sigma}_{ep} + N\tilde{\sigma}_{en}], \tag{4.6}$$

where Z and N are the proton and neutron numbers, respectively, while $\tilde{\sigma}_{ep}$ and $\tilde{\sigma}_{en}$ denote the elastic electron-proton and electron-neutron cross sections stripped of the energy-conserving delta function [16]. In the following, we use the average neutron numbers calculated according to the natural abundances of isotopes, that is 6.01 for carbon, 21.98 for argon, and 25.92 for titanium [38]. For the aluminum target, we employ $Z = 14.26$ and $N = 15.58$, due to its composition listed in Table 4.1.

As shown in Fig. 4.7, the results for titanium and argon are, within uncertainties, identical in the QE peak, but they differ from both those for carbon and aluminum. Near the maximum of the QE peak, the cross section defined in Eq. (4.6) is lower by ∼4% for aluminum, and higher by ∼5% for carbon, than the ones for argon and titanium. In the dip region, the results for aluminum (carbon) are lower by ∼2% (∼13%) compared with those for argon and titanium.

In QE scattering, the cross sections normalized according to Eq. (4.6) exhibit very weak target dependence only in the region of high E', corresponding to low energy transfers, as shown in Fig. 4.7. This is, however, not the case in the QE peak's maximum and for lower E', where the energy transferred by electrons to the nucleus is sufficiently high to probe deeply bound states and also to induce two-nucleon knockout.

The observed differences in the dependence on the atomic number of various interaction mechanisms—previously reported in Refs. [44, 45, 46]—can be expected to provide important clues for building models of nuclear effects valid over broad kinematic regimes and able to describe a range of targets. Such models are of great importance to long-baseline neutrino-

oscillation experiments.

4.6 Scaling and A-dependence

The scaling analysis allows to compare inclusive electron-scattering data taken in different kinematical conditions and using different targets.

Scaling of first kind, or y-scaling, is observed in the kinematical region of large momentum transfer, $|\mathbf{q}|$, and energy transfer $\omega < \sqrt{|\mathbf{q}|^2 + m^2} - m$, in which the beam particle interacts with individual nucleons and the dominant reaction mechanism is quasielastic scattering [47, 48]. Under these conditions, the target response, which in general depends on both momentum and energy transfers, reduces to a function of the single variable $y = y(|\mathbf{q}|, \omega)$, defined by the equation

$$\begin{aligned} \omega + M_A = &\sqrt{y^2 + (M_A - m + E_{\min})^2} \\ &+ \sqrt{(y + |\mathbf{q}|)^2 + m^2}. \end{aligned} \tag{4.7}$$

Here, m and M_A are the nucleon mass and the mass of the target nucleus, respectively, while $E_{\min}$ denotes the nucleon knockout threshold. The scaling variable y, having the dimension of energy, is simply related to the longitudinal component of the initial momentum of the struck nucleon, $k_{\parallel} = \mathbf{k} \cdot \mathbf{q}/|\mathbf{k}|$. The scaling function $F(y)$ is determined from the measured cross section, $\sigma^{\exp}$ through

$$F(y) = K \frac{\sigma^{\exp}}{Z\tilde{\sigma}_{ep} + N\tilde{\sigma}_{en}}, \tag{4.8}$$

with K a kinematic factor.

In Fig. 4.8, the y-scaling function of aluminum, computed using the cross section displayed in Fig. 4.4 and the average proton and neutron numbers from Table 4.1, is compared to those

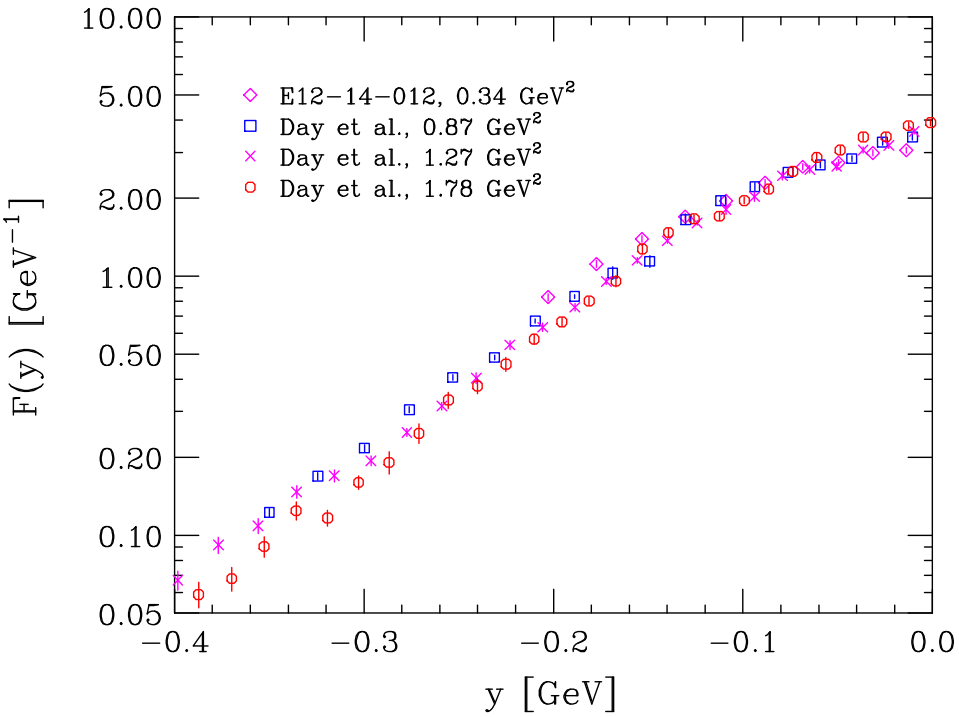

Figure 4.8: (color online) Comparison between the scaling function of aluminum obtained from the E12-14-012 data (this work), represented by diamonds, and those obtained from the data of Day *et al.* [49]. The data are labeled according to the value of Q^2 corresponding to quasi elastic kinematics.

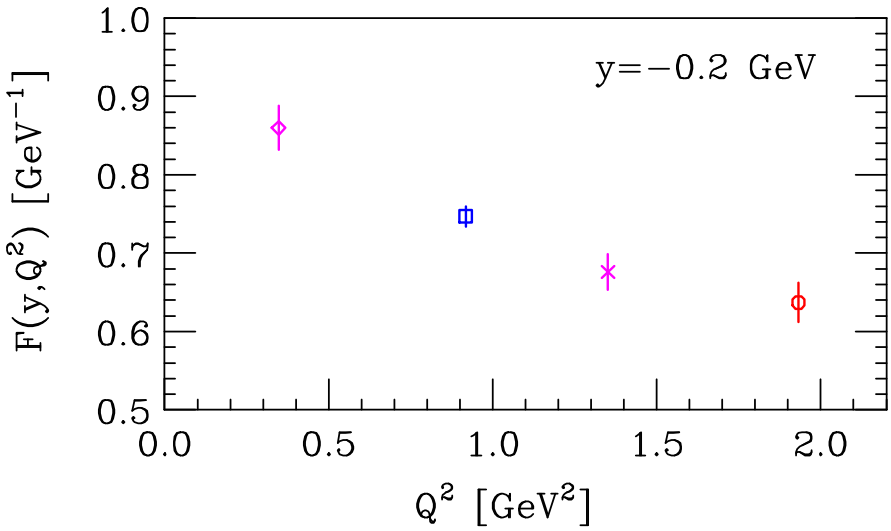

Figure 4.9: (color online) Q^2-dependence of the scaling functions $F(y, Q^2)$ obtained from the cross section displayed in Fig. 4.4 and from the data reported in Ref. [49]. The meaning of the symbols is the same as in Fig. 4.8.

obtained from the data of Day *et al* [49] using a $^{27}_{13}$Al target. The cross sections of Ref. [49] have been measured at fixed beam energy $E = 3.595$ GeV and scattering angle 16, 20 and 25 deg, with the values of Q^2 corresponding to quasi elastic kinematics being 0.87, 1.27 and 1.78 GeV^2, respectively.

Scaling behavior is clearly observed at $y \approx 0$, corresponding to region of the quasifree peak, or $\omega \approx Q^2/2m$. The sizeable scaling violations occurring at larger negative values of y are mainly to be ascribed to the effects of FSI between the knocked-out nucleon and the spectator particles. This feature is illustrated in Fig. 4.9, showing the Q^2-dependence of the scaling function $F(y, Q^2)$ at fixed $y = -0.2$ GeV. The approach to the scaling limit from above is a clear signature of FSI.

A more general form of scaling, dubbed scaling of second kind, permits a global analysis, combining data corresponding to different targets [50]. The definitions of the dimensionless

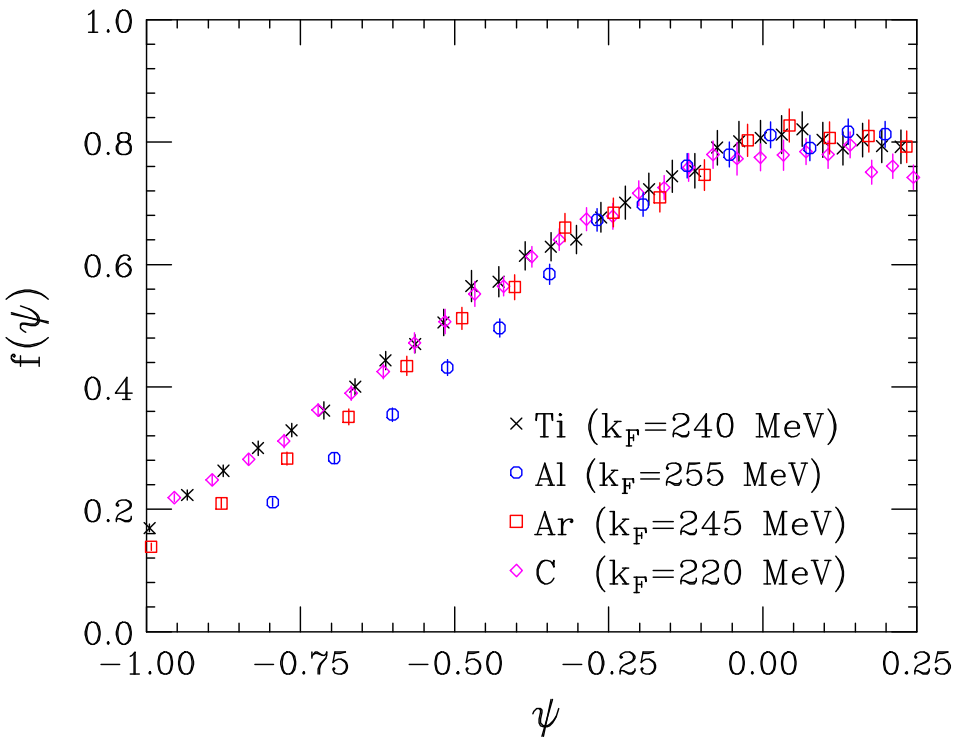

Figure 4.10: (color online) Scaling functions of second kind, obtained from the inclusive cross sections measured by the E12-14-012 experiment using carbon, aluminum, argon and titanium targets.

scaling variable, ψ, and scaling function, $f(\psi)$, involve a momentum scale, loosely referred to as nuclear Fermi momentum, providing a parametrization of the target-mass dependence of the measured cross sections.

Figure 4.10 illustrates the scaling functions obtained from the inclusive cross sections measured by the E12-14-012 experiment using carbon, aluminum, argon and titanium targets. The results shows that setting the carbon Fermi momentum to the value obtained from the independent analysis of Moniz *et al.* [35], $k_F = 220$ MeV, scaling of the second kind is shown when k_F values of 255, 245, and 240 MeV are taken for Al, Ar, and Ti respectively.

A different approach to describe the A-dependence of the nuclear inclusive cross section,

inspired by the considerations underlying the local density approximation of the nucleus [51], has been proposed by the authors of Ref. [52]. Their analysis—aimed at obtaining the inclusive cross section per nucleon of isospin-symmetric nuclear matter from an extrapolation of the available data—shows that the ^{12}C, ^{27}Al, ^{56}Fe, and ^{197}Au cross sections at Q^2 ranging between 0.25 and 2.70 GeV^2 exhibit a striking linear behavior when plotted as a function of $A^{-1/3}$. The extension of this study to the data set collected by the E12-14-012 experiment is under way, and the results will be discussed elsewhere.

4.7 Summary and Conclusions

We have reported on the measurements of the cross sections for inclusive electron scattering over a broad range of energy transfers, extending from the particle-emission threshold to above the excitation of the first hadronic resonance. These high precision data were taken at Jefferson Lab in Hall A for a beam energy of $E = 2.222$ GeV and electron scattering angle $\theta = 15.54°$ from four nuclear targets: carbon, aluminum, argon, and titanium. The reported results give unique opportunity to validate nuclear models employed in Monte Carlo simulations of precise long-baseline neutrino-oscillation experiments, and to assess their contribution to uncertainties of the oscillation analysis in a rigorous manner.

We find (see Fig. 4.6) that the per-nucleon responses for the considered four targets are strikingly similar over the entire energy transfer range ($0.05 < \omega < 0.90$ GeV), save at the maximum of the quasielastic peak and the dip region. At the kinematics from the maximum of the quasielastic peak to the onset of the Δ resonance, the result for carbon stands apart from those for aluminum, argon, and titanium. This finding shows that the momentum and energy distribution of nucleons in the nuclear ground state and final-state interactions—inducing the 'Doppler' broadening of the scattered electron's final energy—in carbon is not

as pronounced as for the heavier nuclei. When accounting is made for the number of protons and neutrons in each nucleus, this feature does not disappear, as can be seen in Fig. 4.7.

When the aluminum data set along with higher Q^2 data from SLAC are presented in terms of the y-scaling analysis (Fig. 4.8) the set behaves as expected, and the scaling behavior is clearly observed at the kinematics corresponding to the quasi-free peak. While in the absence of FSI, the scaling function $F(y)$ is expected to converge from below with increasing Q^2, the effect of FSI—falling with Q^2—leads it to converge from above. These new data fit this pattern (Fig. 4.9).

Taken together this data set will allow us to predict the electromagnetic nuclear responses for nuclei between $A = 12$ and 48 by interpolation as a function of $A^{-1/3}$. Of particular interest will be oxygen, as water serves as the target and radiator in the large Čerenkov detector of T2K [32], and chlorine, as polyvinyl chloride composes the detectors of NOvA [53].

Chapter 5

Measurement of the Ar(e,e′p) and Ti(e,e′p) cross sections in Jefferson Lab Hall A

The work described in this chapter was contributed by: Linjie Gu, Daniel Abrams, et al, (The Jefferson Lab Hall A Collaboration). It has been published on Physical Review C as:

Linjie Gu, Daniel Abrams, et al, (The Jefferson Lab Hall A Collaboration), "Measurement of the Ar(e,e′p) and Ti(e,e′p) cross sections in Jefferson Lab Hall A" [54].

Reproduced with permission from the American Physical Society. Copyright (2021) by the American Physical Society.

I contributed major part of the data analysis work in this paper under Prof. C. Mariani's supervision. I have contributed to the data analysis, computed the detector efficiencies, acceptance corrections and the detailed calculation for the systematic uncertainties together with producing most of the plots presented in the paper.

5.1 Introduction

Jefferson Lab experiment E12-14-012 was primarily aimed at obtaining the proton spectral function (SF) of the nucleus ^{40}Ar from a measurement of the cross section of the $(e, e'p)$ reaction

$$e + A \rightarrow e' + p + (A-1)^*, \tag{5.1}$$

in which the scattered electron and the knocked out proton are detected in coincidence. Here A denotes the target nucleus in its ground state, while the recoiling $(A-1)$-nucleon system can be either in the ground state or in any excited state.

Nucleon knockout processes have long been recognized as being ideally suited to study the momentum and removal energy distribution of protons bound in atomic nuclei [55]. Compared to the pioneering studies carried out using proton beams, see, e.g., Ref. [56], $(e, e'p)$ experiments have clear advantages, because they are largely unaffected by strong initial and final state interactions (FSI) between the beam particle and the target, and give access to the properties of deeply bound protons in medium-mass and heavy nuclei [57].

Under the basic assumption that the scattering process involves individual nucleons, and neglecting FSI between the outgoing proton and the spectator nucleons, the momentum and removal energy of the knocked out particle, $\mathbf{p}$ and E, can be reconstructed from measured kinematical variables, and the cross section of the process is written in simple factorized form in terms of the spectral function of the target nucleus, $P(\mathbf{p}, E)$, trivially related to the nucleon Green's function, $G(\mathbf{p}, E)$, through

$$P(\mathbf{p}, E) = \frac{1}{\pi} \text{ Im } G(\mathbf{p}, E). \tag{5.2}$$

As a consequence, the spectral function—yielding the probability to remove a proton with momentum $\mathbf{p}$ from the target nucleus leaving the residual system with excitation energy $E - E_{\rm thr}$, with $E_{\rm thr}$ being the proton emission threshold—can be readily obtained from the data.

Significant corrections to the somewhat oversimplified scheme outlined above—referred to as Plane Wave Impulse Approximation, or PWIA—arise from the occurrence of FSI. The large body of work devoted to the analysis of $(e, e'p)$ data has provided convincing evidence that the effects of FSI can be accurately included by replacing the plane wave describing the motion of the outgoing proton with a distorted wave, eigenfunction of a phenomenological optical potential accounting for its interactions with the mean field of the residual nucleus. In general, the $(e, e'p)$ cross section computed within this approach, known as Distorted Wave Impulse Approximation, or DWIA, involves the off-diagonal spectral function, and cannot be written in factorized form [58]. However, an approximate procedure restoring factorization, referred to as factorized DWIA, has been shown to yield accurate results in the case of parallel kinematics, in which the momentum of the outgoing proton and the momentum transfer are parallel [59]. In this kinematical setup, the spectral function can still be reliably obtained from $(e, e'p)$ data after removing the effects of FSI.

Additional corrections to the PWIA arise from the distortion of the electron wave functions resulting from interactions with the Coulomb field of the nucleus. However, it has been shown that, for nuclei as heavy as ^{40}Ca, this effect can be accurately taken into account using an effective momentum transfer [60].

Systematic measurements of $(e, e'p)$ cross sections in the kinematical regime in which the recoiling nucleus is left in a bound state, performed at Saclay [15] and NIKHEF-K [61], have allowed the determination of the spectral functions of a broad set of nuclei. These studies have provided a wealth of information on the energies and momentum distributions of shell-

model states belonging to the Fermi sea of the target nuclei, showing at the same time the limitations of the mean-field description and the importance of correlation effects [55].

Besides being a fundamental quantity of nuclear many-body theory, containing important dynamical information, the spectral function is a powerful tool, allowing to obtain the cross sections of a variety of nuclear scattering processes in the kinematical regime in which the beam particles primarily interact with individual nucleons, and FSI can be treated as corrections. Applications to inclusive electron-nucleus scattering have offered vast evidence that the formalism based on spectral functions provides a comprehensive and consistent framework for the calculation of nuclear cross sections in a broad kinematical region, extending from quasielastic (QE) scattering to resonance production and deep-inelastic scattering [62, 63, 64].

Over the past several years, a great deal of work has been devoted to applying the spectral function formalism to the study of neutrino-nucleus interactions, whose quantitative understanding is needed for the interpretation of accelerator-based searches of neutrino oscillations, see, e.g., Refs. [8, 31]. In this context, it should be noted that the capability to describe a variety of reaction channels within a unified approach is a critical requirement, because the energy of the beam particles is distributed according to a broad flux, typically ranging from a few hundreds of MeV to a few GeV. Moreover, the knowledge of the spectral function greatly improves the accuracy of reconstruction of the neutrino energy, a key quantity in the oscillation analysis [65, 66].

Realistic models of the nuclear spectral functions have been obtained from the approach based on the local density approximation, or LDA, in which the information on the shell-model structure extracted from $(e, e'p)$ data is combined to the results of accurate calculations of uniform nuclear matter at various densities [63]. The existing calculations of neutrino-nucleus cross sections employing LDA spectral functions [9, 64, 65, 67, 68, 69, 70, 71, 72, 73, 74, 75, 76], however, are limited to the isospin-symmetric p-shell targets ^{16}O and ^{12}C.

Therefore, the results of these studies are applicable to experiments using water-Čerenkov detectors, e.g. Super-Kamiokande [77], and mineral oil detectors, e.g. MiniBooNE [78].

The analysis of the data collected by the ongoing and future experiments using liquid-argon time-projection chambers, notably the Fermilab Short-Baseline Neutrino program (SBN) [79] and the Deep Underground Neutrino Experiment (DUNE) [80], will require the extension of this approach to the case of a heavier target with large neutron excess. Moreover, in DUNE the proton and neutron spectral functions will both be needed, to extract the Dirac phase δ_{CP} from a comparison of neutrino and antineutrino oscillations, and achieve an accurate description of pion production on protons and neutrons.

In the absence of direct measurements, information on the neutron momentum and removal energy distribution in ${}^{40}_{18}$Ar can be inferred from Ti$(e, e'p)$ data, exploiting the correspondence between the proton spectrum of titanium, having charge $Z = 22$, and the neutron spectrum of argon, having $A - Z = 22$. The viability of this procedure is supported by the results of Ref. [81], whose authors have performed a calculation of the inclusive ^{40}Ar(e, e') and ^{48}Ti(e, e') cross sections within the framework of the self-consistent Green's function approach. The aim of Jlab experiment E12-14-012, is the determination of the proton spectral functions of argon and titanium from the corresponding $(e, e'p)$ cross sections.

In this article, we present the first results of our analysis. In Sec. 5.2 we discuss the kinematic setup, the detectors and their resolutions, and our definitions of signal and backgrounds. In Sec. 5.3 we introduce the missing energy and the missing momentum, which are the fundamental variables of our analysis, and discuss the main elements of the Monte Carlo (MC) simulations employed for event simulation. Sec. 5.4 is devoted to the uncertainties associated with our analysis, while in Sec. 5.5 the measured missing energy and missing momentum distributions are compared with the MC predictions. Finally, in Sec. 5.6 we summarize our work and draw the conclusions.

Table 5.1: Kinematics settings used to collect the data analyzed here.

	E'_e (GeV)	θ_e (deg)	Q^2 (GeV^2/c^2)	$\lvert P\rvert$ (MeV/c)	$T_{p'}$ (MeV)	$\theta_{p'}$ (deg)	$\lvert\mathbf{q}\rvert$ (MeV/c)	p_m (MeV/c)	E_m (MeV)
Ar	1.777	21.5	0.549	915	372	−50.0	865	50	73
Ti	1.799	21.5	0.556	915	372	−50.0	857	58	51

5.2 Experimental Setup

The experiment E12-14-012 was performed at Jefferson lab in Spring 2017. Inclusive (e, e') and exclusive $(e, e'p)$ electron scattering data were collected on targets of natural argon and natural titanium, as well as on calibration and background targets of carbon and aluminum. The average neutron numbers calculated according to the natural abundances of isotopes are 21.98 for argon and 25.92 for titanium [27]. Therefore, from now on we will refer to the targets considered here as ^{40}Ar and ^{48}Ti, for brevity.

The E12-14-012 experiment used an electron beam of energy 2.222 GeV provided by the Continuous Electron Beam Accelerator Facility (CEBAF) at Jefferson Lab. The average beam current was approximately 15 μA for the ^{40}Ar target and 20 μA for the ^{48}Ti target. The scattered electrons were momentum analyzed and detected in the left high-resolution spectrometer (HRS) in Hall A and the coincident protons were similarly analyzed in the right HRS. The spectrometers are equipped with two vertical drift chambers (VDCs) providing tracking information [24], two scintillator planes for timing measurements and triggering, double-layered lead-glass calorimeter, a gas Čerenkov counter used for particle identification [19], pre-shower and shower detectors (proton arm only) [19] and pion rejectors (electron arm only) [19]. The HRSs were positioned with the electron arm at central scattering angle $\theta_e = 21.5$ deg and the proton arm at an angle $\theta_{p'} = -50$ deg. The beam current and position, the latter being critical for the electron-vertex reconstruction and momentum calculation, were monitored by resonant radio-frequency cavities (beam current monitors, or BCMs [19])

and cavities with four antennae (beam position monitors, or BPMs [19]), respectively. The beam size was monitored using harp scanners, which consists of a thin wire which moves through the beam. We used a raster of 2×2 mm^2 area to spread the beam and avoid overheating the target.

The experiment employed also an aluminum target and a set of carbon targets, used to evaluate backgrounds and monitor the spectrometers optics. The aluminum target was made of two identical foils of the Al-7075 alloy with a thickness of 0.889 ± 0.002 g/cm^2. One of the aluminum foils was positioned to match the entrance and the other to match the exit windows of the argon gas target cell. The two thick foils were separated by a distance of 25 cm, corresponding to the length of the argon gas cell and the Al foil's thickness.

The analysis presented here uses data collected with the settings given in Table 5.1. All of our data were taken in parallel kinematics, in which the momentum transfer, q, and the momentum of the outgoing proton, P, are parallel. The only difference of data collection setting for ^{40}Ar and ^{48}Ti is the scattered electron energy.

The VDCs' tracking information was used to determine the momentum and to reconstruct the direction (in-plane and out-of-plane angles) of the scattered electron and proton, and to reconstruct the interaction vertex at the target. We used both the electron and proton arm information separately to reconstruct the interaction vertex and found them in very good agreement. The transformation between focal plane and target quantities was computed using an optical matrix, the accuracy of which was verified using the carbon multi-foil target data and sieve measurements as described in previous papers [27, 36, 37]. Possible variations of the optics and magnetic field in both HRSs are included in the analysis as systematic uncertainties related to the optics.

Several different components were used to build the triggers: the scintillator planes on both

the electron and proton spectrometers, along with signals from the gas Čerenkov (GC) detector, the pion rejector (PR), the pre-shower and the shower detector (PS). Table 5.2 lists the trigger configurations, including details on how the signals from the various detector components are combined to form a trigger.

Table 5.2: Trigger lists detailing how the signals from different detector components are combined. LEFT and RIGHT identify the electron and proton arm, respectively.

T1	(S_0&&S_2) and (GC||PR) [LEFT]
	and (S0&&S2) [RIGHT]
T2	(S_0||S_2) and (GC||PR) [LEFT]
	and (S_0||S_2) and not(PS) [RIGHT]
T3	(S_0&&S_2) and (GC||PR) [LEFT]
T4	(S_0&&S_2) [RIGHT]
T5	(S_0||S_2) and (GC||PR) [LEFT]
T6	(S_0||S_2) and not(PS) [RIGHT]

The triggers used for identifying electron and proton coincidence events were T1 and T2, where T2 was used to provide a data sample to calculate the overall T1 trigger efficiency and we were able to compute the efficiency of T1 using also the product of T3 and T4 efficiencies. If the proton and electron observations from the same event were perfectly paired, these values would be the same as T1 trigger efficiency.

Electrons and protons were selected in their corresponding HRS requiring only one reconstructed good track. For the electron we required also an energy deposit of at least 30% in the lead calorimeter ($E_{\text{cal}}/p > 0.3$) and a signal in the Čerekov detector of more than 400 analog-digital-converter (ADC) counts. Furthermore, the tracks were required to be within ± 3 mrad of the in-plane angle and ± 6 mrad of the out-of-plane angle with respect to the center ray of the spectrometer and have a dp/p of ± 0.06. Those latter conditions focused on removing events coming from the acceptance edges of the spectrometers. We used a cut on β for the proton arm between 0.6 and 0.8 to further isolate protons. We only included in our analysis events in which both the electron and the proton were recorded in a T1 trigger

timing window and for which the difference in the start time of the individual triggers was of just few ns (time coincidence cut). For the argon target we also required that the events originated within the central ±10 cm of the target cell to exclude contamination from the target entry and exit windows. By measuring events from the thick Al foils, positioned at the same entry and exit window of the target, we determined that the target cell contributions to the measured cross section was negligible (<0.1%). The same gas cell was used in another set of experiments and the contribution from an empty gas cell was measured and confirmed a very low contamination of events coming from the Al windows [21]. The spectrometer optics were calibrated using sieve slit measurements and their positions and angles were surveyed before and after moving the spectrometers for each kinematic settings. The survey precision was 0.01 rad and 0.01 mm respectively for the angle and positions of the spectrometers.

The efficiencies of the elements in the detector stack were studied by comparing rates in various combinations of secondary triggers as in Ref. [27, 36, 37]. Table 5.3 summarizes the efficiency for the trigger, acceptances and kinematical cuts. The live-time of the electronics was computed using the rates from scalers, which were independent of triggered events. The acceptance cuts efficiencies were computed using the MC simulation [39]. The efficiency calculations that are based on MC were evaluated multiple times using slightly different SF models in the MC. The effect of theory models was found to be negligible. Our MC model contains nuclear transparency correction [39, 82], but does not account for all FSI effects. We have studied the role of FSI by looking at kinematical distributions for various MC samples obtained using different ranges of the missing momentum p_m, defined as in Eq. (5.3), from lower to higher. We found that the electron arm dp/p distributions showed slight variations. We then decided not to use the electron arm dp/p as a kinematical cut in our analysis. The trigger efficiencies were computed using the other available trigger as described above.

Table 5.3: Summary of the efficiency analysis for the argon and titanium targets.

	Ar target	Ti target
a. Live time	98.0%	98.9%
b. Tracking	98.3%	98.3%
c. Trigger	92.3%	96.9%
d. Čerenkov cut	99.9%	96.6%
e. Calorimeter cut	97.8%	98.1%
f. β cut	95.6%	95.3%
g. Coincidence time cut	54.8%	55.5%

The time coincidence cut efficiency was evaluated selecting a sample of more pure signal events (using a tighter β cut) and looking at the ratio of events with and without the time coincidence cuts. The overall efficiency (between 39.6% and 48.9% across all kinematic regions for the ^{40}Ar target, and between 46.8% and 48.1% for the ^{48}Ti target) includes cuts on the coincidence triggers, calorimeters, both the lead and the Čerenkov counter, track reconstruction efficiency, live-time, tracking and β cut.

5.3 Data Analysis

5.3.1 The $(e, e'p)$ cross section

In electron-nucleus scattering an incident electron, with energy E_e, is scattered from a nucleus of mass M_A at rest. Electron scattering is generally described in the one-photon exchange approximation, according to which the incident electron exchanges a space-like photon, of energy ω and momentum q, with the target nucleus.

In $(e, e'p)$ experiments the scattered electron and a proton are detected in coincidence in the final state, and their momentum and energy are completely determined. If, in addition, the kinematics is chosen such that the residual nucleus is left in a specific bound state, the

reaction is said to be exclusive.

In the following, P, $T_{p'}$, and M will denote the momentum, kinetic energy, and mass of the outgoing proton, while the corresponding quantities associated with the recoiling residual nucleus will be denoted p_R, T_R, and M_R. The missing momentum and missing energy are obtained from the measured kinematical quantities using the definitions

$$p_m = q - P = p_R, \tag{5.3}$$

and

$$E_m = \omega - T_{p'} - T_R. \tag{5.4}$$

Exploiting energy conservation, implying

$$\omega + M_A = M + T_{p'} + M_R + T_R, \tag{5.5}$$

and writing the mass of the residual nucleus in the form

$$M_R = M_A - M + E_{\text{thr}} + E_x = M_{A-1} + E_x, \tag{5.6}$$

where E_{thr} and M_{A-1} denote the proton emission threshold and the mass of $(A-1)$-nucleon system in its ground state, respectively, Eq. (5.4) can be rewritten

$$E_m = E_{\text{thr}} + E_x. \tag{5.7}$$

The usual description of the exclusive $(e, e'p)$ reaction in the QE region assumes the direct knockout mechanism, which naturally emerges within the impulse approximation (IA). According to this picture, the electromagnetic probe interacts through a one-body current with

the quasi-free knocked out proton, while all other nucleons in the target act as spectators. In addition, if FSI between the outgoing nucleon and the spectators is negligible, PWIA can be applied, and the $(e, e'p)$ cross section reduces to the factorized form

$$\frac{d^6\sigma}{d\omega d\Omega_{e'} dT_{p'} d\Omega_{p'}} = K\sigma_{ep} P(-p_m, E_m), \tag{5.8}$$

where $K = |P|E_{p'}$, with $E_{p'} = \sqrt{P^2 + M^2}$. Here, σ_{ep} is the differential cross section describing electron scattering off a bound moving proton, stripped of the flux factor and the energy conserving delta-function [16, 83], while $P(-p_m, E_m)$ is the proton spectral function of Eq. (5.2). Note that Eqs. (5.3) and (5.4) imply that the arguments of the spectral function can be identified with the initial momentum and the removal energy of the struck nucleon, respectively. Therefore, Eq. (5.8) shows that within PWIA the nuclear spectral function, describing the proton momentum and energy distribution of the target nucleus, can be readily extracted from the measured $(e, e'p)$ cross section.

When FSI are taken into account, and the outgoing proton is described by a distorted wave function as prescribed by DWIA, the initial momentum of the struck nucleon is not trivially related to the measured missing momentum, and the cross section can no longer be written as in Eq. (5.8). However, the occurrence of y-scaling in inclusive electron-nucleus scattering [84, 85]—whose observation in the analysis of the Ar(e, e') and Ti(e, e') data is discussed in Refs. [36, 37]—indicates that the formalism based on factorization is still largely applicable in the presence of FSI.

In principle, within the approach of Refs. [28, 86, 87], the bound and scattering states are both derived from an energy dependent non-Hermitian optical-model Hamiltonian. While being fully consistent, however, this treatment involves severe difficulties. In practice, the bound-state proton wave functions are generally obtained from phenomenological approaches—

although a few studies based on realistic microscopic models of the nuclear Hamiltonian have been carried out for light and medium-heavy nuclei [88, 89]—while the scattering states are eigenfunctions of phenomenological optical potentials, the parameters of which are determined through a fit to elastic proton-nucleus scattering data.

The PWIA description provides a clear understanding of the mechanism driving the $(e, e'p)$ reaction, and the ensuing factorized expression of the coincidence cross section, Eq. (5.8), is essential to obtain from the data an intrinsic property of the target, such as the spectral function, independent of kinematics. As pointed out above, however, the occurrence of FSI leads to a violation of factorization, and makes the extraction of the spectral function from the measured cross section more complicated [28, 90]. Additional factorization-breaking corrections arise from the distortion of the electron wave functions, resulting from interactions with the Coulomb field of the target [60, 91, 92].

The general conditions to recover a factorized expression of the cross section are discussed in Refs. [28, 59, 86, 93, 94]. If these requirements are fulfilled, the DWIA cross section can be written in terms of a distorted spectral function according to

$$\frac{d^6\sigma}{d\omega d\Omega_{e'} dT_{p'} d\Omega_{p'}} = K\sigma_{ep} P^D(P, -p_m, E_m). \tag{5.9}$$

Note, however that, unlike the spectral function appearing in Eq. (5.8), the distorted spectral function is *not* an intrinsic property of the target, because it depends explicitly on the momentum of the outgoing nucleon, which in turn depends on the momentum transfer. The most prominent effects of the inclusion of FSI within the framework of DWIA are a shift and a suppression of the missing momentum distributions, produced by the real and imaginary part of the optical potential, respectively.

5.3.2 Data analysis details

The measured cross sections are usually analyzed in terms of missing-energy and missing-momentum distributions. For a value of E_m corresponding to a peak in the experimental missing-energy distribution, the data are usually presented in terms of the reduced cross section as a function of $p_m = |p_m|$. The reduced cross section, obtained from the measured cross section dividing out the kinematic factor K and the electron-proton cross section σ_{ep} can be identified with the spectral function in PWIA and with the distorted spectral function in the factorized DWIA of Eq. (5.9). The off-shell extrapolation of de Forest [16, 83] is generally used to describe the bound nucleon cross section.

The experimental reduced cross sections can be compared with the corresponding reduced cross section calculated using different theoretical models. The comparison of the results obtained from the un-factorized and factorized approaches allows one to make an estimate of the accuracy of the factorization scheme, as well as the sensitivity to the different factorization-breaking contributions.

The six-fold differential cross section as a function of p_m and E_m was extracted from the data using the $(e, e'p)$ event yield Y for each p_m and E_m bin

$$\frac{d^6\sigma}{d\omega d\Omega_{e'} dT_{p'} d\Omega_{p'}} = \frac{Y(p_m, E_m)}{B \times lt \times \rho \times BH \times V_B \times C_{\text{rad}}}, \tag{5.10}$$

where B is the total accumulated beam charge, lt is the live-time of the detector (fraction of time that the detector was able to collect and write data to disk), ρ is the target density (for argon, corrected for the nominal density of gas in the target cell), BH is the local density change due to the beam heating the gas cell times the gas expansion due to boiling effects (this correction is not included in the case of ^{48}Ti), V_B is the effect of the acceptance and kinematical cuts, and C_{rad} is the effect of the radiative corrections and bin center migration.

We used the SIMC spectrometer package [95] to simulate $(e, e'p)$ events corresponding to our particular kinematic settings, including geometric details of the target cell, radiation correction, and Coulomb effects. SIMC also provided the V_B and C_{rad} corrections as in Eq. (5.10). To simulate the distribution of missing energies and momenta of nucleons bound in the argon and titanium nuclei, SIMC was run with a test SF described in detail in the following subsection.

In Table 5.4 we summarize the energies of the shell model states comprising the ground states of ^{40}Ar and ^{48}Ti. In our analysis, in case two orbitals overlap in E_m, we set the energy range for the orbital to be the same, and we assumed the probability of emission of an electron to be the same. Table 5.4 also lists energies derived from previous data sets, as well as the energy used in the calculation of FSI effects according to the model described in Sec. 5.4.1.

Table 5.4: Parametrization of the missing energy distributions of $^{40}_{18}$Ar and $^{48}_{22}$Ti assumed in this analysis. The central peak position E_α, its width σ_α, and the lower (upper) bound on the considered energy range, E^α_{low} (E^α_{high}) are shown for each level α. All values are given in units of MeV.

α	E_α	σ_α	E^α_{low}	E^α_{high}
		argon		
$1d_{3/2}$	12.53	2	8	14
$2s_{1/2}$	12.93	2	8	14
$1d_{5/2}$	18.23	4	14	20
$1p_{1/2}$	28.0	8	20	45
$1p_{3/2}$	33.0	8	20	45
$1s_{1/2}$	52.0	8	45	70
		titanium		
$1f_{7/2}$	11.45	2	8	14
$2s_{1/2}$	12.21	2	14	30
$1d_{3/2}$	12.84	2	14	30
$1d_{5/2}$	15.46	4	14	30
$1p_{1/2}$	35.0	8	30	54
$1p_{3/2}$	40.0	8	30	54
$1s_{1/2}$	62.0	8	53	80

SIMC generates events for a broad phase-space, and propagates the events through a detailed

model of the electron and proton spectrometers to account for acceptances and resolution effects. Each event is weighted by the σ_{cc1} cross section of de Forest [16] and the SF. The final weighted events do not contain any background. As pointed out above, SIMC does not include FSI corrections other than for the nuclear transparency.

The data yield corrected for the above-mentioned factors is then integrated over E_m to get the cross section as function of p_m. We collected 29.6 (12.5) hours of data on Ar (Ti), corresponding to ≈44k (13k) events.

We estimated the background due to accidentals to be 2% (3%) for Ar (Ti), performing analysis for each bin of E_m and p_m. First, we selected events in T1 trigger in anti-coincidence between the electron and proton arms. This region corresponds to 100 times the nominal coincidence time window width (≈2 ns). Then, we re-scaled the total number of events found to the width of the coincidence peak to obtain a correct estimate of the background events. The background-event distributions were then generated and subtracted bin by bin from the E_m and p_m distributions.

5.3.3 Test spectral functions

The spectral function employed to simulate events in SIMC is based on the simplest implementation of the nuclear shell model,

$$P(\boldsymbol{p}_m, E_m) = \sum_\alpha |\phi_\alpha(\boldsymbol{p}_m)|^2 f_\alpha(E_m - E_\alpha) \ , \tag{5.11}$$

where the sum runs over all occupied states. In the above equation, $\phi_\alpha(\boldsymbol{p}_m)$ is the momentum-space wave function of the state α, normalized to unity, and $f_\alpha(E_m - E_\alpha)$ represents the distribution of missing energy peaked at the value E_α, reflecting the width of the corre-

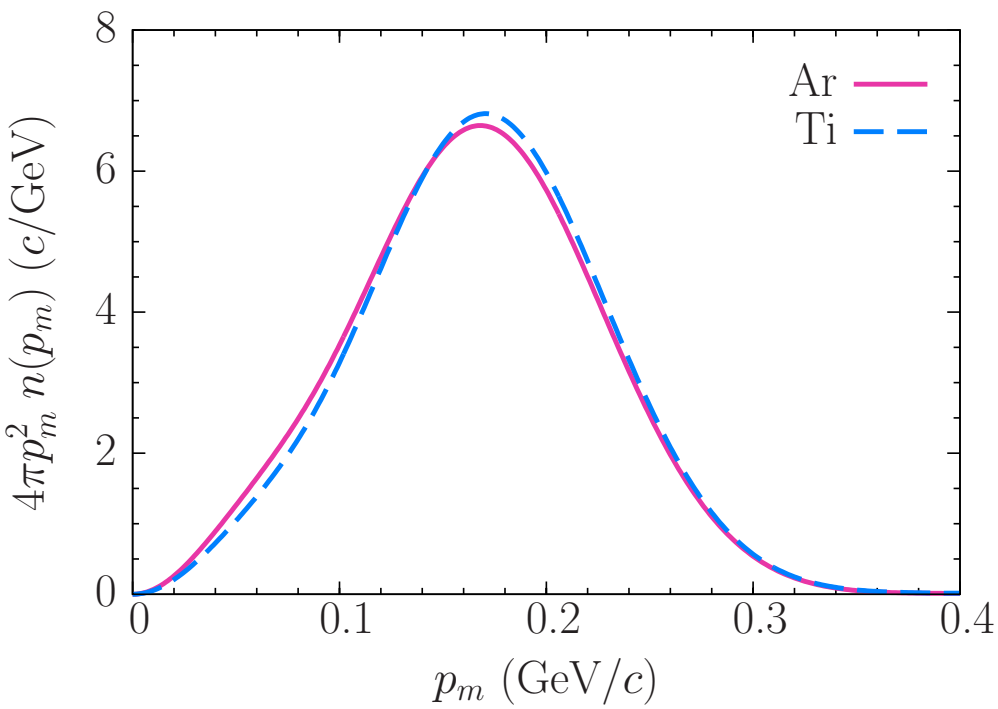

Figure 5.1: Missing momentum distributions of protons in argon and titanium assumed in this analysis.

sponding state. As a consequence of deviations from this mean-field picture originating from nucleon-nucleon correlations, we expect the Monte Carlo simulations typically to overestimate the data, due to the partial depletion of the shell-model states and to the correlated contribution to the nuclear spectral function.

We compared the momentum distribution, defined as

$$n(p_m) = \int P(p_m, E_m) dE_m, \tag{5.12}$$

obtained using the wave functions of Refs. [96, 97] and Ref. [98], and found that the differences between them are negligible for both argon and titanium. As shown in Fig. 5.1, the momentum distributions for argon and titanium also turn out not to differ significantly. This finding suggests that nuclear effects in argon and titanium are similar.

The missing energy distributions are assumed to be Gaussian

$$f_\alpha(E_m - E_\alpha) = \frac{1}{\sqrt{2\pi}\sigma_\alpha} \exp\left[-\frac{(E_m - E_\alpha)^2}{2\sigma_\alpha^2}\right]. \tag{5.13}$$

We obtain the missing energies of the least-bound valence orbital for protons—corresponding to the residual nucleus being left in the ground state, with an additional electron and the knocked-out proton at rest—from the mass difference of the residual system and the target nucleus [99]. These values of missing energy, corresponding to the $1d_{3/2}$ ($1f_{7/2}$) state for ${}^{40}_{18}$Ar (${}^{48}_{22}$Ti) in Table 5.4, are given by

$$E_{\text{thr}} = M_{A-1} + M + m - M_A,$$

where m stands for the electron mass.

In principle, the energies of other valence levels of ${}^{40}_{18}$Ar and ${}^{48}_{22}$Ti could be obtained from the excitation spectra of ${}^{39}_{17}$Cl [100] and ${}^{47}_{21}$Sc [101]. However, the fragmentation of shell-model states induced by long-range correlations makes this information difficult to interpret within the independent-particle model, assumed in Eq. (5.11), because a few spectroscopic lines typically correspond to a given spin-parity state. To overcome this issue and identify the dominant lines, we rely on the spectroscopic strengths determined in past direct pick-up experiments such as $A({}^2_1\text{H}, {}^3_2\text{He})$ for argon [102] and titanium [103].

The heavily fragmented $1d_{5/2}$ shell [102, 103]—with over 10, densely packed, spectroscopic lines contributing—can be expected to lend itself well to the approximation by a single distribution of finite width. To determine its peak position, in addition to the experimental data [102, 103], we use the theoretical analyses of Refs. [104, 105] as guidance.

Table 5.5: Contributions to systematical uncertainties for argon and titanium average over all the E_m and p_m bins.

	Ar	Ti
1. Total statistical uncertainty	0.53%	0.78%
2. Total systematic uncertainty	2.75%	2.39%
a. Beam x&y offset	0.56%	0.48%
b. Beam energy	0.10%	0.10%
c. Beam charge	0.30%	0.30%
d. HRS x&y offset	0.72%	0.69%
g. Optics (q1, q2, q3)	1.10%	0.34%
h. Acceptance cut (θ, ϕ, z)	1.23%	1.39%
i. Target thickness/density/length	0.2%	0.2%
j. Calorimeter & Čerenkov cut	0.02%	0.02%
k. Radiative and Coulomb corr.	1.00%	1.00%
l. β cut	0.63%	0.48%
m. Boiling effect	0.70%	—
n. Cross section model	1.00%	1.00%
o. Trigger and coincidence time cut	0.99%	0.78%

More deeper-lying shells—$1p_{1/2}$, $1p_{3/2}$, and $1s_{1/2}$—were not probed by the past experiments [102, 103]. Their E_α values, as well as the widths σ_α for all shells, are determined to provide a reasonable description of the missing-energy distributions obtained in this experiment. The resulting parametrization is detailed in Table 5.4, and presented in Fig. 5.2.

5.4 Uncertainty Analysis

The total systematic uncertainty in this analysis was estimated by summing in quadrature the contributions listed in Tab. 5.5. We determined the kinematic and acceptance cuts ensuring that there are no dependencies on kinematic variables and input theory model, in this way all uncertainties are uncorrelated bin to bin. All the kinematic and acceptance cuts were varied by the resolution of the variable under consideration. Except for the transparency corrections, the MC used to evaluate those uncertainties did not contain effects

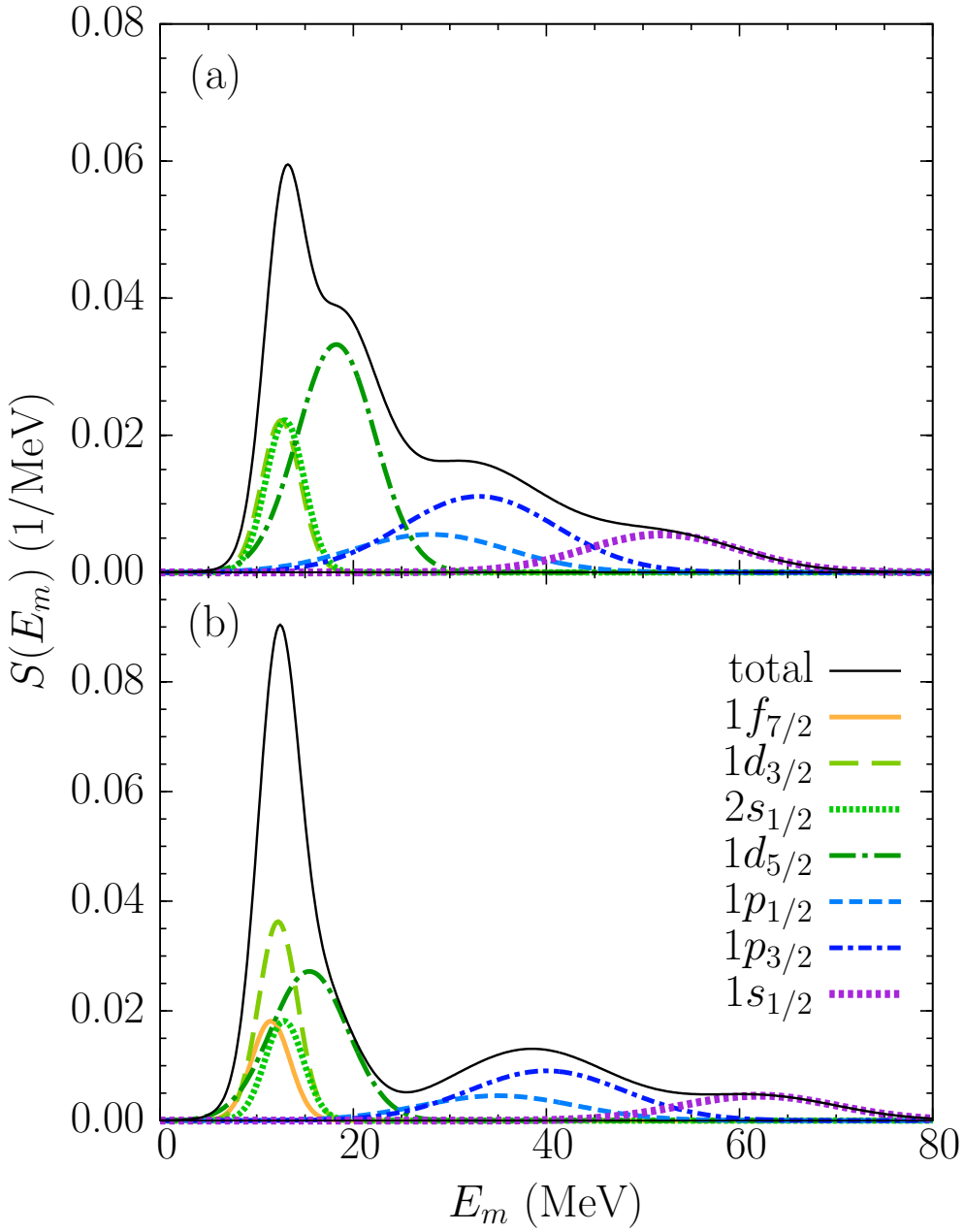

Figure 5.2: Missing energy distribution of protons in (a) argon and (b) titanium assumed in this analysis.

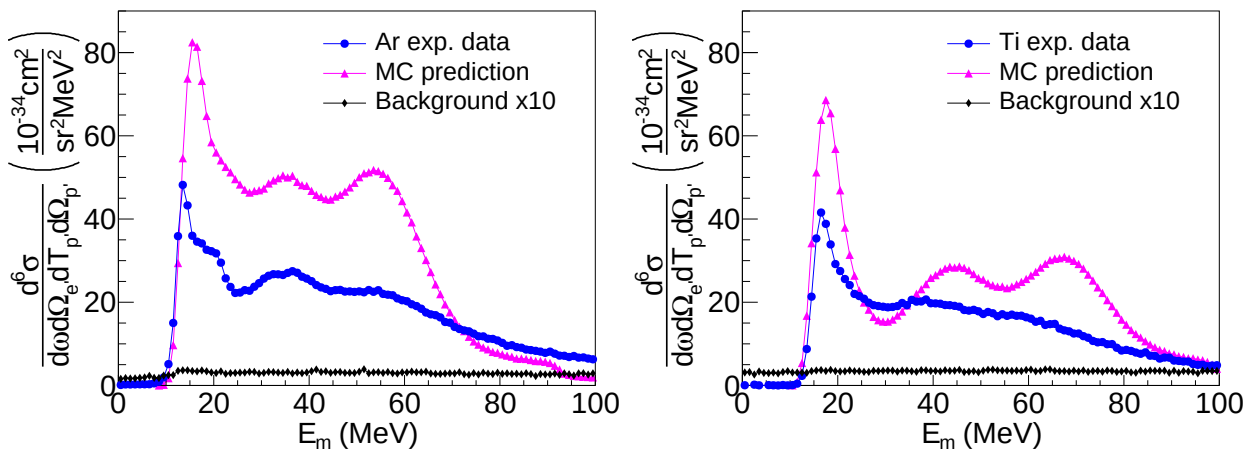

(a) Ar (b) Ti

Figure 5.3: Six-fold differential cross section as a function of missing energy for argon ((a) panel) and titanium ((b) panel). The background estimate (line connecting the experimental data points) is multiplied by 10 for purpose of presentation. The MC predictions, based on the mean-field SF, include a correction for the nuclear transparency, while other FSI effects are not accounted for.

due to FSI, such as a quenching of the strength of the cross section and a modification of the kinematic of the outgoing particles. *A priori* the MC simulation could depend on the underlying theoretical model. However, we repeated the analysis of systematic uncertainties varying its ingredients, and did not observe any substantial variations of the obtained results. As the obtained results depend on the Monte Carlo calculation, it is important to estimate uncertainties resulting from its inputs. To determine the uncertainties related to the target position, we performed the simulation with the inputs for the beam's and spectrometer's x and y offsets varied within uncertainties, and we recomputed the optical transport matrix varying the three quadrupole magnetic fields, one at the time. Each of these runs was compared to the reference run, and the corresponding differences were summed in quadrature to give the total systematic uncertainty due to the Monte Carlo simulation. The uncertainties related to the calorimeter and Čerenkov detectors were determined by changing the corresponding cut by a small amount and calculating the difference with respect to the nominal

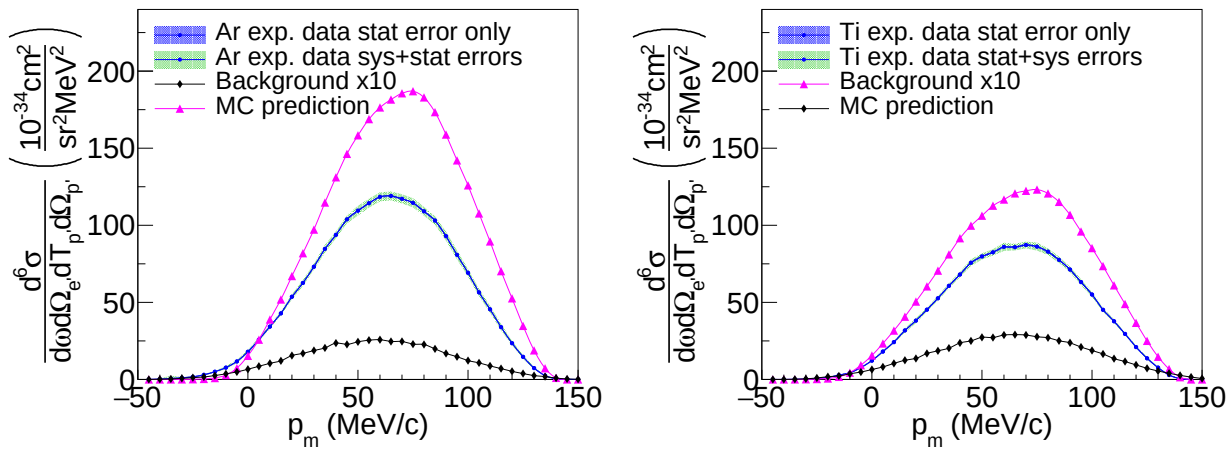

(a) Ar (b) Ti

Figure 5.4: Same as Fig. 5.3 but for the cross section as a function of missing momentum. The inner (outer) uncertainty bands correspond to statistical (total) uncertainties.

yield value. The uncertainty due to the acceptance cuts on the angles was calculated using the same method. We included an overall fixed uncertainty for both the beam charge and beam energy, as in the previous work on C, Ti, Ar, and Al [27, 36, 37]. We evaluated the systematic uncertainties related to the trigger efficiency by determining variations across multiple runs, as well as by applying different acceptance cuts. A fixed uncertainty was assigned to take care of those variations.

The time-coincidence cut efficiency, as other acceptance cuts, was evaluated by changing the cut by $\pm\sigma$.

SIMC generates events including the effects from radiative processes: vacuum polarization, vertex corrections, and internal bremsstrahlung. External radiative processes refer to electrons losing energy while passing through material in the target. Radiative correction in SIMC are implemented following the recipe of Dasu [40], using the Whitlow's approach [41, 106]. We considered a fixed 1% uncertainty due to the theoretical model for the radiative corrections over the full kinematic range as in our previous work. We generated different MC where the radiative corrections were re-scaled by $\sqrt{(Q^2)}/2$, Q^2 being

the four-momentum transfer squared, and re-analyzed the data and looked for variations. Coulomb corrections were included in the local effective momentum approximation [42]. A 10% uncertainty associated with the Coulomb potential was included as systematic uncertainty. Finally, we included a target thickness uncertainty and an uncertainty due to the boiling effect correction [21].

The measured and MC predicted differential cross sections $d^6\sigma/d\omega d\Omega_e dp d\Omega_p$ are presented in Fig. 5.3 as a function of E_m and in Fig. 5.4 as a function of p_m, integrated over the full range of E_m, for ^{40}Ar (panel (a)) and ^{48}Ti (panel (b)) targets.

The MC simulation clearly overestimates the extracted cross sections. As the nuclear model underlying the simulation neglects the effects of FSI other than the nuclear transparency and all correlations between nucleons, this difference is by no means surprising. Both FSI and partial depletion of the shell-model states require further studies, base on all five datasets collected by the JLab E12-14-012 experiment, which will be reported elsewhere.

5.4.1 Final state interactions

Within DWIA, FSI between the outgoing proton and the spectator nucleons are described by a complex, energy dependent, phenomenological optical potential (OP). The OPs available for calculations were determined by fitting a set of elastic proton-nucleus scattering data for a range of target nuclei and beam energies. Different parametrizations, yielding equivalently good descriptions of the data, can give differences and theoretical uncertainties when "equivalent" OPs are used in kinematical regions for which experimental data are not available, or when they are extended to inelastic scattering and to calculation of the cross section of different nuclear reactions.

Nonrelativistic and relativistic OPs are available for $(e, e'p)$ calculations within nonrelativis-

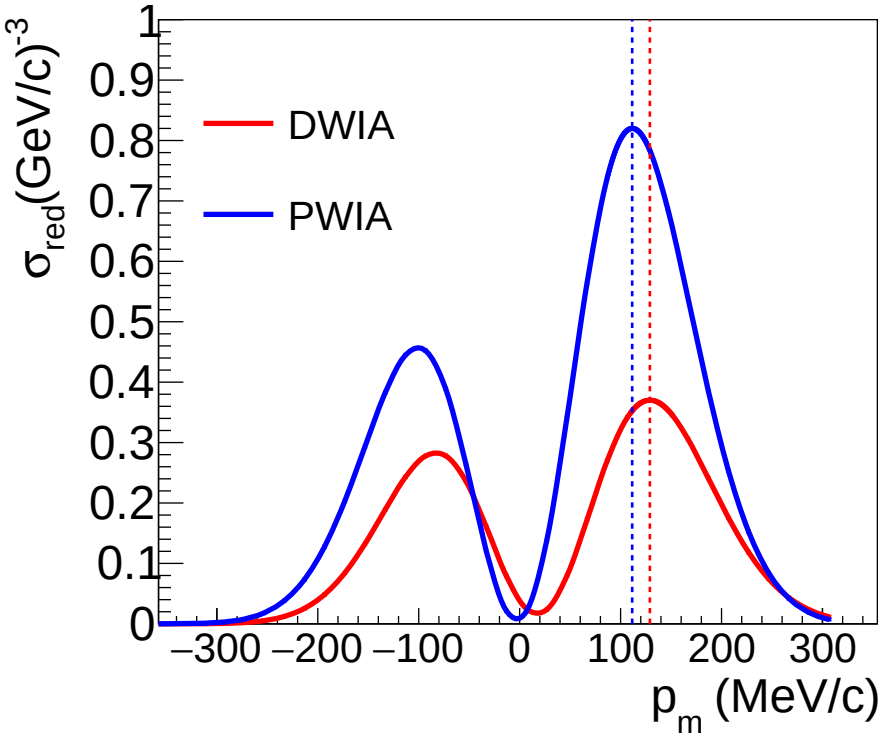

Figure 5.5: Reduced cross section as a function of missing momentum for the $1p_{1/2}$ proton knockout from argon. We compare the PWIA and DWIA results obtained for the parallel kinematics considered in this analysis.

tic and relativistic DWIA frameworks. However, nonrelativistic phenomenological OPs are available for energies not larger than 200 MeV. It is generally believed that above ≈180 MeV the Schrödinger picture of the phenomenological OP should be replaced by a Dirac approach, and a relativistic OP should be used. In Ref. [107], it was shown that in $(e, e'p)$ reactions the differences between the nonrelativistic and relativistic DWIA results depend on kinematics and increase with the outgoing proton energy, and for proton energies above 200 MeV a relativistic calculation is necessary.

We have used the so-called "democratic"(DEM) relativistic OP [108], obtained from a global fit to over 200 sets of elastic proton-nucleus scattering data, comprised of a broad range of targets, from helium to lead, at energies up to 1,040 MeV.

An example of the comparison between PWIA and DWIA results is given in Fig. 5.5, where

Table 5.6: Shifts between the reduced DWIA and PWIA cross sections, and the DWIA to PWIA cross-section ratios, obtained for proton knockout from various argon orbital using different optical potentials: DEM [108], EDAD3 [109], and EDAD1 [109]. All results are calculated for $p_m > 0$.

Orbital	Shift (MeV/c)			DWIA/PWIA		
	EDAD1	EDAD3	DEM	EDAD1	EDAD3	DEM
$1d_{3/2}$	1.5	-2.0	1.5	0.58	0.57	0.58
$2s_{1/2}$	8.0	7.0	8.0	0.78	0.78	0.78
$1d_{5/2}$	-2.0	-6.5	-3.0	0.57	0.57	0.58
$1p_{1/2}$	12.5	9.0	12.5	0.43	0.39	0.42
$1p_{3/2}$	9.5	5.0	9.0	0.47	0.44	0.46
$1s_{1/2}$	13.0	10.0	13.0	0.42	0.38	0.41

the reduced cross section as a function of p_m is displayed for proton knockout from the $1p_{1/2}$ argon orbital. Calculations are performed within the relativistic model of Ref. [107] for the parallel kinematics of the present experiment. Positive and negative values of p_m indicate, conventionally, cases in which $|q| < |p'|$ and $|q| > |p'|$, respectively. The reduction and the shift produced in the reduced cross section by FSI in the DWIA calculation can be clearly seen.

The two dashed lines drawn in the region of positive p_m of the figure indicate the value of p_m corresponding to the peaks of the DWIA and PWIA reduced cross sections. We use the distance between the two dashed lines as a measure of the shift produced by FSI.

The reduction of the calculated cross section produced by FSI can be measured by the DWIA/PWIA ratio, which is defined here as the ratio of the integral over p_m of the DWIA and PWIA reduced cross sections. Both the shift and the DWIA/PWIA ratios are computed separately for the positive and negative p_m regions.

The theoretical uncertainty of the shift and the reduction produced by FSI has been evaluated investigating the sensitivity of the DWIA and PWIA results to different choices of the theoretical ingredients of the calculation.

The uncertainty due to the choice of the OP has been evaluated by comparing the results obtained with the DEM and other energy-dependent and atomic-number dependent relativistic OPs, referred to as EDAD1 and EDAD3 [109] . The shift and the DWIA/PWIA ratio in the positive p_m region, computed for proton knock out from various argon orbitals using the DEM, EDAD1, and EDAD3 potentials are reported in Table 5.6. The results indicate a slight dependence of FSI effects on the choice of OP.

Note that the three OPs were determined by a fitting procedure of elastic proton scattering data over a wide range of nuclei, which, however, did not include argon. This means that the ability of the phenomenological OPs to describe elastic proton scattering data on argon is not guaranteed. A test of this ability is presented in Fig. 5.6, where the $^{40}\mathrm{Ar}(p,p')$ cross section calculated at 0.8 GeV with the three OPs is compared to the corresponding experimental cross section obtained using the HRS of the Los Alamos Meson Physics Facility [110]. The results of the three OPs largely overlap, and their agreement with the experimental cross section, although not perfect, is more than reasonable, in particular if we consider that it has not been obtained from a fit to the data.

In the relativistic DWIA and PWIA calculations different current conserving (cc) expressions of the one-body nuclear current operator can be adopted. The different expressions are equivalent for on-shell nucleons, while differences can arise for off-shell nucleons. For all the results that we have presented until now, and as a basis for the present calculations, we have adopted the cc1 prescription [16]. We note that, historically, the cc1 cross section has been often used to obtain the reduced cross section from the experimental and theoretical cross section. The impact of using a different cross section—such as the cc2 model of Ref. [16]—in the determination of the spectral function will be discussed in future analysis.

We have also checked that the differences obtained using different proton form factors in the calculation of the nuclear current are always negligible in the kinematic situation of the

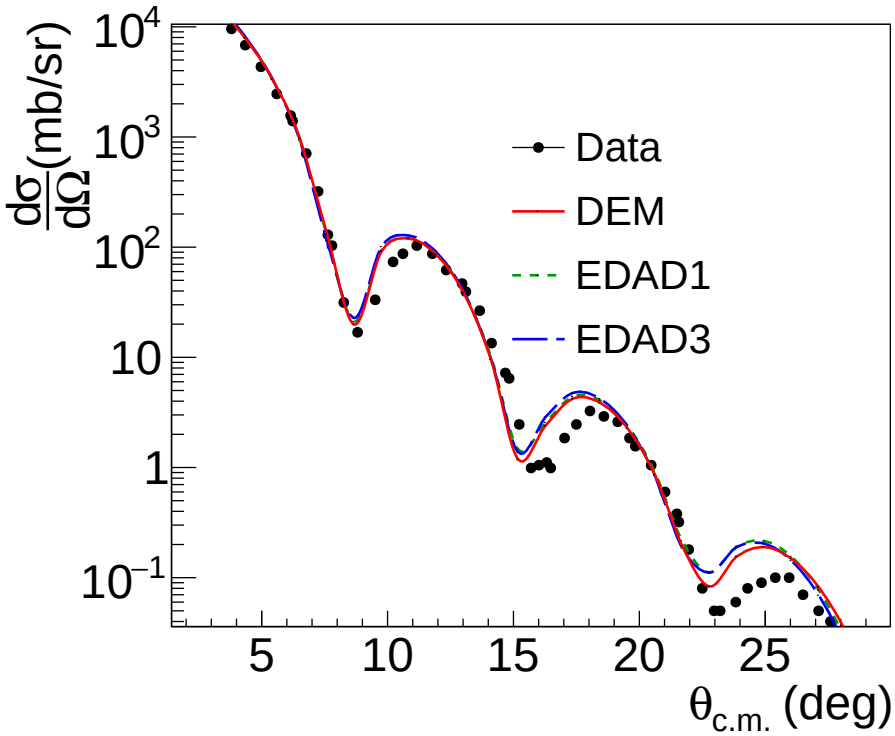

Figure 5.6: Differential cross section for elastic proton scattering on ^{40}Ar at 0.8 GeV as a function of scattering angle. Results for the DEM, EDAD1, and EDAD3 optical potentials, which turn out to almost completely overlap, are compared with the experimental data [110].

present experiment.

The bound proton states adopted in the calculations are self-consistent Dirac-Hartree solutions derived within a relativistic mean field approach using a Lagrangian containing σ, ω, and ρ mesons, with medium dependent parametrizations of the meson-nucleon vertices that can be more directly related to the underlying microscopic description of nuclear interactions [96, 97]. Pairing effects have been included carrying out Bardeen-Cooper-Schrieffer (BCS) calculations. The theoretical uncertainties on the shift and the DWIA/PWIA ratio due to the use of wave functions obtained with a different description of pairing, based on the relativistic Dirac-Hartree-Bogoliubov (DHB) model [98], turn out to be negligible.

In our analysis we assumed the missing energy distribution for each of the orbitals in ^{40}Ar and ^{48}Ti as shown in Fig. 5.2. The lower and upper energy bounds assumed in the DWIA analysis of FSI are given for each orbital in Table 5.4. The FSI correction has been applied event by event in both the missing energy and missing momentum distributions. We applied different corrections for events with $|q| < |p'|$ and $|q| > |p'|$, according to the theoretical predictions mentioned before. For each event, we used the reconstructed energy and momentum of both electron and proton to determine the orbital involved in the primary interaction. Then, we applied the FSI correction, based on the p_m sign. For orbitals that overlap we use a simple prescription to determine the most probable orbital from which the electron was emitted, as described in Sec. 5.3.2.

5.5 Differential cross section comparison

Figures 5.7 and 5.8 show a comparison between the measured differential cross sections of ^{40}Ar and ^{48}Ti and the MC predictions including full FSI corrections, plotted as a function of p_m for three different ranges of E_m. The missing energy regions for ^{40}Ar (^{48}Ti) are: $E_m <$

27 MeV ($E_m < 30$ MeV), $27 < E_m < 44$ MeV ($30 < E_m < 54$ MeV) and $44 < E_m < 70$ MeV ($54 < E_m < 90$ MeV).

We estimated the background to be of the order 2% for ^{40}Ar and 3% for ^{48}Ti. The MC systematic uncertainties from FSI are estimated by varying the following ingredients of the model:

(i) the optical potential (DEM, EDAD1, or EDAD3);

(ii) the pairing mechanism underlying the determination of the wave functions (the default BCS model [96, 97] or the DHB model [98]);

(iii) the parametrization of the nucleon form factors.

The total systematic uncertainty is obtained by adding in quadrature all the variations, and including an overall uncertainty of the theoretical model of 15%.

A prominent feature of both Figs. 5.7 and 5.8 is that the agreement between data and MC predictions including FSI, which turns out to be quite good in the region of low missing energies, becomes significantly worse at larger E_m. This behavior can be explained considering that, according to the shell-model picture employed in MC simulations, missing energies $E_m > 27$ MeV correspond to proton knockout from the deeply bound $1p_{1/2}$, $1p_{3/2}$, and $1s_{1/2}$ states.

As discussed in Sec. 5.3.3, the energies and widths of these states are only estimated, and not determined from experimental data. Underestimating the widths and the associated overlaps of energy distributions would imply a smaller value for the differential cross section and a shift in the p_m distribution between data and MC. We have tested this hypothesis by varying the width of the high-energy states in the test SF and redoing our full analysis, and noticed an improved agreement between data and MC.

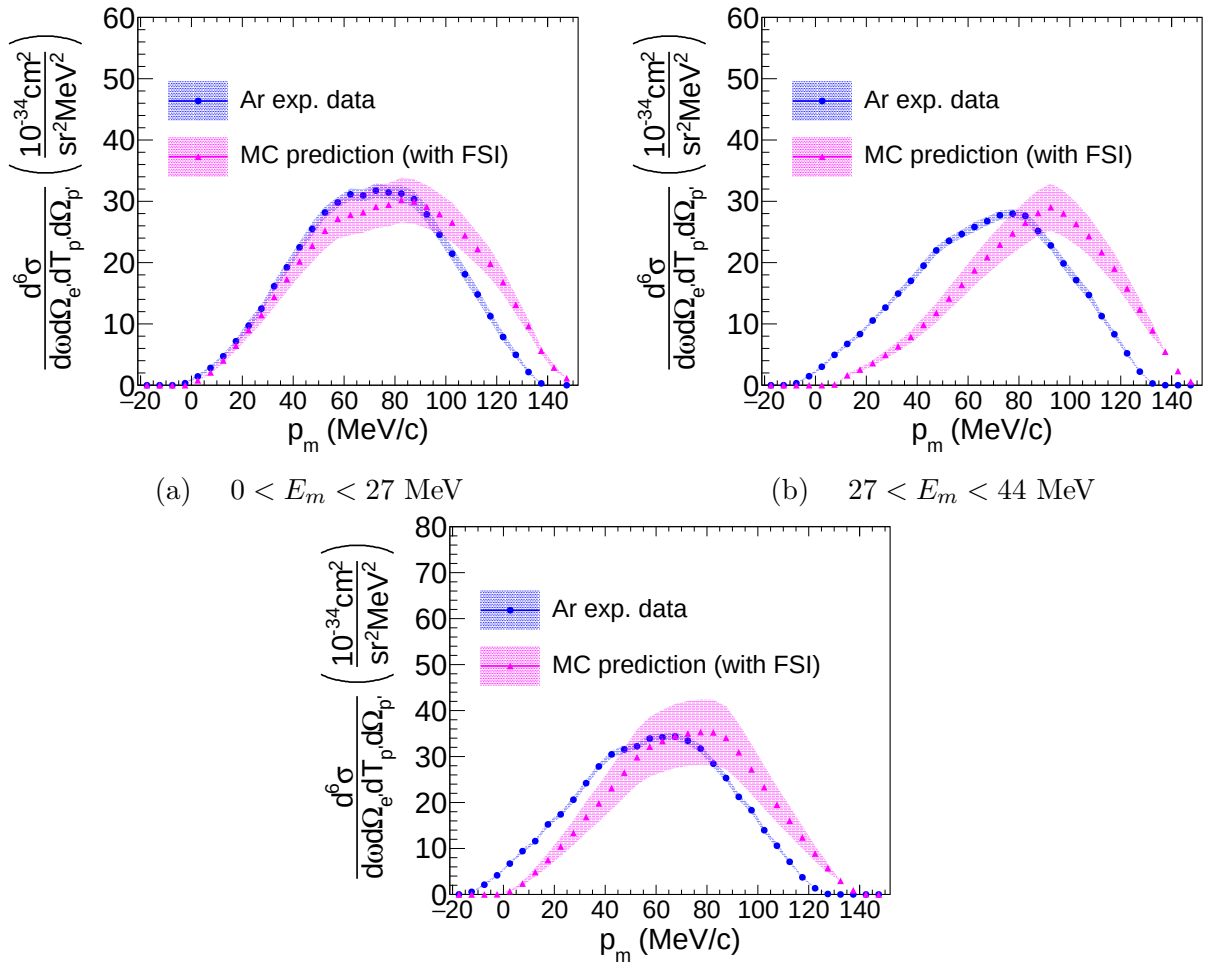

(a) $0 < E_m < 27$ MeV

(b) $27 < E_m < 44$ MeV

(c) $44 < E_m < 70$ MeV

Figure 5.7: Six-fold differential cross section for argon as a function of missing momentum integrated over different ranges of missing energy. The background estimate is multiplied by 10 for presentation. The MC predictions, based on the mean-field SF, include the full FSI corrections.

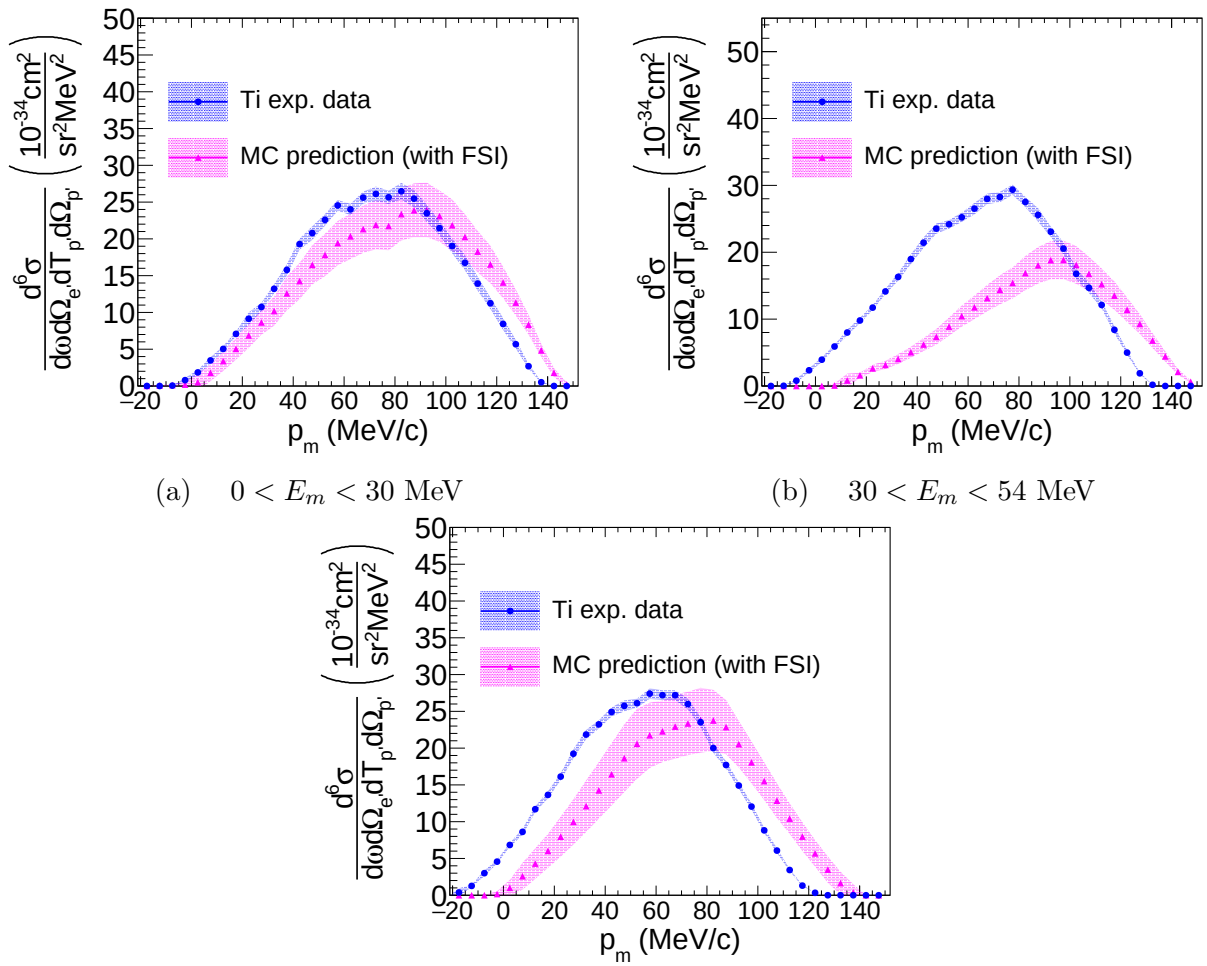

(a) $0 < E_m < 30$ MeV

(b) $30 < E_m < 54$ MeV

(c) $54 < E_m < 90$ MeV

Figure 5.8: Same as Fig. 5.7 but for titanium.

More generally, it has to be kept in mind that a clear identification of single particle states in interacting many-body systems—ultimately based on Landau theory of normal Fermi liquids—is only possible in the vicinity of the Fermi surface, corresponding to the lowest value of missing energy, see, e.g., Ref. [111]. An accurate description of the data at large missing energy will require a more realistic model of the nuclear spectral function, taking into account dynamical effects beyond the mean-field approximation, notably nucleon-nucleon correlations, leading to the appearance of protons in continuum states.

5.6 Summary and Conclusions

In this paper, we report the first results of the analysis of $(e, e'p)$ data at beam energy $E_e = 2.222$ GeV an electron scattering angle $\theta_e = 21.5$ deg, collected in JLab Hall A by the E12-14-012 experiment using Ar and Ti targets. The measured differential cross sections are presented as a function of missing energy and missing momentum, and compared to the predictions of a MC simulation in which the effects of FSI are described within DWIA.

We were able to select coincidence events between the electron and proton spectrometers with high efficiency and low systematic uncertainties. The level of background and systematic uncertainties turned out to be below 4%, in line with the goals listed in the original JLab E12-14-012 proposal [112]. Overall, the comparison between the data and results of MC simulations, carried out over the lowest missing energy range $0 < E_m < 30$ MeV and missing momentum covered by our measurements appears satisfactory. The larger discrepancies observed at the larger missing energies such as $30 < E_m < 44$ MeV re likely to be ascribable to the limitations of the theoretical model based on the mean-field approximation, employed in MC event generation, which is long known to be inadequate to describe the dynamics of deeply bound nucleons [55]. Understanding these discrepancies at quantitative level will

require the inclusion of reaction mechanisms beyond DWIA, such as multi-step processes and multi-nucleon emission triggered by nucleon-nucleon correlations.

The missing energy spectra obtained from our analysis contain valuable new information on the internal structure and dynamics of the nuclear targets, encoded in the positions and widths of the observed peaks.

The determination of these spectra particularly for deep-lying hole excitations is, in fact, a first step towards the derivation of the spectral functions for medium-mass nuclei, such as Ar and Ti, within the framework of LDA, that represents the ultimate aim of our experiment.

The Ar and Ti measurements discussed in this article, providing the first $(e, e'p)$ data in the kinematical range relevant to neutrino experiments—most notably DUNE—comprises the first of five datasets collected by the JLab E12-14-012 experiment. The combined analysis of all data, which is currently under way, will provide information of unparalleled value for the development of realistic nuclear models, and will allow the extraction of Ar and Ti spectral functions.

5.7 Acknowledgments

We acknowledge the outstanding support from the Jefferson Lab Hall A technical staff, target group and Accelerator Division. This experiment was made possible by Virginia Tech, the National Science Foundation under CAREER grant No. PHY−1352106 and grant No. PHY−1757087. This work was also supported by the DOE Office of Science, Office of Nuclear Physics, contract DE-AC05-06OR23177, under which Jefferson Science Associates, LLC operates JLab, DOE contract DE-FG02-96ER40950, DE-AC02-76SF00515, DE-SC0013615 and by the DOE Office of High Energy Physics, contract DE-SC0020262.

Chapter 6

Summary

The JLab E12-14-012 experiment at Jefferson Lab collected data using five kinematical settings and multiple targets (Argon, Titanium, Carbon and Aluminum). It provided high-precision measurement of (e, e') and $(e, e'p)$ cross section for those targets. This Ph.D. thesis summarizes part of inclusive and exclusive analysis results, and also includes the exclusive data analysis strategy for the JLab E12-14-012 experiment.

In this Ph.D. thesis, Chapter.1 shows the connection between neutrino scattering and electron scattering. Basic ideas about cross section calculation methods was also introduced in this chapter. In Chapter.2, after briefly reviewing the experimental setup, the data taking details were presented. A detailed analysis strategy for exclusive electron scattering was presented in Chapter.3 with efficiency and systematic uncertainties calculation methods introduced. Chapter.4 presented the inclusive electron scattering results as published in Phys. Rev. C.. The total uncertainties of all these measurements was below 5%. Lastly, in Chapter.5, the first exclusive electron scattering results on Ar and Ti was shown. The total uncertainties also in the case of the exclusive electron scattering were below 5%. This paper also shows the procedure to include the Final State Interaction (FSI) correction in our experiment.

In summary, the JLab E12-14-012 did a great job in measuring the inclusive and exclusive cross section of argon and titanium targets. Data collected can be used to build and validate nuclear model aiming at describing high accuracy neutrino-nucleus interactions. Neutrino experiments classify and reconstruct neutrino energy based on the observation of product

of the primary neutrino-nucleus scattering. Improving the knowledge of neutrino-nucleus scattering will improve the neutrino energy reconstruction and as a consequence will improve the precision of the determination of the neutrino oscillation parameters.

The future plan for the JLab E12-14-012 experiment is to extract spectroscopic factors and orbital info (mean energy and width) for the proton in Ar and Ti, that will provide unparalleled information to further develop the theoretical nuclear model and extract the spectral functions of Ar and Ti.

Bibliography

[1] O. Benhar, A. Fabrocini, S. Fantoni, and I. Sick, Nucl. Phys. A 579, 493 (1994).

[2] O. Benhar, N. Farina, H. Nakamura, M. Sakuda, and R. Seki, Phys. Rev. D 72, 053005 (2005).

[3] S.L. Glashow, Nucl. Phys. **22**, 579 (1961).

[4] S. Weinberg, Phys. Rev. Lett. **19**, 1264 (1967).

[5] A. Corey *et al.*, (DUNE Collaboration), arXiv preprint arXiv:1307.7335 (2013).

[6] B. Abi *et al.*, arXiv preprint arXiv:1807.10334 (2018).

[7] L. Alvarez-Ruso *et al.*, Prog. Part. Nucl. Phys. **100**, 1 (2018).

[8] O. Benhar, P. Huber, C. Mariani, and D. Meloni, Phys. Rep. **700**, 1 (2017).

[9] O. Benhar and D. Meloni, Nucl. Phys. **A789**, 379 (2007).

[10] O. Benhar, D. Day, I. Sick, Rev. Mod. Phys. **80**, 189 (2008).

[11] T. de Forest, J.D. Walecka, Adv. Phys. **15**, 1 (1966).

[12] Joaquín López Herraiz. Study of the (e, e'p) quasi-elastic reaction in complex nuclei: theory and experiment. Technical report, Thomas Jefferson National Accelerator Facility, Newport News, VA (United States), (2010).

[13] R. Jost and A. Pais, Phys. Rev. 82, 840 (1951).

[14] F. Chew and C. Wick, Phys. Rev. 85, 636 (1952).

[15] S. Frullani and J. Mougey, Adv. Nucl. Phys. **14**, 1 (1984).

[16] T. de Forest, Nucl. Phys. **A392**, 232 (1983).

[17] O. Benhar, *et al.* (The Jefferson Lab E12-14-012 Collaboration), arXiv:1406.4080 [nucl-ex].

[18] URL https://hallaweb.jlab.org/posters/halla/HallaGraphic.jpg.

[19] J. Alcorn *et al.*, Nucl. Instrum. Meth. A**522**, 294 (2004).

[20] W Barry *et al.* *JLab-TN-91-087*, (1991).

[21] S. N. Santiesteban *et al.*, Nucl. Instrum. Methods Phys. Res. A **940**, 351 (2019).

[22] D. Hongxia Ph.D. thesis. (2019)

[23] SN. Santiesteban *et al.*, Nucl. Instrum. Meth. A (2001).

[24] K. G. Fissum *et al.*, Nucl. Instrum. Meth. A **474**, 108 (2001). doi:10.1016/S0168-9002(01)00875-0

[25] Dan Green. *High Pt physics at hadron colliders* **22**. Cambridge University Press, (2005).

[26] Y. Zhihong, Ph.d. thesis. (2013).

[27] M. Murphy *et al.* (Jefferson Lab Hall A Collaboration), Phys. Rev. C **100**, 054606 (2019);

[28] S. Boffi, C. Giusti, F. D. Pacati, and M. Radici, *Electromagnetic Response of Atomic Nuclei* (Clarendon, Oxford, UK, 1996).

[29] P. K. A. de Witt Huberts, J. Phys. G **16**, 507 (1990).

[30] D. Rohe *et al.*, Phys. Rev. Lett. **93**, 182501 (2004).

[31] A. M. Ankowski and C. Mariani, J. Phys. G **44**, 054001 (2017).

[32] K. Abe *et al.* (T2K Collaboration), Phys. Rev. Lett. **121**, 171802 (2018).

[33] R. Acciari *et al.* (DUNE Collaboration), arXiv:1512.06148 [physics.ins-det].

[34] K. Abe *et al.* (Hyper-Kamiokande Proto-Collaboration), Prog. Theor. Exp. Phys. **2015**, 053C02 (2015).

[35] E. J. Moniz, I. Sick, R. R. Whitney, J. R. Ficenec, R. D. Kephart, and W. P. Trower, Phys. Rev. Lett. **26**, 445 (1971).

[36] H. Dai, *et al.*, (The Jefferson Lab Hall A Collaboration), Phys. Rev. C**98**, 014617 (2018).

[37] H. Dai *et al.* (Jefferson Lab Hall A Collaboration), Phys. Rev. C **99**, 054608 (2019).

[38] J. K. Tuli, Nuclear Wallet Cards, https://www.nndc.bnl.gov/wallet, 2011.

[39] J. Arrington *et al.*, Phys. Rev. Lett. **82**, 2056 (1999).

[40] S. R. Dasu, Precision Measurement of x, Q^2, and A-dependence of $R = \sigma_L/\sigma_T$ and F_2 in deep inelastic scattering, Ph.D. thesis, University of Rochester, 1988.

[41] L. W. Mo and Y. S. Tsai, Rev. Mod. Phys. **41**, 205 (1969).

[42] A. Aste, C. von Arx, and D. Trautmann, Eur. Phys. J. **A26**, 167 (2005).

[43] J. S. O'Connell *et al.*, Phys. Rev. C **35**, 1063 (1987).

[44] R. M. Sealock *et al.*, Phys. Rev. Lett. **62**, 1350 (1989).

[45] J. S. O'Connell *et al.*, Phys. Rev. Lett. **53**, 1627 (1984).

[46] D. T. Baran *et al.*, Phys. Rev. Lett. **61**, 400 (1988).

[47] I. Sick, D. B. Day, and J. S. McCarthy, Phys. Rev. Lett. **45**, 871 (1980).

[48] D. B. Day, J. S. McCarthy, T. W. Donnelly and I. Sick, Ann. Rev. Nucl. Part. Sci. **40**, 357 (1990).

[49] D. B. Day *et al.*, Phys. Rev. C **48**, 1849 (1993).

[50] T. W. Donnelly, and I. Sick, Phys. Rev. C **60**, 065502 (1999).

[51] A. N. Antonov and I. Zh. Petkov, Nuovo Cimento A **94**, 68 (1986).

[52] D. B. Day *et al.*, Phys. Rev. C **40**, 1011 (1989).

[53] R. L. Talaga, J. J. Grudzinski, S. Phan-Budd, A. Pla-Dalmau, J. E. Fagan, C. Grozis, and K. M. Kephart, Nucl. Instrum. Meth. A **861**, 77 (2017).

[54] L. Gu, et al. (Jefferson Lab Hall A Collaboration), Phys. Rev. C 103, no.3, 034604 (2021).

[55] O. Benhar, Nucl. Phys. News. **26**, 15 (2018).

[56] M. Riou *et al.*, Rev. Mod. Phys. **37**, 375 (1965).

[57] G. Jacob and Th. A. J. Maris, Nucl. Phys. **A31**, 139 (1962).

[58] D. H. E. Gross and R. Lipperheide, Nucl. Phys. **A150**, 449 (1960).

[59] S. Boffi, C. Giusti, F. Pacati, and S. Frullani, Nucl. Phys. **A319**, 461 (1979).

[60] C. Giusti and F. Pacati, Nucl. Phys. **A485**, 461 (1988).

[61] A. E. L. Dieperink and P. K. A. de Witt Huberts, Ann. Rev. Nucl. Part. Sci. **40**, 239 (1990).

[62] O. Benhar and V. R. Pandharipande, Phys. Rev. C **47**, 2218 (1993).

[63] O. Benhar, A. Fabrocini, S. Fantoni, and I. Sick, Nucl. Phys. **A579**, 493 (1994).

[64] A. M. Ankowski, O. Benhar, and M. Sakuda, Phys. Rev. D **91**, 033005 (2015).

[65] O. Benhar and D. Meloni, Phys. Rev. D **80**, 073003 (2009).

[66] C.-M. Jen, A. M. Ankowski, O. Benhar, A. P. Furmanski, L. N. Kalousis, and C. Mariani, Phys. Rev. D **90**, 093004 (2014).

[67] O. Benhar, N. Farina, H. Nakamura, M. Sakuda, and R. Seki, Phys. Rev. D **72**, 053005 (2005).

[68] A. M. Ankowski, O. Benhar, and N. Farina, Phys. Rev. D **82**, 013002 (2010).

[69] O. Benhar, P. Coletti, and D. Meloni, Phys. Rev. Lett. **105**, 132301 (2010).

[70] A. M. Ankowski, O. Benhar, T. Mori, R. Yamaguchi, and M. Sakuda, Phys. Rev. Lett. **108**, 052505 (2012).

[71] A. M. Ankowski, Phys. Rev. C **86**, 024616 (2012).

[72] A. M. Ankowski and O. Benhar, Phys. Rev. D **88**, 093004 (2013).

[73] A. M. Ankowski, Phys. Rev. D **92**, 013007 (2015).

[74] A. M. Ankowski, M. B. Barbaro, O. Benhar, J. A. Caballero, C. Giusti, R. González-Jiménez, G. D. Megias, and A. Meucci, Phys. Rev. C **92**, 025501 (2015).

[75] E. Vagnoni, O. Benhar, and D. Meloni, Phys. Rev. Lett. **118**, 142502 (2017).

[76] A. M. Ankowski, Phys. Rev. C **96**, 035501 (2017).

[77] S. Fukuda *et al.*, Nucl. Instrum. Methods Phys. Res. A **599**, 28 (2003).

[78] A. A. Aguilar-Arevalo *et al.* (MiniBooNE Collaboration), Nucl. Instrum. Methods Phys. Res A **501**, 418 (2009).

[79] M. Antonello *et al.* (The MicroBooNE, LAr1-ND, and ICARUS-WA104 Collaborations), arXiv:1503.01520.

[80] B. Abi *et al.* (DUNE Collaboration), J. Instr. **15**, T08008 (2020).

[81] C. Barbieri, N. Rocco, and V. Soma, Phys. Rev. C **100**, 062501(R) (2019).

[82] Frankfurt, M. Strikman, and M. Zhalov, Phys. Lett. **B503**, 73 (2001).

[83] A. E. L. Diepereink, T. de Forest Jr., I. Sick, and M.A. Brandenburg, Phys. Lett. **B63**, (1976).

[84] I. Sick, D. B. Day, and J. S. McCarthy, Phys. Rev. Lett. **45**, 871 (1980).

[85] T. W. Donnelly, and I. Sick, Phys. Rev. C **60**, 065502 (1999).

[86] S. Boffi, C. Giusti, and F. D. Pacati, Phys. Rep. **226**, 1 (1993).

[87] S. Boffi, F. Cannata, F. Capuzzi, C. Giusti, and F. D. Pacati, Nucl. Phys. **A379**, 509 (1982).

[88] M. Radici, S. Boffi, S. C. Pieper, and V. R. Pandharipande, Phys. Rev. C **50**, 3010 (1994).

[89] C. Bisconti, F. Arias de Saavedra, and G. Cò, Phys. Rev. C **75**, 054302 (2007).

[90] M. Bernheim, A. Bussière, J. Mougey, D. Royer, D. Tarnowski, S. Turck–Chièze, S. Frullani, S. Boffi, C. Giusti, F. D. Pacati, G. P. Capitani, E. de Sanctis, and G. J. Wagner, Nucl. Phys. **A375**, 381 (1982).

[91] C. Giusti, F. D. Pacati, Nucl. Phys. **A473**, 717 (1987).

[92] J. M. Udías, P. Sarriguren, E. Moya de Guerra, E. Garrido and J. A. Caballero, Phys. Rev. C **48**, 2731 (1993).

[93] S. Boffi, C. Giusti, F. D. Pacati, Nucl. Phys. **A336**, 437 (1980).

[94] J. R. Vignote, M. C. Martínez, J. A. Caballero, E. Moya de Guerra, and J. M. Udías, Phys. Rev. C **70**, 044608 (2004).

[95] SIMC, https://hallcweb.jlab.org/wiki/index.php/SIMC_Monte_Carlo.

[96] P. Finelli, N. Kaiser, D. Vretenar, and W. Weise, Nucl. Phys. **A735**, 449 (2004).

[97] P. Finelli, N. Kaiser, D. Vretenar, and W. Weise, Nucl. Phys. **A770**, 1 (2006).

[98] T. Nikšić, N. Paar, D. Vretenar, and P. Ring, Comput. Phys. Commun. **185**, 1808 (2014).

[99] Meng Wang, G. Audi, F. G. Kondev, W. J. Huang, S. Naimi, and Xing Xu, Chin. Phys. C **41**, 030003 (2017).

[100] J. Chen, Nucl. Data Sheets **149**, 1 (2018).

[101] T. W. Burrows, Nucl. Data Sheets **108**, 923 (2007).

[102] G. Mairle, M. Seeger, H. Reinhardt, T. Kihm, K. T. Knöpfle, and Chen Lin Wen, Nucl. Phys. **A565**, 543 (1993).

[103] P. Doll, G. Mairle, H. Breuer, K. T. Knöpfle, T. Tohei, and G. J. Wagner, J. Phys. G **5**, 1421 (1979).

[104] E. K. Warburton and J. A. Becker, Phys. Rev. C **40**, 2823 (1989).

[105] P. Doll, Nucl. Phys. **A292**, 165 (1977).

[106] L.W. Whitlow, Ph.D. Thesis, Stanford University, 1990, SLAC-REPORT-357 (1990).

[107] A. Meucci, C. Giusti, and F. D. Pacati, Phys. Rev. C **64**, 014604. (2001).

[108] E. D. Cooper, S. Hama, B. C. Clark, Phys. Rev. C **80**, 034605 (2009).

[109] E. D. Cooper, S. Hama, B. C. Clark, R. L. Mercer, Phys. Rev. C **47**, 297 (1993).

[110] G. S. Blanpied, B. G. Ritchie, M. L. Barlett, R. W. Fergerson, J. A. McGill, and B. H. Wildenthal, Phys. Rev. C **37**, 1304 (1988).

[111] O. Benhar and S. Fantoni, *Nuclear Matter Theory* (Taylor & Francis, Oxford, 2020).

[112] O. Benhar *et al.*, arXiv:1406.4080.